

Nonlinear Laser Matter Interaction in Gas-filled Antiresonant Hollow-Core Fibers

DISSERTATION

zur Erlangung des akademischen Grades

Doctor rerum naturalium (Dr. rer. nat.)



**FRIEDRICH-SCHILLER-
UNIVERSITÄT
JENA**

vorgelegt dem Rat der

Physikalisch-Astronomischen Fakultät
der Friedrich-Schiller-Universität Jena

von M.Tech. M.Sc. Rudrakant Sollapur

geboren am 15.02.1988 in Hukkeri

Gutachter

1. *Prof. Dr. Christian Spielmann*
Institut für Optik und Quantenelektronik
Friedrich-Schiller-Universität Jena
2. *Prof. Dr. Stefan Nolte*
Institut für Angewandte Physik
Friedrich-Schiller-Universität Jena
3. *Prof. Dr. Nicolas Joly*
Institut für Optik, Information und Photonik
Max-Planck-Institut für die Physik des Lichts

Tag der Disputation: 26. March 2019

*The beauty of creation is that everything is tenderly
balanced. So tenderly, you cannot disturb it - not easily.
The whole creation is like this. That manifests the mastery
of the Creator.*

-SADHGURU

TO MY PARENTS PROF. DR. M R SHOLLAPUR AND
PROF. DR. SHRIDEVI PATTED

Zusammenfassung

Die Entwicklung von Lichtleitfasern und der sich daraus ergebenden Technologien hat in den letzten Jahrzehnten erhebliche Veränderungen in den menschlichen Gesellschaften weltweit bewirkt. Optische Fasern haben aufgrund ihrer Kompaktheit, geringen Verluste und nicht zuletzt den günstigen Preis viele in der Vergangenheit etablierte Technologien nach und nach ersetzt. Beispielsweise ließ am Ende des 20. Jahrhundert die Telekommunikationsrevolution durch den weiter verbreiteten Einsatz von Glasfaserkabeln die Welt näher zusammenrücken. Am Anfang des 21. Jahrhunderts haben Glasfaserlaser nicht nur eine weit verbreitete Anwendung in der Industrie für das Schneiden und Schweißen gefunden, sondern auch zahlreiche wissenschaftliche Anwendungen erst ermöglicht. Alle diese neuen Anwendungen waren das Ergebnis einer kontinuierlichen Forschung der Mechanismen der Lichtführung in optischen Fasern. Um mit den Erfordernissen Schritt zu halten, hat sich Glasfasertechnologie von der Lichtführung in konventionellen Glasfasern hin zu jener in Hohlkernfasern wie Kagome-Fasern weiterentwickelt.

In den letzten Jahren finden antiresonante Hohlkernfasern (ARHCF) aufgrund ihrer neuartigen optischen Eigenschaften zunehmende Anwendungen in verschiedenen Bereichen der Wissenschaft und Technologie. ARHCF haben eine große Übertragungsbandbreite, die von ultravioletten bis infraroten Wellenlängen reicht. Aufgrund ihres Lichtleitmechanismus ergeben sich aber sogenannte *strand resonances*, das sind spektral schmale Banden mit hoher Dämpfung. Die Entwicklung eines tieferen Verständnisses der neuartigen Eigenschaften und faszinierenden Anwendungsmöglichkeiten von ARHCF bilden den Kern dieser Arbeit. Im ersten Teil werden Untersuchungen der einzigartigen Fasereigenschaften von ARHCF präsentiert. Dazu gehört die abrupte Änderung der Gruppengeschwindigkeitsdispersion (GVD) in der Nähe von Wellenlänge der *strand resonances*, sowie die Entwicklung des Polarisationszustandes bei Propagation in verschiedenen polygonal strukturierten Faserkernen. Der zweite Teil dieser Arbeit befasst sich mit der spektralen Verbreiterung eines ultrakurzen Pulses in einer gasgefüllten ARHCF unter den Bedingungen einer stark variierenden GVD in der Nähe der verlustbehafteten *strand resonances*. Dabei wurde erstmals festgestellt, dass die nichtlinearen Effekte zur Generation neuer Frequenzen, die mit einem solchen Dispersionsprofil verbunden sind, die erheblichen linearen Verluste im Resonanzbereich

überwinden können und so zu einem spektral kontinuierlichen Ausgangssignal führen. Im letzten Teil der Arbeit wird dann noch gezeigt, dass in gasgefüllten knotenlosen ARHCF Laserpulse durch Selbstpulskompression auf eine Dauer von wenigen Zyklen verkürzt werden können.

Das Dispersionsprofil in der Nähe der *strand resonances* der ARHCF wird unter Verwendung eines Mach-Zehnder-Interferometers, in dem sich die Faser in einem Arm befindet, charakterisiert. Wenn eine Weißlichtquelle verwendet wird, kann aus dem spektral aufgelösten Interferenzsignal die Dispersion der Faser ermittelt werden. Das aufgezeichnete Interferenzmuster zeigt in der Nähe der Resonanz eine hochfrequente Modulation, die entfernt von der Resonanz dann wieder niederfrequent wird. Diese Streifenmuster werden durch Fourier-Analyse numerisch verarbeitet, um so das Dispersionsprofil zu erhalten. Die extrahierten Dispersionskurven zeigen eine Variation der GVD um mehrere Größenordnungen. Es konnte auch gezeigt werden, dass die genaue Position der Resonanzwellenlänge sehr kritisch vom genauen Aufbau der Faser abhängt. Diese Messungen bilden die Grundlage für ein besseres Verständnis der Leitungsmechanismen, aber auch wichtige Hinweise für Optimierungen des Faserdesigns sowie des Faserziehvorgangs. Nicht zuletzt sind diese Messungen die Grundlagen für die Experimente und Simulationen zur Erzeugung von Superkontinuum und ultrakurzer Pulse in gasgefüllten ARHCF.

Das Verständnis der Entwicklung des Polarisationszustandes der sich ausbreitenden Grundmode in einer ARHCF ist für den Einsatz in vielen photonischen Anwendungen unabdingbar. Die geometrieinduzierte Polarisationsabhängigkeit in verschiedenen polygonkernförmigen ARHCF wird hier erstmals experimentell untersucht. Dabei wird die Veränderung der Polarisation des Ausgangslichts als Funktion der Orientierung der Eingangspolarisation in Bezug auf den Faserquerschnitt betrachtet. Dabei zeigt sich, dass strukturelle Abweichungen von der regulären Polygonform Doppelbrechung und einen von der Polarisation abhängigen Verlust induzieren. In der Mitte des Übertragungsbandes einer bestimmten ARHCF tritt nicht nur der geringste Verlust auf, sondern das Ausgangslicht zeigt eine minimale Elliptizität für einen linear polarisierten Eingang. Die Ergebnisse zeigen eine erhebliche Zunahme der Doppelbrechung in Richtung der Resonanzwellenlängen. Es konnte außerdem gezeigt werden, dass sowohl die Betriebswellenlänge als auch die sorgfältige Wahl der relativen Orientierung der Eingangspolarisation in Bezug auf den Faserquerschnitt entscheidend sind, um Ausgangslicht mit minimaler Elliptizität zu erreichen, das für viele Anwendungen eine Grundvoraussetzung ist. Das beobachtete einzigartige Dispersionsprofil der ARHCF spielte eine wesentliche Rolle bei der nichtlinearen spektralen Verbreiterung ultrakurzer Pulse in einer gasgefüllten ARHCF. Das beschriebene Experiment untersucht die Aus-

wirkung einer abrupten Änderung der GVD nahe der Resonanz auf die Dynamik der nichtlinearen Impulse durch Anregung nahe der Resonanzwellenlänge in einer mit Edelgas gefülltem AHRCF. Damit ist es nun möglich mit einer Krypton gefüllten ARHCF ein Superkontinuum mit Ausgangsenergie von $\sim 23 \mu\text{J}$ zu erzeugen, das sich über drei optische Oktaven erstreckt, also von tiefen UV-Wellenlängen (200 nm) bis zum nahen Infrarot ($1.7 \mu\text{m}$) reicht. Die Dispersion aufgrund der *strand resonances* übertrifft den Dispersionsbeitrag des Gases und leitet einen beschleunigten Aufspaltungsprozess in einem nicht-adiabatischen Dispersionsregime ein. Die Simulationen bestätigen die Emission phasenangepasster Cherenkov-Strahlung auf beiden Seiten der Resonanz. Derartige Dispersionsprofile sind unabhängig von der Kerngröße und ermöglichen die Skalierung höherer Eingangsenergien durch eine Konstruktion mit einer größeren Kerngröße.

Hohlkernfaser mit negativer Krümmung des Faserkerns, sogenannte negative curvature (NC) ARHCF, haben in den letzten Jahren ebenfalls große Verbreitung gefunden. Denn sie haben den Vorteil, dass im nahen und mittleren Infrarotbereich nahezu verlustfrei übertragen werden kann, welches einem Wellenlängenbereich weit jenseits der Absorption von Quarzglas bei $1,9 \mu\text{m}$ entspricht. Im letzten Teil wurde nun die Erzeugung von Pulsen mit weniger Zyklen in einer Argon gefüllten, knotenlosen Quarzglas-NCARHCF untersucht. Komplexe nichtlineare Prozesse, wie die Solitonspaltung, werden durch Pumpen fernab der Resonanzwellenlänge vermieden und eine Selbstpulskompression erreicht, die bei einer Wellenlänge von $1,75 \mu\text{m}$ Pulse von nur mehr 2,5 Zyklen mit einer Ausgangsenergie von $\sim 18 \mu\text{J}$ ergibt.

Zusammenfassend wurden in dieser Arbeit die Vorteile von ARHCF wie Dispersionsabstimmung, Resonanzposition, Skalierbarkeit und Transmission von ultravioletten bis mittleren Infrarotwellenlängen für die Licht-Materie-Wechselwirkungen demonstriert. Damit konnte gezeigt werden, dass ARHCF ideale Kandidaten für die weitere Erforschung nichtlinearer Optik in gasgefüllten Fasern sind und den Weg ebnen für die Entwicklung kohärenter Ultrabreitband- und Hochenergiequellen. Diese Quellen können viele interessante Anwendungen in verschiedenen Wissenschafts- und Technologiefeldern wie Attosekunden-Messtechnik, Biophotonik, Spektroskopie usw. erleichtern.

Abstract

Invention of optical fibers and technologies driven by it have brought significant transformation in the human societies across the globe over last few decades due to their small footprint, excellent power budget and economically affordable. Since their advent, optical fibers have gradually replaced many technologies of the previous centuries; e.g. in 20th century, optical fiber enabled telecommunication revolution made the whole world smaller, few micrometre thin optical fibers are able to monitor structural health of large structures, since the early 21st century fiber lasers have transformed industrial cutting and welding along with high impact scientific applications, etc. Such applications have been possible as a result of continuous research in studying light guidance in optical fibers. The evolution of optical fiber technology has come a long way from solid core-clad fibers to hollow core-clad guidance like Kagome fibers.

In the recent years, the antiresonant hollow core fibers (ARHCF) are finding increasing applications in different fields of science and technology due to their novel optical properties. The in-depth understanding of these novel properties and intriguing possibilities for applications is at the core of this thesis. This work investigates the unique fiber properties like abrupt variation of group velocity dispersion (GVD) of the ARHCF near resonance wavelengths due to fiber strands that form the fiber core structure and polarization evolution in different polygonal structured cores. Strand resonances induce narrow band high attenuation regions in the broad transmission bandwidth of the ARHCF extending from ultraviolet to infrared wavelengths. This work delves into spectral broadening of an ultrashort pulse in gas-filled ARHCF under the new scenario of highly varying GVD profile. The nonlinear effects associated in such a dispersion profile are found to overcome lossy resonance region and generate a spectrally continuous output. Further, the work explores few cycle pulse generation in gas-filled nodeless ARHCF by self-pulse compression. The dispersion profile near the fundamental resonance of the ARHCF is characterized using an interferometric technique in a balanced Mach-Zhender interferometer. The interference fringes produced by the superposition of light from the two arms contain the information about the dispersion of the fiber. The recorded interference pattern contains both high and low frequency fringe patterns away from the resonance and in the vicinity of resonance,

respectively. These fringe patterns are numerically processed through Fourier analysis to obtain dispersion profile. Extracted dispersion curves show significant GVD variation by few orders in magnitude (of fs^2/cm) in close proximity of the resonance wavelength along with additional zero dispersion wavelengths. Position of resonance wavelength depends on the thickness of the glass strands forming the fiber core and it can be controlled in the fiber design opening up new ways to engineer precise GVD profile with possible interesting applications involving ultrashort pulses.

Understanding polarization behaviour of the propagating fundamental mode is important to develop relevant photonic devices. Geometry-induced polarization dependence in different polygon core shaped ARHCFs is studied from the experimental perspective. Variation in the polarization of the output light as function of orientation of input polarization with respect to fiber cross section is investigated. The results show that structural deviations from regular polygonal shape induce birefringence and polarization dependent loss in polygon core antiresonant fibers. The center of the transmission band in a given ARHCF has lowest loss and is found to deliver the output light with minimal ellipticity for a linearly polarized input. The results show substantial increase in birefringence towards the resonance wavelengths. Both operating wavelength at lowest loss and careful choice of the relative orientation of input polarization with respect to fiber cross section is critical to achieve output light with minimal ellipticity.

The observed unique dispersion profile of the ARHCF can play a significant role in nonlinear spectral broadening of ultrashort pulses in gas-filled ARHCF. The experiment studies the effect of abrupt variation in GVD near resonance on the nonlinear pulse dynamics by pumping close to resonance wavelength in inert gas filled ARHCF. The results show the supercontinuum generation spreading over three octave of broadband light ranging from deep ultraviolet (UV) wavelengths to near infrared (IR). The dispersion due to strand resonance outperforms the dispersion contribution from gas and initiates accelerated fission process in a non-adiabatic dispersion regime. The simulations confirm the emission of multiple phase matched Cherenkov radiations on both sides of the resonance. Broadened output spectrum extends from 200 nm to $1.7 \mu\text{m}$ at output energy of $\sim 23 \mu\text{J}$ in krypton-filled fiber. Such dispersion profiles are independent of the core size and enable scaling higher input energies by design of larger core ARHCFs. Another advantage of negative curvature (NC) ARHCFs is that they can transmit light from near infrared to mid infrared wavelengths, well beyond traditional silica cut-off wavelength at $1.9 \mu\text{m}$. This thesis explores generation of few cycle pulses in argon-gas filled silica based nodeless NC-ARHCFs. Complex nonlinear processes like soliton fission is avoided by pumping away from the resonance wavelength and achieves self-pulse compression yielding 2.5 cycle pulses at wavelength of $1.75 \mu\text{m}$ with output energy of

$\sim 18 \mu\text{J}$.

In summary, this work shows first successful measurement of such large GVD variation of few orders in magnitude arising due to geometry induced dispersion. This provides a new platform to study laser matter interactions where one can combine ARHCF design advantages like dispersion tuning, position of resonance, scaling capabilities, transmission from ultraviolet to mid infrared wavelengths. The work demonstrates not only achieving of over three octave broadband supercontinuum, but also generation of 2.5 cycle pulses at $1.8 \mu\text{m}$ by the optimisation of different fiber parameters and choice of nonlinear medium. These ARHCFs are ideal candidates to further explore nonlinear optics in gas-filled fibers and pave way towards development of coherent ultra-broadband and high-energy sources. These sources can facilitate many intriguing applications different fields of science and technology like attosecond metrology, biophotonics, spectroscopy etc.

Contents

Zusammenfassung	I
Abstract	IV
Table of contents	1
1 Introduction	3
2 Nonlinear Pulse Propagation in Fibers	7
2.1 Maxwell's equations	7
2.2 Pulse propagation equations	10
2.2.1 Unidirectional pulse propagation equation	10
2.2.2 Generalized nonlinear Schrödinger equation	11
2.3 Nonlinear effects	12
2.3.1 Group velocity dispersion (GVD)	12
2.3.2 Second order susceptibility $\chi^{(2)}$	14
2.3.3 Self phase modulation (SPM)	15
2.3.4 Soliton	16
2.3.5 Self-steepening	17
2.3.6 Modulation instability (MI)	18
2.3.7 Dispersive wave generation (Cherenkov radiation emission)	18
2.3.8 Four wave mixing (FWM)	19
2.3.9 Supercontinuum generation	19
2.3.10 Stimulated inelastic scattering	20
3 Antiresonant Hollow-Core Fiber	21
3.1 Types of Hollow Core Fibers (HCF)	22
3.2 Types of ARHCFs	24
3.3 Guiding mechanism	26
3.4 Characteristics of an ARHCF	27
3.4.1 Spectral distribution of the losses in the ARHCF core	28
3.4.2 Effective refractive index at resonance	29
3.5 Antiresonant fibers used in this work	30
3.6 Summary	31
4 Dispersion Measurement of Antiresonant Hollow Core Fiber	34
4.1 Experimental setup to measure GVD	35
4.2 Measurement and Analysis	37

4.2.1 Phase retrieval	38
4.3 Results and Discussion	40
4.4 Summary	42
5 Polarization Evolution in ARHCF	44
5.1 Importance of polarization evolution in fibers	44
5.2 Theory	45
5.3 Properties of polygon shaped core ARHCFs	46
5.4 Experimental set up	47
5.5 Impact of core geometry on output ellipticity	48
5.6 Impact of input wavelength on output ellipticity	50
5.7 Discussion	51
5.8 Summary	55
6 Supercontinuum Generation in ARHCF	57
6.1 Comparison of dispersion between ARHCF and Capillary	58
6.2 Experimental set-up	59
6.3 Supercontinuum generation	61
6.4 Numerical Simulation and Analysis	66
6.5 Discussion	68
6.6 Supercontinuum generation in Raman-active gas	78
6.7 Summary	80
7 Few Cycle Pulse Generation in Negative Curvature ARHCF	82
7.1 Introduction	82
7.2 NC-ARHCF Properties	83
7.3 Experimental set up	84
7.4 Results and Discussion	85
7.5 Summary	88
8 Summary and Outlook	89
References	92
List of Abbreviations and Symbols	103
List of Figures	105
List of Tables	107
Publications	108
Ehrenwörtliche Erklärung	114
Acknowledgments	116

1 Introduction

Light is the fastest known entity in the universe. There is nothing physical in the existence that travels faster the velocity of light in vacuum. There has always been an effort to guide the light from one point to another. Since the first description on light guiding by total internal reflection in 1842 [1], there has been a continuous effort in developing new strategies for guided light. In the early nineteenth century, quartz glasses was used to transport the light in a microscope with an ability to bend the light at the corners [2]. The development of flexible fiberscopes by total internal reflection in 1954 paved the way for fiber optics revolution [3]. About three decades later, seeds of Anti-Resonant Reflecting Optical Waveguiding (ARROW) were sown giving rise to a new class of light propagation in hollow-core fibers [4, 5]. Such fibers are also known as Antiresonant Hollow-Core Fibers (ARHCF). This work focuses on nonlinear laser matter interactions in gas-filled ARHCF.

Nonlinear optics has been one of the most important areas of science and technology with numerous applications in spectroscopy, optical coherence tomography, optical communication, biomedical imaging, metrology and many others. Nonlinear interactions are possible when an intense light interacts with matter. Nonlinear interactions in solid core optical fibers have found numerous applications in different fields started with the self-phase modulation (SPM) and this lead to the observation of solitons in optical fibers [6, 7]. Over the last few decades, the applications have extended to supercontinuum generation [8], four-wave mixing (FWM) in microstructured fibers [9], optical switches based on cross phase modulation [10], and few-cycle pulse generation [11]. However, the solid core fibers operate at low pulse energies of few nanojoules limited by damage threshold of silica. Gas-filled hollow core capillary waveguides provide energy scaling by few orders in magnitude and support ultrashort pulse propagation [12–15]. Nonlinear effects can be increased by tighter light confinement in the hollow core i.e. by reducing

the bore diameter. However, the loss length of these fibers is proportional to the cube of the bore radius a and is given by [16, 17]

$$L_{\frac{1}{e}} \approx \left(\frac{2\pi}{z_{01}}\right)^2 \frac{a^3 \sqrt{n^2 - 1}}{\lambda^2 n^2 + 1} \quad (1.1)$$

where the first root of the zero-order Bessel function J_0 is z_{01} , refractive index of the glass is n and vacuum wavelength of light is given by λ . The $1/e$ intensity decay length in fused silica capillary for a 10 μm uncoated bore is ~ 3.55 mm. Such short decay lengths are not practical in hollow-core fiber (HCF) experiments. Advent of hollow-core photonic crystal fiber (HC-PCF) revolutionized the field of nonlinear optics in gas filled fiber where they provide two order higher effective nonlinearities for ten times narrower bore diameter along with low propagation losses [13, 15]. Ref. [15] provides a detailed review on ultrafast pulse dynamics and different nonlinearities that take place in gas-filled HC-PCFs.

Over the last decade, interest in antiresonant hollow-core fibers has increased substantially due to its unique properties like transmission in broad spectral bandwidth spreading over multioctave frequencies, fundamental propagation mode across the transmission bandwidth [18], low propagation losses [19], low dispersion (except in the vicinity of the strand resonance wavelength) [20], extending transmission towards mid infrared spectral region, beyond cut-off wavelength of in silica fibers [21].

The hollow-core nature of the antiresonant hollow core fibers (ARHCF) gives an additional advantage to fill the core with a certain choice of nonlinear gas to study laser matter interactions. Such fibers provide enhanced light-matter interactions in diffraction free propagation over long lengths. Gas-filled ARHCFs have found applications in soliton pulse compression [14], generation of ultraviolet light by dispersive waves [22], supercontinuum generation [15, 23] and so on.

This thesis is divided into three different parts each containing two chapters. First part is on fundamentals. Chapter 2 provides an overview of Maxwell's equations that describe the electromagnetic wave propagation. Two different pulse propagation models known as unidirectional pulse propagation equation (UPPE) and Generalized nonlinear Schrödinger equation (GNLSE) are introduced. The last section of the chapter describes different nonlinear effects that are normally observed in the optical fibers.

Chapter 3 introduces different hollow-core fibers with a focus on ARHCF. It explains

the light guiding mechanism, characteristic features of an ARHCF and details different ARHCFs used in this work.

Second part of thesis deals with characterization of unique properties of ARHCF. Chapter 4 details measurement of group velocity dispersion (GVD) of the ARHCF in the vicinity of the spectral resonance region by interferometric method.

Chapter 5 explores the polarization evolution in ARHCF. The study involves polarization evolution as a function of variation in azimuthal periodicity of the single ring ARHCF. Further, impact of resonance on the polarization property of the propagating light is discussed.

The final part of the thesis concentrates on nonlinear interactions in gas-filled ARHCF: Chapter 6 studies light matter interaction in gas filled ARHCF leading to supercontinuum generation. The studies are carried out with inert gas krypton and Raman-active gas nitrogen filled ARHCF. Numerical simulation analyse different nonlinear effects that are responsible for supercontinuum generation focusing on the effect of dispersion profile of the ARHCF near resonance wavelength.

Chapter 7 focuses on few cycle pulse generation in argon gas filled in a nodeless ARHCF and temporal characterization of the output pulses.

Final chapter summarizes the main results and provides an outlook for the future experiments.

Part I: Fundamentals

2 Nonlinear Pulse Propagation in Fibers

This chapter discusses the fundamental principles of nonlinear pulse propagation in optical fibers. The pulse propagation equations are derived from Maxwell's equations. The discussion focuses on two different numerical methods that are implemented in this work.

- unidirectional pulse propagation equation (UPPE) [24–26]
- nonlinear Schrödinger equation (NLSE) [27]

Different nonlinear effects that are experienced by propagating light in the fiber are explained with the help of UPPE and NLSE simulations. Section 2.1 introduces Maxwell's equations and its applications in nonlinear optics. The two numerical methods (UPPE, NLSE) for pulse propagation in optics fibers are detailed in section 2.2. A brief introduction to different third order nonlinear effects are discussed in section 2.3.

2.1 Maxwell's equations

Maxwell's equations govern the propagation of electromagnetic waves in any given medium. They govern both linear and nonlinear effects induced by the polarization of the propagating light. Maxwell's equations are defined in SI units as:

$$\nabla \cdot \mathbf{D} = \rho \quad (2.1)$$

$$\nabla \cdot \mathbf{B} = 0 \quad (2.2)$$

$$\nabla \times \mathbf{E} = -\frac{\partial \mathbf{B}}{\partial t} \quad (2.3)$$

$$\nabla \times \mathbf{H} = \mathbf{J} + \frac{\partial \mathbf{D}}{\partial t} \quad (2.4)$$

$$\mathbf{D} = \epsilon_0 \mathbf{E} + \mathbf{P} \quad (2.5)$$

$$\mathbf{B} = \mu_0 \mathbf{H} + \mathbf{M} \quad (2.6)$$

where, \mathbf{E} and \mathbf{H} are the electric field and magnetic field of the propagating electromagnetic wave, \mathbf{D} and \mathbf{B} are the corresponding electric and magnetic flux densities, respectively. \mathbf{J} , ρ , ϵ_0 and μ_0 are the current density, charge density, vacuum permittivity and vacuum permeability, respectively. \mathbf{P} and \mathbf{M} correspond to induced electric and magnetic polarizations. Vector quantities are written in bold and nabla - ∇ is the Laplacian operator to denote divergence ($\nabla \cdot$) and curl ($\nabla \times$) operators.

In a nonmagnetic medium like optical fiber, \mathbf{M} is equal to zero. Optical fibers do not carry any electric charge ($\rho=0$) and current ($\mathbf{J}=0$) reducing Maxwell's equations to

$$\nabla \cdot \mathbf{E} = 0 \quad (2.7)$$

$$\nabla \cdot \mathbf{B} = 0 \quad (2.8)$$

$$\nabla \times \mathbf{E} = -\frac{\partial \mathbf{B}}{\partial t} \quad (2.9)$$

$$\nabla \times \mathbf{H} = \frac{\partial \mathbf{D}}{\partial t} \quad (2.10)$$

$$\nabla \times \mathbf{H} = \frac{\partial(\epsilon_0 \mathbf{E} + \mathbf{P})}{\partial t} \quad (2.11)$$

Maxwell's wave equation can be obtained by taking curl of Eq. 2.9 and substituting with Eqs. 2.7, 2.8, 2.11 to eliminate \mathbf{B} and \mathbf{D} and obtain the following equation with further simplification in terms of \mathbf{E} and \mathbf{P}

$$-\nabla^2 \mathbf{E} + \frac{1}{c^2} \frac{\partial^2 \mathbf{E}}{\partial t^2} = -\mu_0 \frac{\partial^2 \mathbf{P}}{\partial t^2} \quad (2.12)$$

where c is the speed of light in vacuum and is given by $\frac{1}{\sqrt{\epsilon_0\mu_0}}$.

Induced polarization \mathbf{P} can be split into linear part and \mathbf{P}_L and nonlinear part \mathbf{P}_{NL} such that

$$\mathbf{P} = \mathbf{P}_L + \mathbf{P}_{NL} \quad (2.13)$$

where \mathbf{P}_L has linear dependence on \mathbf{E} and \mathbf{P}_{NL} is of great interest in this work where higher orders of \mathbf{E} play a significant role in the pulse propagation dynamics. Limiting to third order nonlinear effects governed by $\chi^{(3)}$, \mathbf{P}_L and \mathbf{P}_{NL} are written as

$$\mathbf{P}_L = \epsilon_0 \int_{-\infty}^t \chi^{(1)}(t-t') \cdot \mathbf{E}(\mathbf{r}, t') dt \quad (2.14)$$

$$\begin{aligned} \mathbf{P}_{NL} = \epsilon_0 \int_{-\infty}^t dt_1 \int_{-\infty}^{t_1} dt_2 \int_{-\infty}^{t_2} dt_3 \\ \times \chi^{(3)}(t-t_1, t-t_2, t-t_3) : \mathbf{E}(\mathbf{r}, t_1) \mathbf{E}(\mathbf{r}, t_2) \mathbf{E}(\mathbf{r}, t_3) \end{aligned} \quad (2.15)$$

where $\chi^{(1)}$ is the linear susceptibility and \mathbf{P}_L is the linear polarization due to electric field \mathbf{E} . Linear index of refraction (n) is related to linear susceptibility and is given by $n = \sqrt{1 + \chi^{(1)}}$. At higher incident \mathbf{E} , the third order susceptibility $\chi^{(3)}$ introduces the Kerr effect leading to intensity dependent modification in refractive index. Kerr effect leads to different nonlinear phenomena like self-phase modulation (SPM), four-wave mixing (FWM) and cross-phase modulation (XPM). Change in the refractive index due to high intensity of the pulse is mathematically given by

$$\Delta n = \bar{n}_2 |\mathbf{E}|^2 \quad (2.16)$$

where $|\mathbf{E}|^2$ is the intensity of the pulse. \bar{n}_2 is the nonlinear refractive index and is defined as

$$\bar{n}_2 = \frac{3\text{Re}(\chi^{(3)})}{8n_0} \quad (2.17)$$

where Re stands for the real part, the optical field \mathbf{E} is assumed to be linearly polarized and n_0 is the refractive index of the material.

2.2 Pulse propagation equations

There are two approaches to model nonlinear pulse propagation in optical fibers. Unidirectional pulse propagation equation is based on real electric field [24] and generalized nonlinear Schrödinger equation is based on envelope approach. The following sections discuss the two methods in detail.

2.2.1 Unidirectional pulse propagation equation

The UPPE assumes pulse propagation in the positive z-direction. Considering the electric and polarization fields in the same direction, the scalar form of the wave equation can be written as [24]

$$\left(\partial_z^2 - \frac{n^2(\omega)}{c^2}\partial_t^2\right)E(z,t) = \mu_0\partial_t^2\mathbf{P}_{\text{NL}}(z,t) \quad (2.18)$$

where the electric field propagating in z-direction is written as

$$E(z,t) = \frac{1}{2\pi}\int_{-\infty}^{\infty}A(z,\omega)e^{i(\beta(\omega)z-\omega t)}d\omega \quad (2.19)$$

where the electric field amplitude is A , propagation constant is $\beta(\omega)$. The scalar equation 2.18 has real electric field.

Therefore,

$$E(z,t) = E^*(z,t) \quad (2.20)$$

and

$$A(z,-\omega)e^{i\beta(-\omega)z} = A^*(z,\omega)e^{-i\beta(\omega)z} \quad (2.21)$$

The UPPE equation is defined as [26]:

$$\begin{aligned} \frac{\partial E(z,\omega)}{\partial z} = & i\left(\beta(z,\omega) - \frac{\omega}{\nu}\right)E(z,\omega) - \alpha(\omega)E(z,\omega) \\ & + i\frac{\omega^2}{2c^2k(\omega,z)}\chi^{(3)}(z)\mathcal{F}[E(z,t)^3] \end{aligned} \quad (2.22)$$

where $\alpha(\omega)$ includes frequency dependent losses, $k(\omega,z) = \sqrt{k^2(\omega) - k_x^2 - k_y^2} = \beta(z,\omega)$ and the last term $i\frac{\omega^2}{2c^2k(\omega,z)}\chi^{(3)}(z)\mathcal{F}[E(z,t)^2]$ includes Kerr nonlinear effects and

$\mathcal{F}[E(z, t)]$ gives Fourier transform of real electric field $E(z, t)$. Section 6.4 details application of UPPE for given experimental conditions.

2.2.2 Generalized nonlinear Schrödinger equation

Generalized nonlinear Schrödinger equation (GNLSE) is based on complex envelope and is extensively used in literature to model pulse propagation in optical fiber. The equation is defined as:

$$\begin{aligned} \frac{\partial A}{\partial z} - i \sum_{m \geq 2} \frac{i^m \beta_m}{m!} \frac{\partial^m A}{\partial \tau^m} + \frac{\alpha}{2} A = i\gamma \left(1 + i\tau_{\text{shock}} \frac{\partial}{\partial \tau} \right) \\ \times \left(A(z, t) \int_{-\infty}^{\infty} R(\tau') |A(z, \tau - \tau')|^2 d\tau' \right) \end{aligned} \quad (2.23)$$

where the left hand side terms denote linear effects and right hand terms denote nonlinear effects. The retarded time frame τ is equal to $\left(t - \frac{z}{v_g} \right)$ and group velocity is v_g , attenuation is given by α and the dispersion coefficients are defined as $\beta_m = \left(\frac{d^m \beta}{d\omega^m} \right)_{\omega=\omega_0}$ (for $m=1,2,3,\dots$). The nonlinear coefficient γ is defined as

$$\gamma = \frac{\omega_0 n_2(\omega_0)}{c A_{\text{eff}}(\omega_0)} \quad (2.24)$$

with A_{eff} as the effective mode area at the carrier frequency ω_0 and $n_2 = \frac{2\bar{n}_2}{\epsilon_0 n c}$. $\tau_{\text{shock}} = \frac{1}{\omega_0}$ leads to effects like self-steepening. The nonlinear Raman response $R(T)$ is defined as

$$R(T) = (1 - f_R) \delta(t) + f_R h_R(t) \quad (2.25)$$

where $\delta(t)$ is the Dirac delta function, f_R is the delayed fractional contribution of the Raman response to \mathbf{P}_{NL} and h_R is the Raman response function. GNLSE is explained further in section 6.5 for experimental conditions.

A simple version of GNLSE contains only GVD and instantaneous Kerr nonlinearity. This version is known as nonlinear Schrödinger equation (NLSE) and expressed as

$$\frac{\partial A}{\partial z} = -i \frac{\beta_2}{2} \frac{\partial^2 A}{\partial \tau^2} + i\gamma A |A|^2 \quad (2.26)$$

2.3 Nonlinear effects

This section discusses different nonlinear effects that an intense pulse can undergo in a given medium. The physics of some important nonlinear processes discussed here include group velocity dispersion, second order nonlinearity, self phase modulation, nonlinear length, self-steepening, modulation instability, dispersion wave generation, four-wave mixing, supercontinuum generation, and stimulated inelastic scattering.

2.3.1 Group velocity dispersion (GVD)

Chromatic dispersion is inherent property of any material. It manifests by having frequency dependent refractive index towards the propagating electromagnetic waves. Dispersion profile of a fiber plays an important in the propagation of ultrashort pulses having significant spectral bandwidth. Though, the individual spectral components in an optical pulse travel at different velocities, the envelope of the pulse travels at a well defined group velocity (v_g) that depends on the fiber design parameters. Mathematically, it is possible to account for the fiber dispersion experienced by the propagating pulse using Taylor series expansion of the mode-propagation constant β about central frequency ω_0 .

$$\beta(\omega) = n(\omega)\frac{\omega}{c} = \beta_0 + \beta_1(\omega - \omega_0) + \frac{1}{2}\beta_2(\omega - \omega_0)^2 + \dots \quad (2.27)$$

where

$$\beta_m = \left(\frac{d^m \beta}{d\omega^m} \right)_{\omega=\omega_0} \quad (m = 0, 1, 2, \dots) \quad (2.28)$$

The parameter β_1 relates to group velocity and is given by

$$\beta_1 = \frac{1}{v_g} = \frac{n_g}{c} = \frac{1}{c} \left(n + \omega \frac{dn}{d\omega} \right) \quad (2.29)$$

where n_g is group index. The term β_2 is responsible for pulse broadening and is known as GVD parameter. β_2 is a function of refractive index and is given by

$$\beta_2 = \frac{1}{c} \left(2 \frac{dn}{d\omega} + \omega \frac{d^2 n}{d\omega^2} \right) \quad (2.30)$$

A given wavelength is in normal dispersion regime if $\beta_2 > 0$ and in anomalous dispersion regime if $\beta_2 < 0$. When $\beta_2 = 0$, it is known as zero dispersion wavelength (ZDW). Near ZDWs, higher order dispersions like third order dispersion (β_3) start to play a role in pulse propagation. Chapter 4 details the measurement of highly varying GVD near strand resonance wavelength of the ARHCF where definition of refractive index ($n(\omega)$) is no longer governed by Sellmeier equation.

Temporal properties of a propagating pulse may contribute in the nonlinear effects along with fiber parameters. Two parameters known as dispersion length L_D and nonlinear length L_{NL} assist in classifying different pulse propagation regimes in an optical fiber.

Dispersion length is defined as

$$L_D = \frac{T_0^2}{|\beta_2|} \quad (2.31)$$

where T_0 is the pulse width and modulus sign considers magnitude of the GVD parameter.

As shown in Eq. 2.16, ultrashort pulse experiences intensity dependent refractive index. Mathematically, it can be represented as

$$n(\omega, I) = n_0(\omega) + n_2 I \quad (2.32)$$

where $n_0(\omega)$ is the linear refractive index of the material, n_2 is the nonlinear refractive index equal to $\frac{3}{2n_0^2\epsilon_0 c} \chi^{(3)}$ and I is the intensity of the propagating light in the medium is given by $\frac{1}{2} n_0 \epsilon_0 c |E|^2$. Such varying refractive index with the intensity leads to accumulation of nonlinear phase shift (ϕ_{NL}) in the propagating light. This can be expressed as

$$\phi_{NL} = \frac{2\pi}{\lambda} n_2 I(t) L \quad (2.33)$$

where L is the propagation length. If the propagating light experience π -phase shift, then the corresponding propagation length is known as nonlinear length L_{NL} and is given by

$$L_{NL} = \frac{1}{\gamma P_0} \quad (2.34)$$

where P_0 is the peak power of the pulse. The parameters L_D and L_{NL} provide informa-

tion on which dispersive or nonlinear effects contribute towards pulse evolution. By comparing lengths L_D and L_{NL} with respect to actual fiber length L , pulse propagation can be classified into four categories:

- $L \ll L_D$ and $L \ll L_{NL}$

Pulse does not experience any dispersion effects or nonlinear effects. It maintains its pulse shape and spectrum as fiber plays a passive role. However, fiber attenuation needs to be considered in real world applications.

- $L \sim L_D$ and $L \ll L_{NL}$

Pulse propagates in dispersion dominant region where nonlinearities play a minor role. This regime is applicable when the following condition is satisfied.

$$\frac{L_D}{L_{NL}} = \frac{\gamma P_0 T_0^2}{|\beta_2|} \ll 1 \quad (2.35)$$

- $L \ll L_D$ and $L \sim L_{NL}$

Pulse propagation is mainly governed by nonlinear refractive index n_2 leading towards SPM, described in detail in section 2.3.3. Condition for nonlinear dominant regime is defined as

$$\frac{L_D}{L_{NL}} = \frac{\gamma P_0 T_0^2}{|\beta_2|} \gg 1 \quad (2.36)$$

- $L \geq L_D$ and $L \geq L_{NL}$

Pulse propagation is simultaneously influenced by dispersion and nonlinearity. When $\beta_2 < 0$, anomalous dispersion regime yields to soliton (discussed in next sections). When $\beta_2 > 0$, normal dispersion regime supports GVD and SPM.

2.3.2 Second order susceptibility $\chi^{(2)}$

The second order susceptibility $\chi^{(2)}$ is responsible for effects like second harmonic generation or sum frequency generation. $\chi^{(2)}$ nonlinearity can take place only in non-centrosymmetric materials. However, neither the fiber material silica nor the gaseous nonlinear mediums employed in this work (and also in general) are non-centrosymmetric materials. Hence, $\chi^{(2)}$ processes are not in the scope of this work.

2.3.3 Self phase modulation (SPM)

Intensity dependent refractive index induces self phase modulation and is responsible for spectral broadening of the propagating pulse [28]. The nonlinear phase ϕ_{NL} is a function of time and results in continuous phase modulation with time inducing spectral modulation.

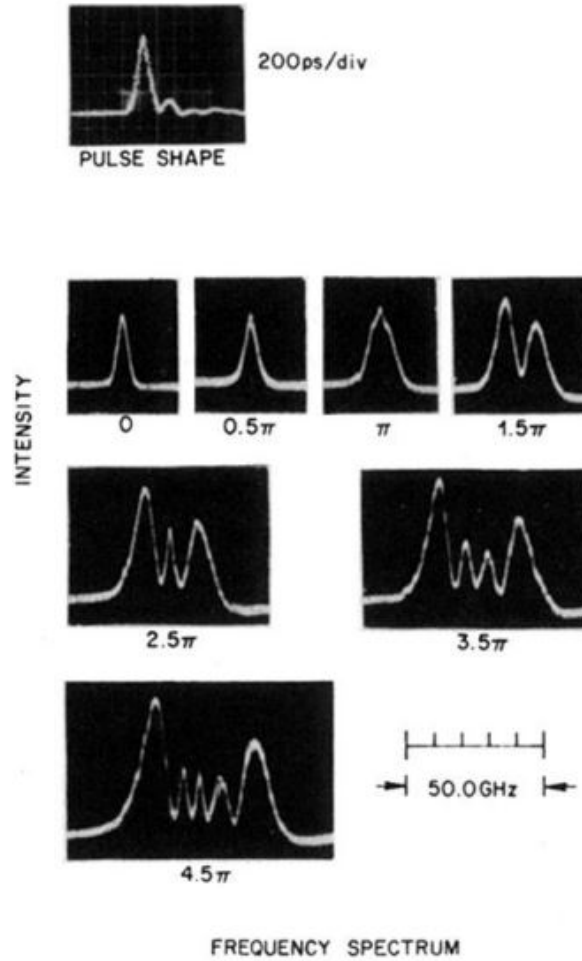


Figure 2.1: Self phase modulation in silica fiber [29].

First experimental observation of SPM in silica fibers is shown in Figure 2.1 [29]. Top figure shows the input pulse. The following figures show output spectrum for different accumulated nonlinear phase at increasing input intensities. The spectra labelled according to maximum phase shift. The spectral broadening due to SPM is symmetric in nature and always results in the depletion of the pump wavelength.

2.3.4 Soliton

Soliton is that pulse which can retain its shape while propagating in dispersive and nonlinear medium. This is achieved by maintaining the balance between GVD and SPM effects. In anomalous dispersion region, the chirp introduced by SPM is compensated by the GVD. Soliton is the solution for the NLSE [27] and has the form

$$A(z, t) = \sqrt{P_0} \operatorname{sech} \left(\frac{t}{T_0} \right) e^{-i|\beta_2|z/2T_0^2} \quad (2.37)$$

where $P_0 = \frac{|\beta_2|}{\gamma T_0^2}$ is the peak power required support fundamental soliton solution. For higher peak power, the soliton is known as higher-order soliton, where N represents the corresponding soliton number. This soliton number N connects the dispersion length L_D and the nonlinear length L_{NL} by the following equation

$$N^2 = \frac{L_D}{L_{NL}} = \frac{\gamma P_0 T_0^2}{|\beta_2|} \quad (2.38)$$

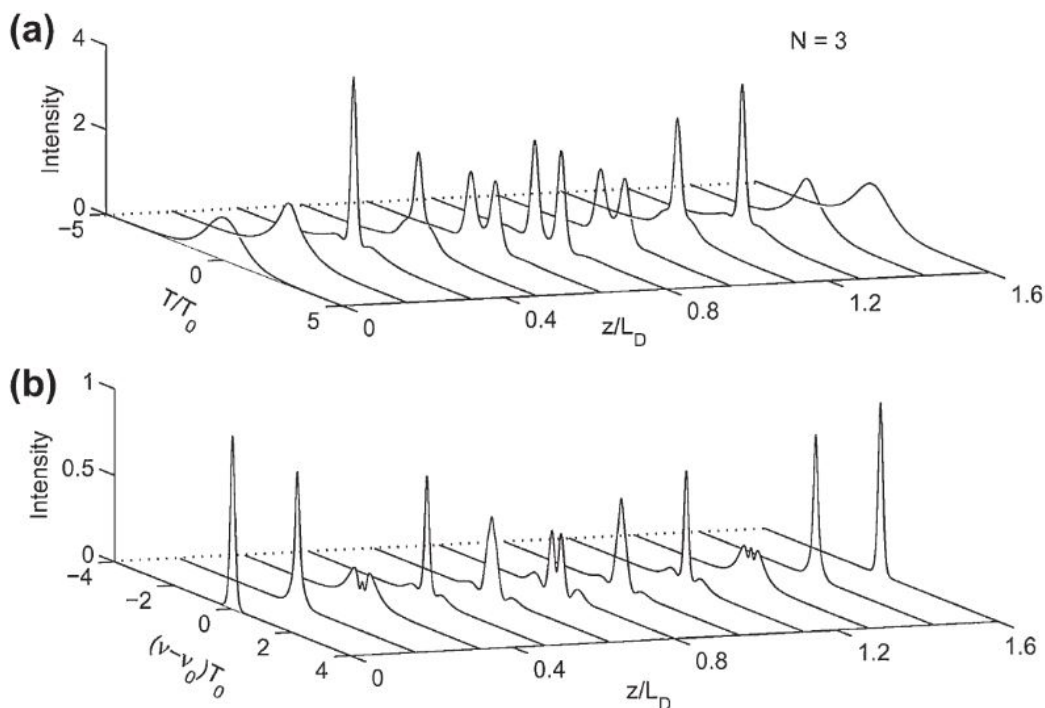


Figure 2.2: Higher order soliton propagating through an optical fiber (a) temporal evolution (b) spectral evolution [27].

$N=1$ is known as fundamental soliton. It propagates with no change in temporal

or spectral shape in a lossless medium. For $N > 1$, soliton continuously evolves along propagation length such that it recovers its initial pulse shape and spectrum after one soliton period as shown in Figure 2.2. It shows propagation of third order soliton over one soliton period in a lossless medium [27]. Initial temporal and spectral profile undergo continuous change along the length of the fiber and recover completely after one soliton period (z_0), which is given by

$$z_0 \approx \frac{T_{\text{FWHM}}^2}{2|\beta_2|} \quad (2.39)$$

where T_{FWHM} is the pulse width at half maximum and is equal to $2\ln(1 + \sqrt{2})T_0$.

2.3.5 Self-steepening

Origin of self-steepening of propagating pulse in a medium is due to intensity dependence of the group velocity [30, 31]. Self-steepening leads to an asymmetric spectral broadening unlike SPM and is mathematically described by the shock term $i\tau_{\text{shock}}\frac{\partial}{\partial\tau}$ in Eq. 2.23 [27]. Figure 2.3 shows self-steepening leading towards optical shock formation [32].

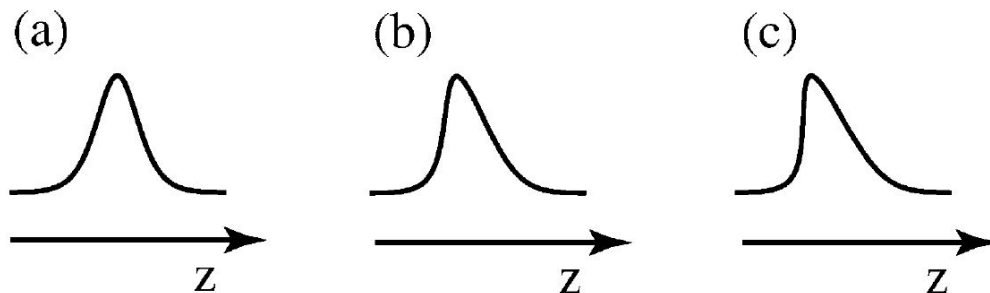


Figure 2.3: Evolution of self steepening:(a) Gaussian input pulse (b) propagation through nonlinear media resulting in trailing edge of the pulse showing self-steepening (c) pulse undergoing significant self-steepening towards onset of an optical shock wave when intensity change instantaneously [32].

Self-steepening distance is given by

$$L_{\text{SS}} = \frac{cT}{n_2^{(g)}I} \quad (2.40)$$

where $n_2^{(g)} \approx n_2$ [32]. The shock is formed on the leading edge if $n_2 < 0$ or on the trailing edge if $n_2 > 0$.

2.3.6 Modulation instability (MI)

Interaction between intense carrier wave at frequency ω and its minor sidebands $\omega \pm \Delta\omega$ (symmetrically located about pump frequency) results in modulation instability [33]. The growth of sidebands originates from the noise resulting in incoherent spectral broadening and breaking the temporal structure of the input pulse. MI is known to occur in anomalous dispersion regimes, but the sidebands can appear in normal dispersion region in presence of higher order dispersion [34]. When the sidebands ($\omega \pm \Delta\omega$) grow large enough, they can generate further sidebands at $\omega \pm m\Delta\omega$ (for $m=2,3,\dots$) and cascade the process as shown in Figure 2.4 [15, 33]. This method makes it possible to generate a train of optical pulses with precise control of repetition rate [27]. MI also plays an important role in generation of optical rogue waves [35] and supercontinuum generation [36].

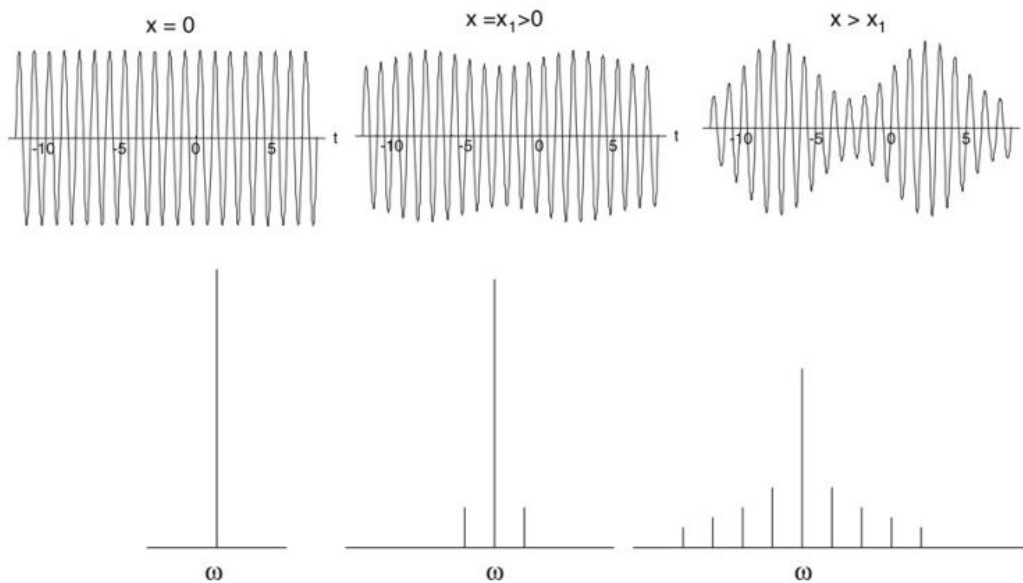


Figure 2.4: New frequency generation due to modulation instability (top) evolution of wave train in time (bottom) corresponding spectral evolution [33].

2.3.7 Dispersive wave generation (Cherenkov radiation emission)

A fundamental soliton can dissipate part of its energy into dispersive wave in higher order dispersion regime. Energy transfer between soliton and dispersive wave is governed by phase matching condition where both soliton and dispersive wave have the same phase velocity. Dispersive waves are also known as Cherenkov radiation or nonsoliton

radiation [27]. The section 6.5 in Chapter 6 discusses this topic in detail.

2.3.8 Four wave mixing (FWM)

Four wave mixing is a nonlinear process where two or three wavelengths interact in a medium to produce two or one new wavelengths [37]. Stimulated FWM in silica fibers was first observed by achieving phase matching by the dispersion of the propagating modes and compensating for the bulk dispersion externally [38]. FWM is explained with the help of energy level diagram in Figure 2.5. When two (or more) input frequency components ω_1 and ω_2 (such that $\omega_1 > \omega_2$) are propagating in a nonlinear medium, a refractive index modulation can occur at difference frequency creating two additional frequency components. The new frequency components can be written as $\omega_3 = \omega_1 - (\omega_2 - \omega_1) = 2\omega_1 - \omega_2$ and $\omega_4 = \omega_2 + (\omega_2 - \omega_1) = 2\omega_2 - \omega_1$. If all four frequencies coincide, it is known as degenerate four wave mixing.

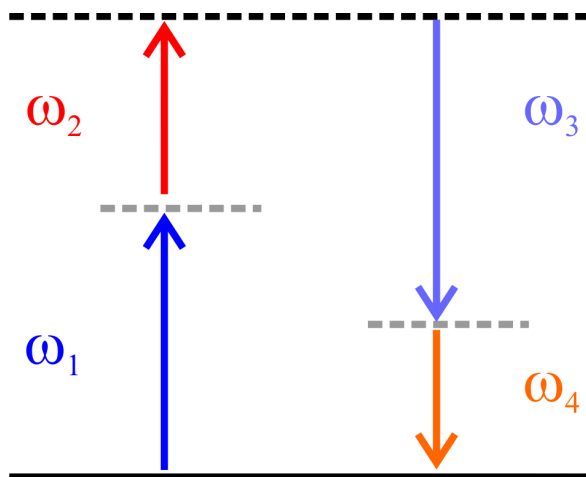


Figure 2.5: Non-degenerate four wave mixing energy diagram. Three input frequencies (ω_1 , ω_2 and ω_3) can phase match to produce output frequency at ω_4 . Thick black line denotes the ground level and top dashed line can be energy level in the nonlinear medium or virtual level.

2.3.9 Supercontinuum generation

Supercontinuum generation (SCG) is a process in which a narrow spectral linewidth laser undergoes extreme spectral broadening in presence of a nonlinear medium. There are various nonlinear processes (discussed above) that can lead to supercontinuum generation. SCG has been observed in crystals [39], liquids [40], semiconductors [41],

gases [42], and also in fibers [8]. Dispersion profile of the fiber plays an important role in the generation of supercontinuum. Chapter 4 discusses the unique dispersion characteristics of the ARHCF and chapter 6 explains the SCG in the gas-filled ARHCF having novel dispersion profile.

2.3.10 Stimulated inelastic scattering

The nonlinear effects discussed until now are governed by third order susceptibility $\chi^{(3)}$. All these processes are elastic nature where there is no energy transfer between the propagating wave and the medium. There are two important inelastic nonlinear process that are observed in the optical fibers and known as

- stimulated Raman scattering (SRS)
- stimulated Brillouin scattering (SBS)

In SRS and SBS, the pump photon is annihilated to produce a photon with lower energy and a phonon. The scattering process conserves energy and momentum. When the phonon with right energy and momentum is available, pump photon can create a new photon at higher energy. The main difference between the SRS and SBS is in their dispersion relation with acoustic and optical phonons [27]. Normally, SRS is observed when pumped with continuous wave or short pump pulses (pulse width of >1 ns) as the walk-off length exceeds the fiber length. For ultrashort pulses (<10 ps), SRS is limited by group velocity mismatch and other elastic nonlinear interactions become prominent. But, intrapulse Raman scattering is of significant importance for pulse width of <1 ps and can induce frequency shift due to Raman scattering in pulse spectrum towards longer wavelength [27, 43–45].

SBS ceases to occur for ultrashort pulses due to its gain bandwidth effect [27]. This effect does not play a significant role in this work and is introduced here for completeness of the discussion.

3 Antiresonant Hollow-Core Fiber

As an effort towards developing low-loss optical waveguides in SiO₂-Si multilayer structures, guidance by antiresonant reflection was first explored in 1986 [4]. Few years later in 1993, the theoretical analysis of antiresonant waveguides provided leaky mode solutions to the wave equation paving steps towards realization of ARHCFs [5]. Fundamental principle to guide light in ARHCFs is the confinement of light in the region of low refractive index by antiresonant reflection between the boundary of low and high refractive index materials. Such a propagation mechanism is observed in hollow core fibers like Kagome fiber [46–49] also. However, the ARHCFs haven been attracting a great interest in recent years due to simple fiber geometry and having advantageous fiber properties like

- broadband transmission window from ultraviolet to mid infrared except at resonance wavelengths
- fundamental mode propagation across complete transmission region
- high damage threshold due to mode propagation in hollow core
- negligible nonlinearities due to minimal overlap between the propagating mode and the waveguide material
- GVD variation due strand resonance wavelength of the ARHCF by few orders in magnitude
- choice of nonlinear media that can be filled in the ARHCF (e.g. inert gases, Raman-active gases, liquids, etc ...)
- and simple fiber structure with an ease of fabrication.

With such excellent properties, ARHCFs have been finding applications in different fields of science and technology like high energy pulse delivery [50, 51], supercontinuum generation [23], mid-infrared fiber lasers [52], pharmaceutical sensing [53], surgical applications [54], few cycle pulse generation [55].

This chapter briefly explains different hollow core fibers and how it lead to design of ARHCF in section 3.1. Section 3.2 introduces various different types of ARHCFs and their unique properties. Section 3.3 details the light guiding mechanism in ARHCF and its characteristics are explained in section 3.4. Penultimate section 3.5 introduces different fiber structures that are used in this work and the final section 3.6 summarizes the different types based on their parameters with a focus on supercontinuum generation and few cycle pulse generation.

3.1 Types of Hollow Core Fibers (HCF)

There has been a continuous interest in the study of propagation of light through HCF since one of the early papers published by Marcatili and Schmeltzer [16]. With the advent of fiber drawing technology various different types of hollow core fibers have surfaced in the last two decades and new fiber designs are still rolling out. The photonic crystal fibers (PCF) have a solid core and a cladding consisting of tiny and closely spaced air holes which run along the length of the fiber. Variation in the size of the hole, pitch and pattern provides additional degrees of freedom in the fiber design and control fiber properties like loss profile, dispersion, mode area etc. [56–58]. Further, this concept extended to design of photonic bandgap fibers (PBG) where the light was confined within a hollow core in silica-air PCF [59]. This design allowed low loss transmission of light in certain narrow wavelength bands where the confinement is provided by two-dimensional band gap due the fiber design structure. This section explains different types of HCFs like HC-PCF [59], Kagome HC-PCF [60], photonic bandgap fibers [61], hypocycloid Kagome HC-PCF [62], single ring ARHCF [18, 63, 64], negative curvature ARHCF [65–68] etc.

Figure 3.1 shows few of the prominent hollow core fiber designs. Figure 3.1a shows the first two dimensional photonic bandgap fiber supporting single mode propagation in air core. One for the design requirements of such a fiber is precise location of periodic

air holes which have high air filling fraction [59]. However PBGs transmit in a very narrow spectral region requiring new fiber design for a new application at a different wavelength.

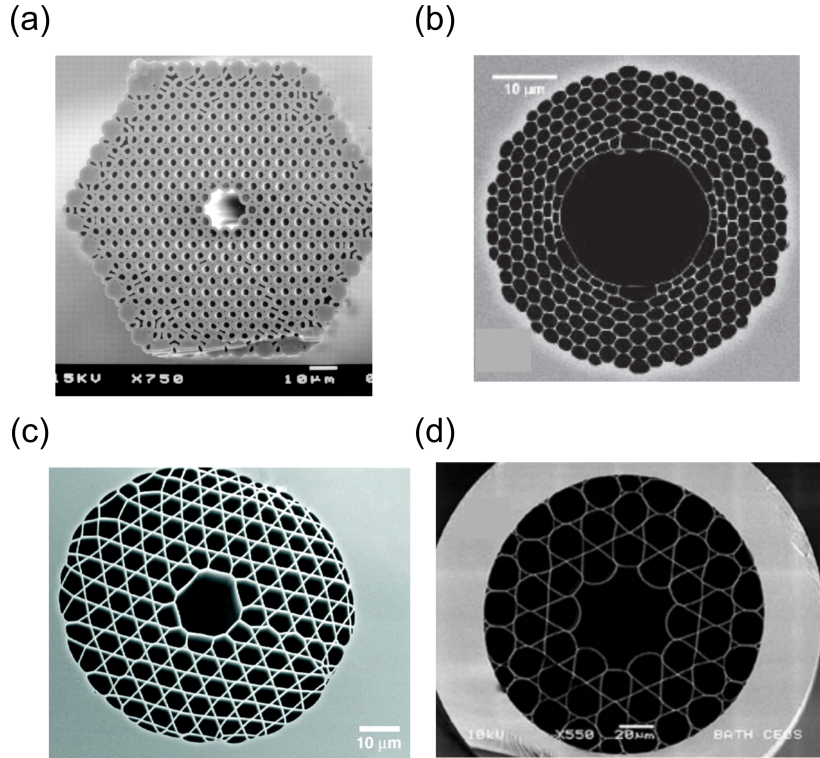


Figure 3.1: SEM images of different types of HCFs: (a) the first photonic bandgap PCF [59], (b) sophisticated PBG-PCF design that is immune to bending losses for bending radius of 5 cm [61], (c) Kagome HC-PCF [60], (d) hypocycloid Kagome HC-PCF [62].

Figure 3.1b is hollow core PBG fiber fabricated by removing 37 cells in the center. This fiber has a narrow band transmission at around $1.05 \mu\text{m}$ supporting fundamental propagation mode. Such fiber designs are immune to bend losses. The fiber in Figure 3.1b is tested down to bend radius of 5 cm making the overall footprint of the application very small [61].

Figure 3.1c shows Kagome type HC-PCF fabricated by removing seven capillaries in the fiber to form hollow core. Such structures transmit light over a large spectral region spreading over an octave bandwidth. These large core fibers have an advantage to study nonlinear interactions between laser and gas or liquid materials that can be filled in the fiber core. This particular fiber was filled with hydrogen to study stimulated Raman scattering [60].

Figure 3.1d shows an extension of Kagome fiber design where the inner core is

fabricated as seven-cell hypocycloid-core structure [62]. This design inhibits coupling between the core and cladding modes trapping the propagating light in the core mode for broad spectral bandwidth with low loss, unlike PBG fibers.

Continuous development in the HCF design over the years have led to understanding of various different fiber parameter that play a role in fiber performance. At the same time, such designs have resulted in complex fiber core-cladding structures bringing a new challenges in fiber drawing process and limiting possible applications. Antiresonant hollow core fibers combine many advantages that are offered by different HCFs and have a simple fiber structure with an ease to draw the fibers. Next sections will detail types of antiresonant hollow fibers and their advantages.

3.2 Types of ARHCFs

Over the last decade, an exponential increase in design of ARHCFs is observed. Though ARHCFs have simpler fiber structure, there are different design properties through which one can control transmission spectrum of the fiber, position of fiber resonance, dispersion tuning, selective mode guidance (fundamental mode or higher order mode in the core), polarization control of the propagating mode, attenuation at specific wavelength etc. One or more of these different parameters can be incorporated in fiber design. Broadly ARHCFs can be classified into the following categories:

- single ring structure [63, 64]
- negative curvature core structure [65, 66]
- nodeless ARHCF [67, 68]
- nested nodeless ARHCF [69]
- hypocycloid core contour [21]
- double revolver [70]
- positive and negative curvatures nested inside ARHCF [71]

Figure 3.2 shows different types of fiber geometry. Figure 3.2(a-e) shows the drawn fibers and Figure 3.2(f-g) correspond to theoretical designs. Each of these different fiber

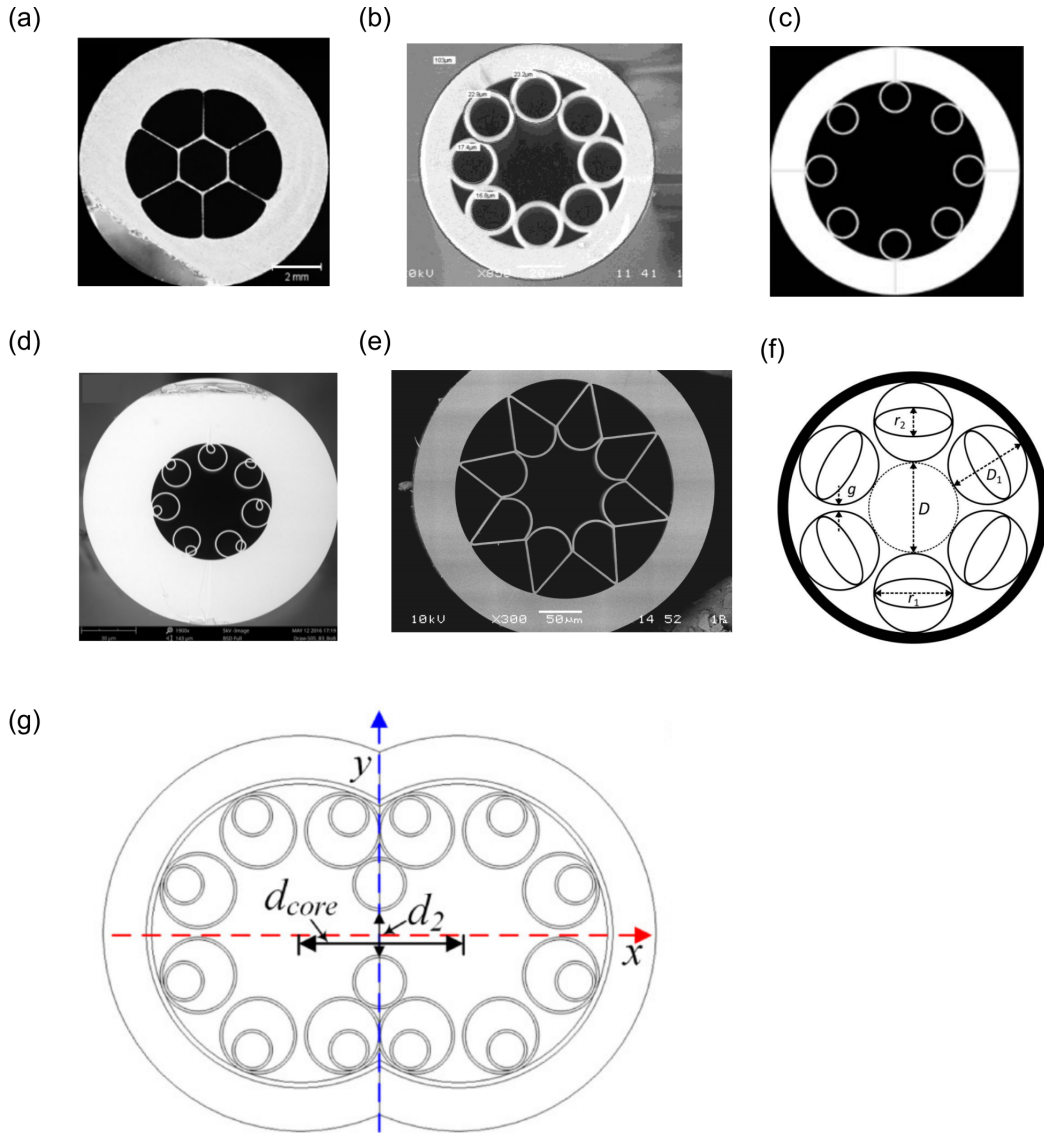


Figure 3.2: SEM image of different types of ARHCFs (a) single ring structure [63], (b) negative curvature core structure [72] (c) nodeless ARHCF [67] (d) nested nodeless ARHCF [73] (e) hypocycloid core contour [21] (f) positive and negative curvatures nested inside ARHCF [71] (g) dual core [74].

designs have unique applications like Raman sensing in single ring structure [63], light propagation beyond $3.5 \mu\text{m}$ in silica based negative curvature ARHCF [72], further addition of nests in the nodeless ARHCF can further reduce the confinement losses while maintaining multioctave propagation bandwidth [69, 71], transmission in mid IR spectral region in hypocycloid core contour [21], and dual core ARHCFs can pave way towards efficient mode-coupling between two independently propagating modes [74]. Possible applications of ARHCFs are ever increasing due to its salient features and simple structure. This work focuses on less explored single ring ARHCFs in terms of dispersion,

polarization evolutions, laser-matter nonlinear interactions in gas filled fibers. The penultimate chapter discusses few cycle pulse generation in negative nodeless negative curvature ARHCF.

3.3 Guiding mechanism

The antiresonant reflecting optical waveguide (ARROW) model [4, 75] provides physical insight and predicts accurately the high-loss features of anti-resonant hollow-core fibres. The glass strand (see Figure 3.3) that forms the fibre core can be considered as Fabry-Perot etalon having characteristic transmission resonances depending on the thickness of the strand t . When the core diameter is very large compared with propagating wavelength i.e. $d \gg \lambda$, wave vector in longitudinal direction (k_L) is given by

$$k_L \approx n_0 k_0 \quad (3.1)$$

and transverse wave vector inside the stand material can be approximated to

$$k_T \approx k_0 \sqrt{n_1^2 - n_0^2} \quad (3.2)$$

where $k_0 = \frac{2\pi}{\lambda_0}$ is the wave vector in vacuum. The incident light on the strand (as shown by the continuous red arrow entering the strand from the left side in Figure 3.3) can pass through the strand with and without multiple reflection(s) (as denoted by the dotted red arrow lines in Figure 3.3). The phase difference between the light passing through the strand with and without reflection is given by

$$\delta\varphi = \varphi_1 - \varphi_0 = 2tk_0 \sqrt{n_1^2 - n_0^2} \quad (3.3)$$

When $\delta\varphi$ is equal to multiple of 2π , strand resonance condition is expressed as

$$\delta\varphi = \varphi_1 - \varphi_0 = 2m\pi \quad (3.4)$$

for $m = 1, 2, 3, \dots$ and strand thickness t can be calculated for air filled core

$$t = \frac{m\lambda}{2(n_{glass}^2 - n_{air}^2)} \quad (3.5)$$

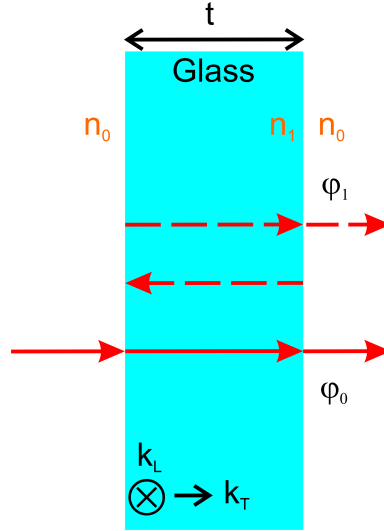


Figure 3.3: ARHCF strand having thickness t . Refractive index of the strand material (glass) is n_2 and refractive index of the medium surrounding the strand is n_1 (equal to 1 for air).

Strand resonance wavelength is given by

$$\lambda_m = \frac{2t\sqrt{(n_{glass}^2 - n_{air}^2)}}{m} \quad (3.6)$$

All the wavelengths that satisfy Eq. 3.6 leak from the core of the fiber into cladding and are lost.

The following antiresonant condition need to be satisfied by the propagating mode to be confined within the core

$$\delta\varphi = \varphi_1 - \varphi_0 = (2m - 1)\pi \quad (3.7)$$

and corresponding strand thickness is given by

$$t = \frac{(m - 0.5)\lambda}{2\sqrt{(n_{glass}^2 - n_{air}^2)}} \quad (3.8)$$

3.4 Characteristics of an ARHCF

This section introduces salient characteristics of the ARHCF that is used in this work. The fiber (shown in Figure 3.4) considered here is a single-ring large core ARHCF having core diameter of $\sim 50 \mu\text{m}$. The inner ring is supported by thin silica strands

that form the cladding. This particular fiber is referred as hexagon core fiber in the rest of the work presented here.

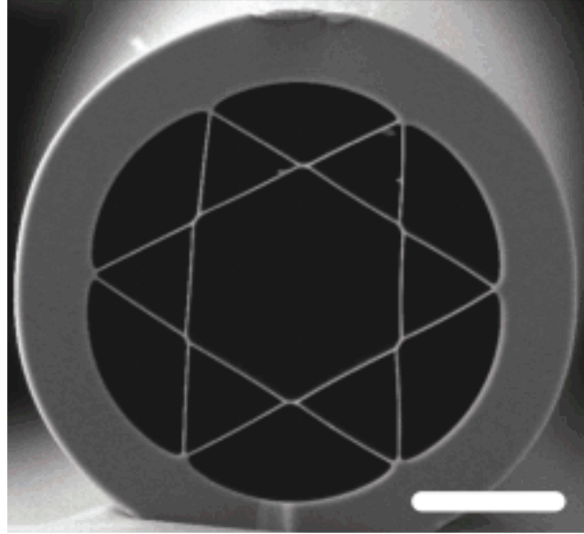


Figure 3.4: Scanning electron microscopy (SEM) image of the single-ring hexagon core ARHCF cross-section. White horizontal bar corresponds length of 50 μm . GVD of this fiber is characterized and used in supercontinuum generation (discussed in Chapter 6).

3.4.1 Spectral distribution of the losses in the ARHCF core

The average strand thickness of the hexagon core ARHCF is ~ 495 nm. This corresponds to fundamental resonance at ~ 1 μm . Cut back method shows fiber transmission from UV to IR. The propagation losses vary from 5 dB/m in the UV-VIS region to 10 dB/m in the IR region (see Figure 3.5). The strand thickness varies by $\sim 10\%$ along the length of the fiber which broadens the resonance region. Theoretically, the losses in ARHCF arise from the Fresnel reflections that occur at the boundary of the core with silica strands that form the core. These losses are unavoidable. Though, tighter light confinement in smaller cores may increase the losses, the technological limitations of fiber drawing are defining the limits of the losses of today's ARHCF. ARHCF losses depend on the strand thickness and its variation during the fiber drawing process. An ideal ARHCF having a fixed strands thickness of t will have losses at a fixed wavelength given by the Eq. 3.6 , which means at all other wavelengths there are no losses. However, due to challenges in maintaining the variation of strand thickness in fiber drawing process, the actual fiber will have strand thickness of $t \pm \Delta t$ increasing the resonance spectrum to $\lambda_m \pm \Delta\lambda$. For $t \sim 495$ nm, the first order resonance wavelength (λ_1) corresponds

to ≈ 1000 nm for silica fiber. 10% variation in strand thickness during fiber drawing process results in $\Delta\lambda$ of ± 100 nm. This broadens the resonance spectrum by ~ 200 nm.

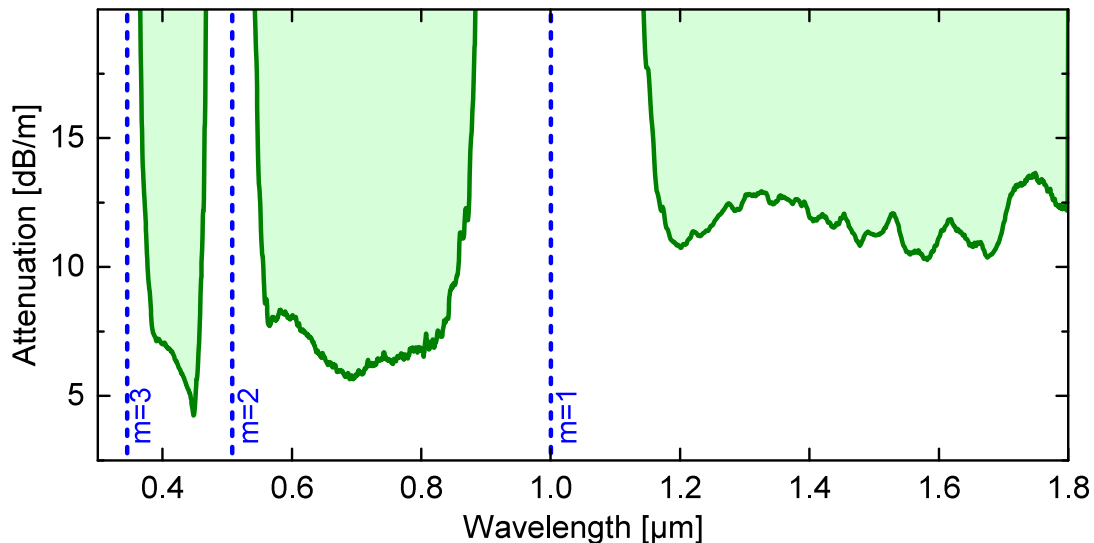


Figure 3.5: Measured loss profile of the hexagon core ARHCF.

One of the distinct advantages of ARHCF is that it does not follow the capillary loss formula where the losses increase as the cube of the core diameter. Hence, confinement losses do not play a major role in experimental work. Further, experiments that study nonlinear laser-matter interaction in gas-filled ARHCF use short length of fiber between 20-25 cm where overall propagation losses are not critical and ARHCF with smaller core size assures tighter light confinement enhancing the nonlinear interactions.

3.4.2 Effective refractive index at resonance

Effective refractive index in ARHCF follows cylindrical waveguide index as explained by Marcatili and Schmeltzer [16]. However, strand resonances strongly influence effective refractive index at resonance wavelengths. Finite element simulations for the hexagon fiber shows a sudden change in the effective refractive index at $\lambda_1 = 1 \mu\text{m}$ (see Figure 3.6: left Y-axis, shown in red). This modifies dispersion profile of the fiber significantly and GVD can vary by orders in magnitude [76]. Corresponding loss due to resonance is also shown by blue curve (right Y-axis). Chapter 4 explores in detail on characterizing such a complex GVD pattern near resonance wavelength.

The hollow core structure of the ARHCF provides an additional choice of injecting gases (or liquids) in the core which can further change the effective refractive index. It is also possible to shift the dispersion curve and zero dispersion wavelength by controlling the gas pressure inside the fiber [15].

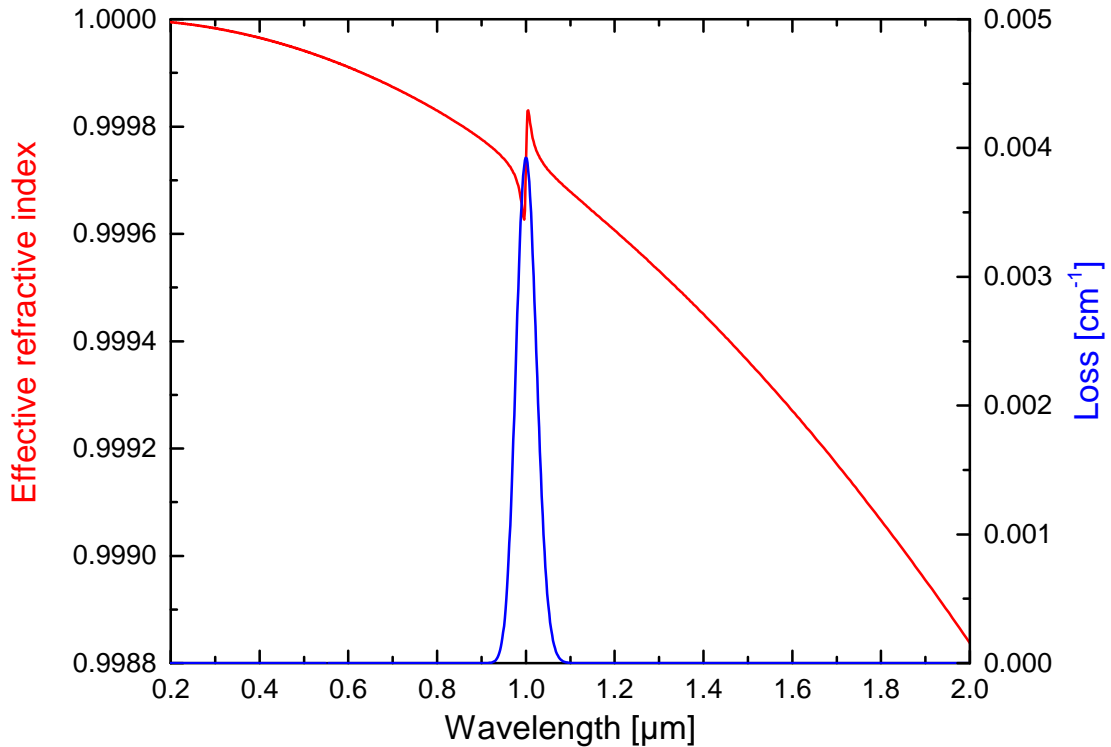


Figure 3.6: Variation in the effective refractive index of the fundamental mode in ARHCF due to resonance (in red) and corresponding loss (in blue) calculated by FEM simulations. The effect of higher order resonances i.e. for $m > 2$ are smoothed as only first order resonance plays a dominant role in the experimental work.

3.5 Antiresonant fibers used in this work

This work is carried out in four different of ARHCFs having different geometries. Hexagon core ARHCF (Figure 3.4) is characterized for dispersion and is chosen for supercontinuum generation as the resonance is situated closer to the Ti:Sapphire pump wavelength. Polarization evolution in single ring ARHCF involves three different polygon core shapes (square core, hexagon core and nonagon core) as shown in Figure 3.7. Individual fiber properties are discussed in Chapter 5.

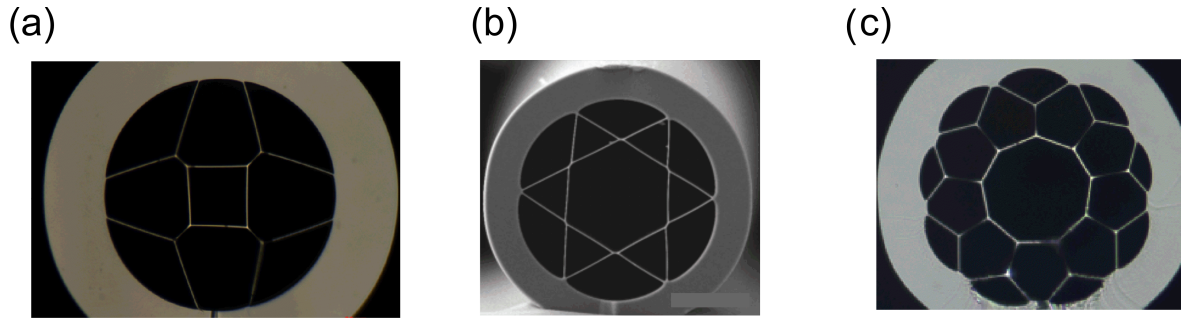


Figure 3.7: SEM images of ARHCFs used in this experiment (a) Square core (b) Hexagon fiber (c) Nonagon fiber.

Few cycle pulse generation at $1.75 \mu\text{m}$ is carried out in nodeless ARHCF and is as shown in Figure 3.8. This negative curvature ARHCF transmits light into mid IR wavelengths beyond silica cut-off wavelength. Details of this fiber is discussed in Chapter 7.

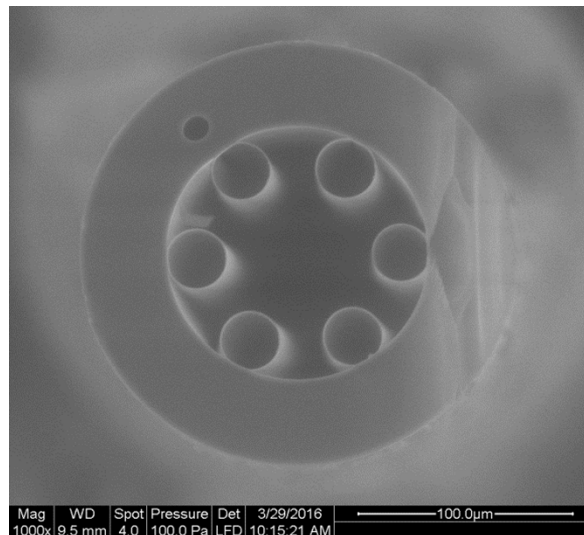


Figure 3.8: SEM image of nodeless negative curvature ARHCF used to generate few cycle pulses (discussed in Chapter 7).

3.6 Summary

This section compares the different fiber types discussed in this chapter and summarises the important fiber parameters that are essential for supercontinuum generation or few cycle pulse generation experiments. Table 3.1 lists different types of fibers based on their operation bandwidth, propagation losses, fiber structure which manifests into ease of fabrication and damage threshold.

Fiber type	Core type	Operational bandwidth	Propagation loss	Fiber structure	Damage threshold
Solid-core-clad fiber	Solid	Narrowband	Low	Simple	Low
Capillary fiber	Hollow	Broadband	$\propto \frac{\text{wavelength}^2}{(\text{core dia})^3}$	Simple	High
Solid-core PCF	Solid	Broadband	Low	Somewhat complex	Low
PBG fibers	Hollow	Narrowband	Low	Somewhat complex	High
Kagome fibers	Hollow	Multi-octave	Low	Complex	High
ARHCF	Hollow	Multi-octave	Low	Somewhat complex	High

Table 3.1: Comparison of different silica fibers for supercontinuum generation and few cycle pulse generation

The hollow core fibers have higher damage threshold when compared with solid core fibers for obvious reasons. Though most of the fibers provide low propagation losses in their operational bandwidth, the Kagome fibers and the ARHCFs support multi-octave propagation bandwidth making them more suitable for supercontinuum generation or few cycle pulse generation. Structure of the fiber defines the ease of fabrication. Simpler structures like capillary fibers are easy to fabricate when compared with any PCFs. However, the losses in capillary HCFs are inversely proportional to cube of its diameter. In spite of having many favourable parameters, the loss factor significantly limits their operation as reduction in the diameter is the only way to increase nonlinearity in this fiber. The ARHCFs tend to have less complicated structures amongst the PCF and are favourable candidates to explore efficient nonlinear laser-matter interactions in gas-filled fibers.

Part II: Linear properties of ARHCF

4 Dispersion Measurement of Antiresonant Hollow Core Fiber

In the recent years, one of the rapidly developing applications of microstructured hollow-core fibres has been their usage as a mediator for nonlinear optical interactions of ultrashort pulses and gases [15, 77]. Further, ARHCFs also have a great potential applications in the field of telecommunication which has strong industrial applications across the world [78, 79]. All such practical applications require precise information of group velocity dispersion (GVD) of the waveguide. The light passing through a waveguide gets influenced by the properties of the medium through which it propagates. When light is coupled into an optical fiber, propagating light gets confined within the boundary of the waveguide in radial direction. Light propagates either by total internal reflection, photonic bandgap effect, inhibit coupling, or via antiresonant mechanism. When the intensity of the input light is above certain threshold, it undergoes different nonlinear processes by interacting with its surroundings. E.g. a given pulse can experience a characteristically different nonlinear effects like self phase modulation and self steepening effects in normal dispersion region ($k'' = \frac{\partial}{\partial \omega} \left(\frac{1}{v_g} \right) > 0$; where v_g is group velocity of light and is function of wavelength (λ)) and soliton dynamics plays a crucial role in the anomalous dispersion ($k'' < 0$).

Theoretical analysis show that the GVD of the ARHCF changes in large magnitude near resonance wavelengths [76]. As discussed in Chapter 3, position of resonance wavelength in an ARHCF can be engineered by controlling the thickness of the core strand during fiber drawing process. This means, it is possible to position a unique and significant dispersion profile at a desired wavelength. This chapter discusses an interferometric method to quantitatively measure such a dispersion change which can give an additional freedom in fiber design for niche applications both in linear operations like

dispersion compensating fibers and nonlinear operations like supercontinuum generation. In addition, such GVD profiles are independent of core diameter enabling high power (energy) operation giving a boost towards scaling nonlinear laser matter interactions in hollow core fibers without ionizing the gas filled in the fiber core.

This chapter details interferometric set up to measure GVD in Section 4.1. Section 4.2 explains the experimental measurement and data analysis steps. The measured GVD results are discussed in section 4.3 and summarized in section 4.4.

4.1 Experimental setup to measure GVD

The GVD of the ARHCF is characterized with the help of conventional interferometry technique. Experimental set up is a balanced Mach-Zehnder interferometer (MZI) where both sample and reference arms have identical optical elements to cancel the effect of dispersion experienced by propagating light due to optical elements that form the interferometer. In a MZI, collimated light from a single source is split and made to go through two different arms. One arm is called reference arm and the other arm is called sample arm. The beams from the two arms are combined again to produce interference pattern. The observed interference pattern contains the relative phase shift differences between the two arms. Any transparent object under test like an optical fiber can be placed in the sample arm and it is possible to measure the relative phase differences between the light passing through the two arms. When a broadband light source is placed at the input, it is possible to measure relative phase difference as a function of wavelengths. This can be characterized to obtain GVD of the test object.

Theoretical calculations show that the GVD of the AHRCF away from resonance region is same as that of hollow capillary having same core diameter. But, an abrupt GVD increase of few orders of fs^2/cm in magnitude is predicted by FEM simulations in the resonance spectral region which has high attenuation of the order of 20-30 dB/m. Hence, a 9.7 cm long hexagon ARHCF is placed in a balanced MZI (as shown in Figure 4.1) such that interference can be observed not only across broad bandwidth having low GVD profile, but also close to lossy resonance region.

A fiber based white-light supercontinuum source from *Fianium* is used as source. The pump peak from the source spectrum is attenuated using a color filter (*Thorlabs*

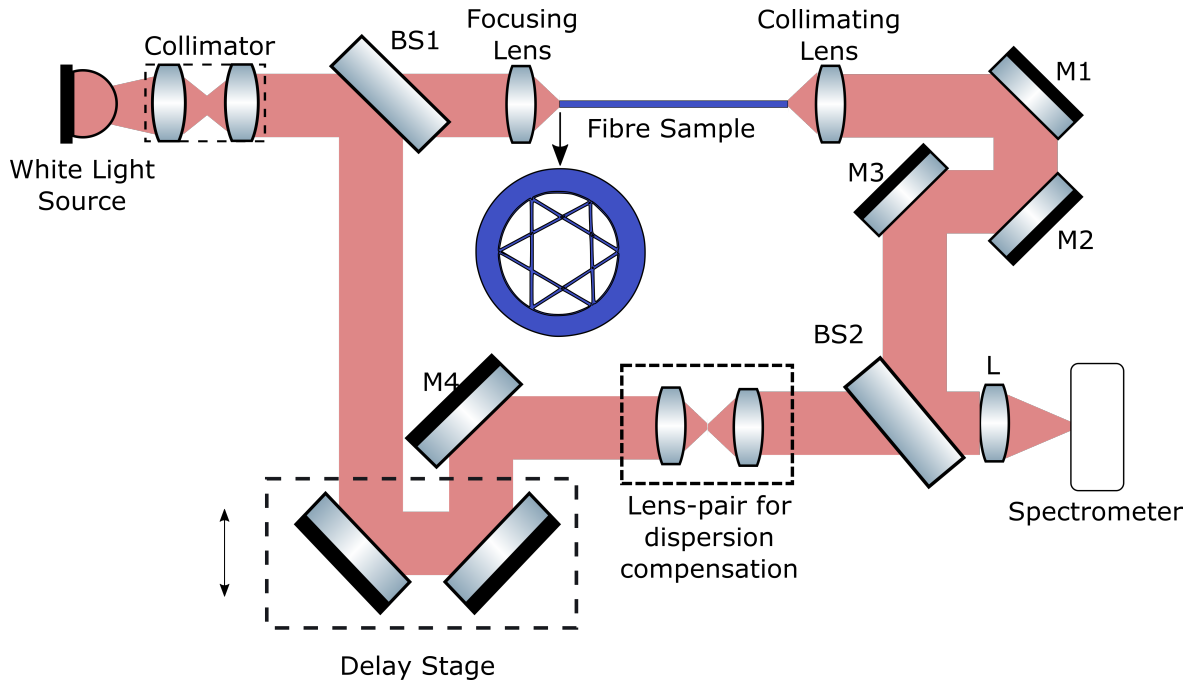


Figure 4.1: Sketch of the experimental setup used to measure GVD of the ARHCF (details can be found in the main text)

FGS900). Two identical glass plates form beam splitters BS1 and BS2. Through BS1, $\sim 96\%$ of the input light passes into sample arm and the remaining $\sim 4\%$ is reflected by Fresnel reflection into the reference arm. A focusing lens having focal length of 30 mm couples the light in the sample arm into the ARHCF (placed on *Thorlabs* Nanomax stage) and an identical lens collimates the output at the exit of the fiber. A similar lens pair is also placed in the reference arm to balance the interferometer. A delay stage in the reference arm compensates extra path length (if any) that propagating light travels in the sample arm so that light from both the arms fall on the beamsplitter BS2 at the same time to recombine and produce the required interference pattern. At lens L, $\sim 4\%$ of the light from the sample arm (i.e. reflected by BS2) and $\sim 96\%$ of the reference arm light gets recombined such that approximately equal intensities of the light interfere and produce fine interference pattern. The recombined collimated beams are focused on to the spectrometer entrance to record finely spaced interference fringes on a high-resolution spectrometer (*OceanOptics* HR4000).

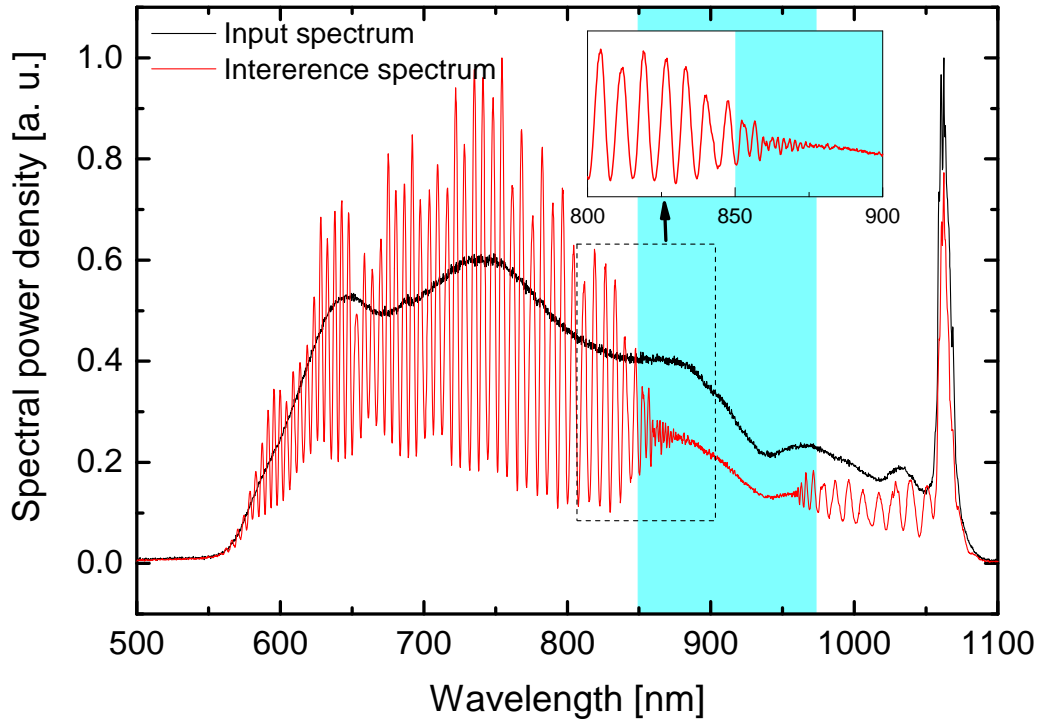


Figure 4.2: Recorded spectral interference fringes (in red) [inset: close up view of interference fringes near the resonance]. Resonance region is shown in blue shade.

4.2 Measurement and Analysis

The recorded interference fringe pattern for the fundamental fiber mode extends in wavelength from 550 nm to 1100 nm covering both sides of the resonance region as shown in Figure 4.2. The inset of Figure 4.2 highlights the denser spectral fringe pattern measured into the resonance spectrum. The high attenuation due to transmission of propagating light into cladding in the resonance region limits measurement of continuous GVD across the resonance spectrum. Dispersion profile of the ARHCF as a function of wavelength can be obtained by extracting the phase information from the recorded interference pattern. There are different methods like stationary phase point method, minima-maxima method, phase modulated cosine function fit method, Fourier-transform method, windowed Fourier-transform method which can be used to obtain the phase information [80]. Advantages and disadvantages of all the methods are compared in detail in the Ref. [80]. Fourier method is selected for data analysis here as it is possible

automatize the process and requires single interferogram enabling direct measurement of the spectral phase. This method is immune to reduced sensitivity to the amplitude near resonance region. Further losses in the interferometer arms like scattering and absorption do not affect the phase retrieval process. This methods enables phase extraction at all the wavelength points where the interference has been recorded.

4.2.1 Phase retrieval

Mathematically, the recorded spectrogram can be represented as

$$S(\omega) = S_r(\omega) + S_s(\omega) + 2\sqrt{S_r(\omega)S_s(\omega)} \cos \varphi(\omega) \quad (4.1)$$

where $S_r(\omega)$ and $S_s(\omega)$ are the power spectral densities in reference and sample arm, respectively, $\varphi(\omega)$ is the phase difference between optical fields of the two arms and contains the information of dispersion profile of the fiber. The following steps explain the phase retrieval from the measured interference spectrum:

- Interference spectrum with respect to wavelength is converted to angular frequency. Interference spectrum with respect to frequency is interpolated to obtain linearly spaced frequencies.
- Fourier transform of the spectrogram over the new frequency scale is calculated and one side of Fourier time-domain values are selected. Fourier time-domain values correspond to the delay between the two arms i.e. when the reference arm is shorter than the sample arm the reference pulse is behind the sample pulse so the delay is negative. Then left part of the spectrum is filter out and vice-versa.
- Chosen Fourier time-domain values undergo inverse Fourier transform to provide the phase values (shown in Figure 4.3).

Extracted phase from the recorded interference fringes of Figure 4.2 are shown in Figure 4.3 (in black). Uniform interference fringe pattern away from the resonance maintain a constant slope. But a sudden change in slope in the vicinity of the resonance is distinctly observed due to an increase in the density of interference fringes. Differentiating the extracted phase twice with respect to angular frequency (ω) provides the dispersion curve. The direct differentiation of the extracted phase leads to large

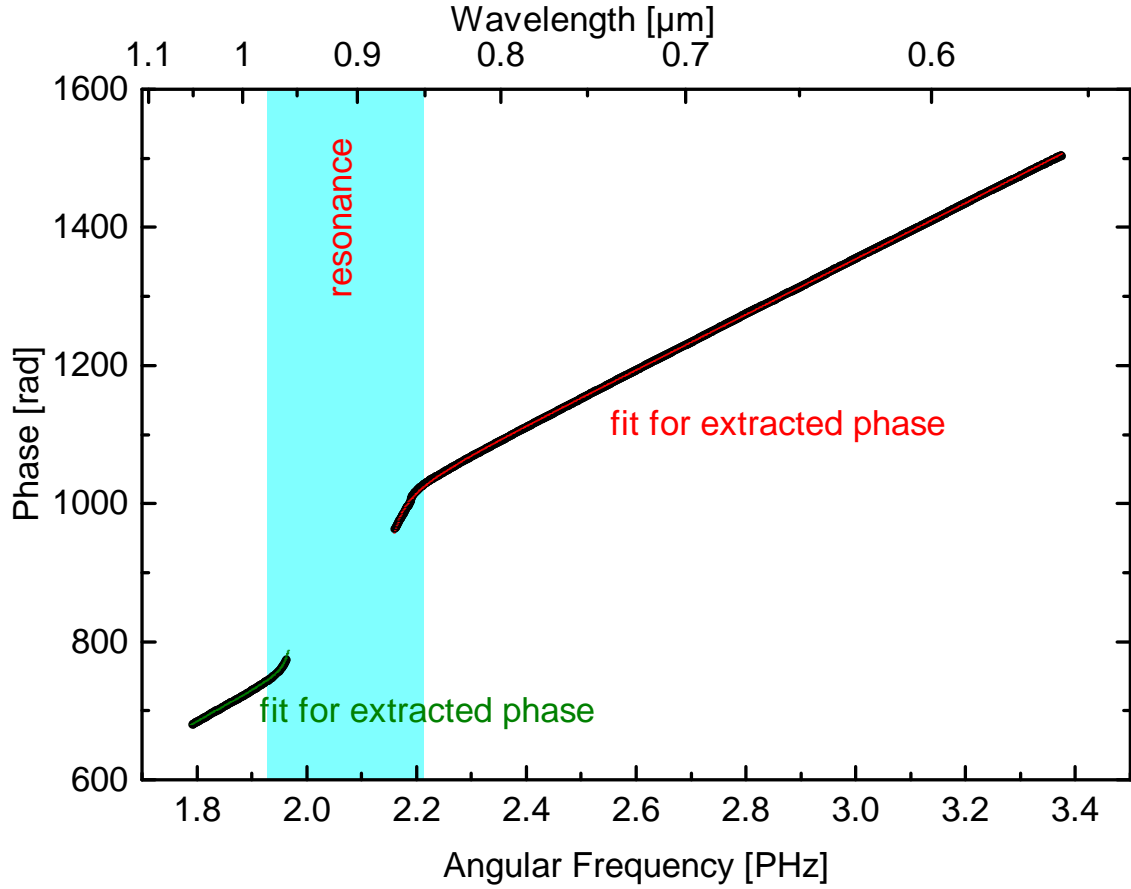


Figure 4.3: Extracted phase from the interference pattern in Figure 4.2 is shown as (black line). Mathematical fit with Lorentzian-like resonances are shown in colour, red coloured fit for higher frequencies (towards blue side of the resonance region) and green coloured fit for lower frequencies (towards longer wavelengths from the resonance).

numerical error and hence it requires a mathematical fit. In this work it is difficult to define a fit for the phase as a function of angular frequency (ω) where the fit needs to represent both high and low frequency terms. Traditional Taylor expansion cannot be used in this scenario.

The strands that form the fiber core behave as high-finesse Fabry-Perot etalons for mode propagation under oblique incidence angle. In such cases, modal properties can be calculated by considering the wave as a reflection of planar film as operating wavelength is much smaller when compared with core diameter [76]. Further, Lorentzian-type line shape functions that are comparable to Sellmeier equations can provide a better fit for such phase evolutions [23]. Eq. 4.2 is the function used to fit the extracted phase shown in Figure 4.3.

$$\varphi = P\omega \sqrt{1 - \frac{A}{\omega^2} - \frac{B(\omega - C)}{(\omega - C)^2 + D}} \quad (4.2)$$

where the fitting terms P and A correspond to hollow core capillary dispersion, and the remaining terms B, C, D corresponds to resonance. The fitting parameter [P] is dimensionless and the remaining parameters [A], [B], [C], and [D] have dimensions [s^{-2}], [s^{-1}], [s^{-1}], and [s^{-2}], respectively. A single resonance fit is sufficient for GVD measurement and also results are acceptable for practical applications as shown in Refs. [23, 81]. Defining multiple resonances might reduce the mathematical error of the fit, but have no practical significance as they lead to additional modulations at unexpected resonance frequencies during GVD calculation. Hence, further analysis limits to single resonance picture.

The extracted phase information is available from 550 nm to 1050 nm except at the center of the resonance where no fringes are observed. The transmission region between the first two resonance orders ($m=1, 2$) i.e. between spectral range from 570 to 860 nm is of special interest as this fiber is used to study spectral evolution in gas filled ARHCF with Ti:Sapphire laser system providing pump wavelength at 800 nm. For a fixed delay of the MZI, 10 spectrograms are recorded at intervals of 100 μ s. Eq. 4.2 is used to fit extracted phase from each of the spectrograms. The results are obtained by taking average of these measurements.

4.3 Results and Discussion

Every spectrogram has two separate fits, one on each side of the resonance. Results of the calculations are tabulated in Table 4.1 and are differentiated twice with respect to angular frequency to obtain the GVD profile. The values mentioned in Table 4.1 can be used as a starting point for future fiber design.

Figure 4.4 shows the obtained GVD profile of the ARHCF along with calculated GVD of the capillary having similar core diameter. The results show that the low GVD region is similar to capillary GVD behaviour away from the resonance and strongly modifies GVD on both sides of the resonance spectrum. Additionally there exists a zero dispersion wavelength (ZDW) at 705 nm (shown in the inset of Figure 4.4), which exist in capillary fiber much away from the Ti:Sapphire pump wavelength. In Ref [76],

Parameter	Below resonance wavelength		Above resonance wavelength	
	Value	Standard deviation	Value	Standard deviation
P	437.40748	6.03683	416.11277	5.83027
A	-1.69159	0.28612	0.51128	0.07684
B	0.00843	7.24836×10^{-4}	3.7306×10^{-4}	1.16701×10^{-4}
C	2.00917	0.02758	1.9690	0.00113
D	-0.03697	0.06828	7.83588×10^{-6}	4.59314×10^{-6}

Table 4.1: Averaged fitting parameters for extracted phase used to obtain GVD curve shown in Figure 4.4

Eq. 25 qualitatively explains the origin of such a GVD variation in detail.

From the structural perspective, fiber strand width defines the resonance spectral position. This gives an additional tool to engineer the such microstructure fibers position significant GVD variation at a given wavelength as required for any given application, which is not possible in capillary fibers [20, 76]. Dispersion tuning by structural resonance gets stronger with decrease in the fiber core diameter. Such designs have great influence on nonlinear light generation and pulse compression applications.

To further verify the obtained results, GVD is numerically calculated by finite element simulations (FEM) in COMSOL software [82]. The simulation results are shown in blue in Figure 4.4. FEM calculations assume a fixed strand thickness of 495 nm and results show a narrow resonance region. However, the strand thickness has a variation of $\sim 10\%$ due to technological challenges in fiber drawing. These variations run along the fiber longitudinally and also across the fiber cross section. Such changes lead to broadened resonance region from few nanometers to hundreds of nanometers. The COMSOL simulation assumes a fixed thickness in the simulation which results in narrowband resonance region, unlike experimental condition. Hence, COMSOL results are spectrally shifted in wavelength to match experimental measurements for qualitative comparison. Figure 4.4 shows significant overlap between experimental and FEM simulations and confirms the variation in GVD by few orders of fs^2/cm on both sides of the resonance spectrum.

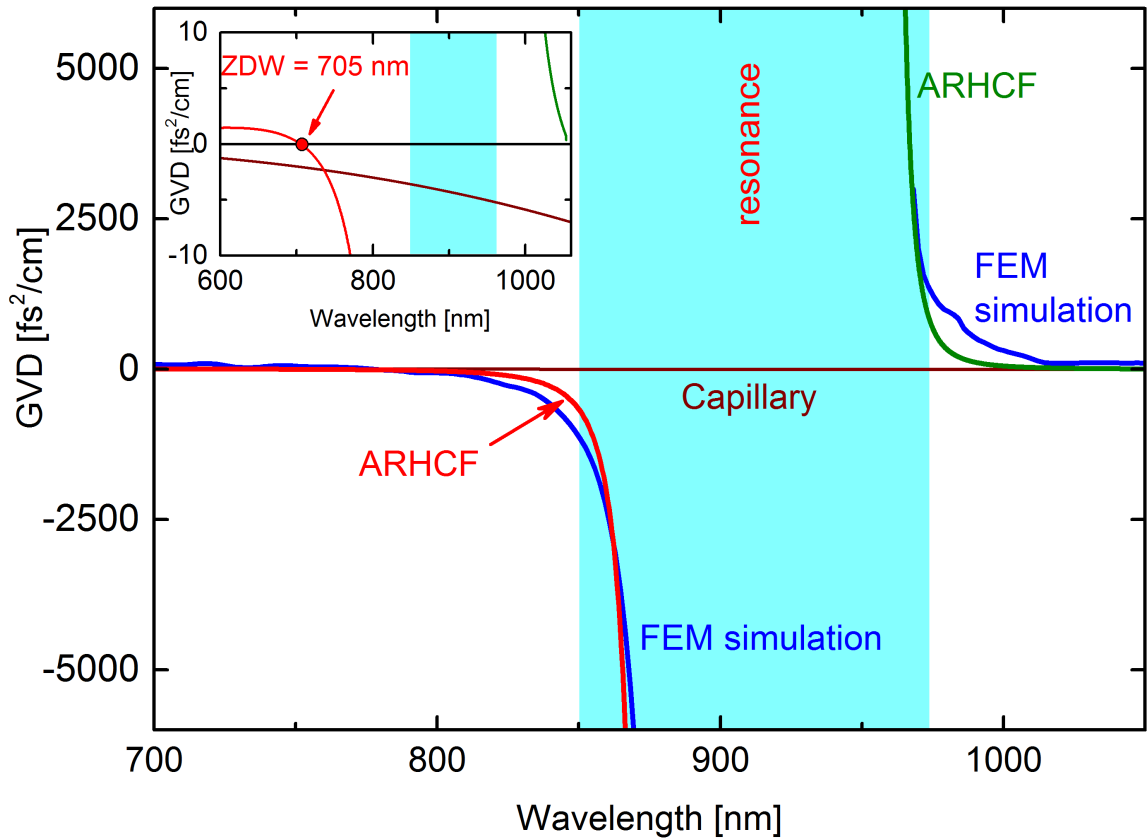


Figure 4.4: Measured GVD obtained from the fit to the measured phase profiles shown in red and green in comparison with GVD of a standard hollow capillary (in brown) having similar core size (by Marcatili-Schmeltzer (MS) model [16]) and GVD calculated the same ARHCF by FEM simulations in COMSOL (blue) [inset: close-up shows the abrupt GVD variation near the fundamental strand resonance wavelength and the ZDW at 705 nm, not present for capillary waveguide].

4.4 Summary

Traditional spectral interferometric method is applied to measure the GVD profile of the single ring ARHCF. The fiber is placed in sample arm of the balanced MZI. Interference fringes are recorded behind the recombination of the propagating light from the sample arm and the reference arm in a spectrometer. These broadband spectrograms provide an information on variation of phase in ARHCF as a function of wavelength. A unique mathematical fit for the phase distribution is applied on each side of the resonance. Differentiation of the phase fit with respect to the angular frequency twice provides GVD profile of the fiber.

It is possible to measure the GVD away from the resonance and in the vicinity of the resonance. Due to inevitable variation in strand thickness and high-attenuation in

the resonance region, it is not possible to make a quantitative GVD measurement at resonance. Experiment confirms few orders of fs^2/cm in the vicinity of the resonance. It is important to highlight that such large GVD is independent of the core diameter and depends on inner dielectric annulus thickness. Such a GVD profile with large core diameters (like $250\ \mu\text{m}$, $500\ \mu\text{m}$, $1\ \text{mm}$, etc.) have potential to scale high power (energy) operations. Strand thickness controls the position of the resonance. Hence, it is possible design fibers where a unique, but significant GVD change can be defined at a given wavelength paving way for niche applications.

5 Polarization Evolution in ARHCF

5.1 Importance of polarization evolution in fibers

The previous chapter introduced the novel dispersion regimes that can be accessed using ARHCF is an added advantage. However, there has been no detailed experimental studies on polarization evolution in ARHCF. Some of the theoretical studies show that it is challenging to achieve high birefringence in antiresonant fibers keeping structural requirements to minimize confinement loss [83] and it is also suggested that flat core walls can have higher birefringence when compared with negative curvature ARHCF [84].

Understanding of polarization properties in any waveguides, here in particular in ARHCF is of fundamental importance to advance knowledge and develop possible photonic devices incorporating unique properties of the fiber. It is challenging to introduce birefringence in negative curvature ARHCF (NC-ARHCF) due to the minimal overlap between the optical mode and the microstructured cladding. Different approaches to control birefringence in these fibers include nested ARHCF [83] and fibers with different strand thickness surrounding the core [84]. It is challenging to introduce large birefringence while maintaining structural requirements in NC-ARHCF. In [84], *Ding et. al.* suggest to use the 1st hybrid band of ARHCF and a square-shaped core to introduce significant birefringence.

This chapter investigates the geometry-induced polarization behaviour of ARHCF with flat core boundaries having different polygon structures. The focus of the study is on the influence of fiber core geometry and its deviations from the ideal regular polygon structure on birefringence. Three different types of ARHCFs having square, hexagon and nonagon core shape are considered for experiments. Figure 5.1 shows the experimental concept to study the dependence of the output polarization state for a well defined input polarization state. As shown in the concept Figure 5.1, a linearly

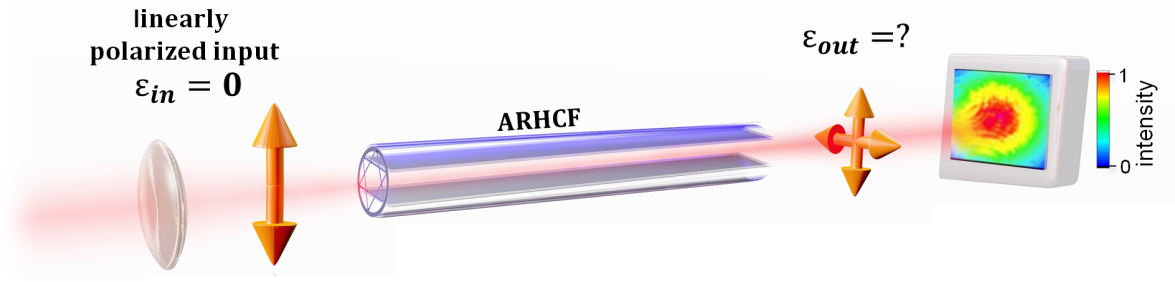


Figure 5.1: Concept figure: a linearly polarized light having $\epsilon=0$ is coupled into the fiber. The experiment tries to measure unknown state of output ellipticity. Excited fundamental mode profile is shown at the fiber output as an example.

polarized light with zero ellipticity ($\epsilon_{in} = 0$) is coupled into a polygon shaped core of an ARHCF to excite the fundamental mode. The state of output polarization (ϵ_{out}) is measured to study its variation with respect to orientation of input polarization and wavelength. The ellipticity value ranges between 0 and 1.

The theory behind experiment to measure polarization evolution is introduced in section 5.2. Transmission property and geometrical parameters of the ARHCF are discussed in section 5.3. Study of impact of core geometry and input wavelength on the output ellipticity is explained in sections 5.5 and 5.6. The section 5.7 discusses the origin of birefringence and the experimental results. Chapter is summarized in section 5.8.

5.2 Theory

Amplitude of a unit electric field vector \vec{E} can be resolved into its projections along horizontal and vertical axes in laboratory frame. It can be described using Jones matrix by $\vec{E} = \begin{pmatrix} A \\ B e^{i\delta} \end{pmatrix}$ where A and B are the normalized horizontal and vertical components of the \vec{E} field and $\sqrt{A^2 + B^2} = 1$, δ is the phase difference between A and B . A linearly polarized light at angle α to horizontal can be described by $\begin{pmatrix} \cos\alpha \\ \sin\alpha \end{pmatrix}$ where $\delta = 0$. A

horizontally polarized light has $\alpha = 0$ and $\vec{E} = \begin{pmatrix} 1 \\ 0 \end{pmatrix}$ and vertically polarized light has

$\alpha = \pi/2$ and $\vec{E} = \begin{pmatrix} 0 \\ 1 \end{pmatrix}$. Similarly for a circularly polarized light, A and B have equal magnitude along with $\delta = \pm\pi/4$, defining left circular polarization by $\delta = +\pi/2$ or

right circular polarization by $\delta = -\pi/2$ and can be represented as $\frac{1}{\sqrt{2}} \begin{pmatrix} 1 \\ \pm i \end{pmatrix}$. However, visualization of elliptical states of polarization in terms of linear basis is challenging. Considering a Poincare sphere approach paves way for simpler analysis where every point on the sphere represents a pure state of polarization [85].

The output polarization orientation to be measured can be defined as $\vec{E} = \begin{pmatrix} A \\ B e^{i\delta} \end{pmatrix}$. A linear polarizer is placed at the output of the fiber to record the power detected on the photodiode as a function of the transmission axis polarizer with respect to output beam. If θ is the angle with polarizer transmission axis with the horizontal axis, then Jones matrix of the polarizer is given by $\begin{pmatrix} \cos^2\theta & \sin\theta\cos\theta \\ \sin\theta\cos\theta & \sin^2\theta \end{pmatrix}$. The power measured by the photodiode for a fixed position of the polarizer angle θ can be written mathematically as

$$I = \kappa(A^2\cos^2\theta + B^2\sin^2\theta + AB\cos\delta\sin 2\theta) \quad (5.1)$$

where κ is proportionality constant and is ignored in the fit for the data. Output polarizer is rotated to cover 360° and corresponding power measured in the photodiode is recorded. The data is mathematically fit using Eq. 5.1 to obtain the linear basis parameters A , B and δ . These parameters are transformed into circular basis set and the output ellipticity (ε_{out}) is given by

$$\varepsilon_{\text{out}} = \tan(\pi/4 - \chi) \quad (5.2)$$

where $\chi = \cos^{-1} \sqrt{\frac{1 + \sin 2\alpha \sin \delta}{2}}$ is the half of the polar angle in a Poincare sphere and $\alpha = \cos^{-1} A$ [86].

5.3 Properties of polygon shaped core ARHCFs

The polarization evolution study includes three different ARHCF core geometries viz; square, hexagon and nonagon core. Inset of Figure 5.3 shows the fiber cross sections and corresponding propagation loss profile. These three different fibers are chosen as they transmit at Ti:Sapphire wavelength of 800 nm and possess different polygon core geometries. Further, the square and hexagon-core fibers have similar strand thickness

and have transmission bands in VIS-NIR region between 600 to 900 nm. The fiber properties are summarized in Table 5.1.

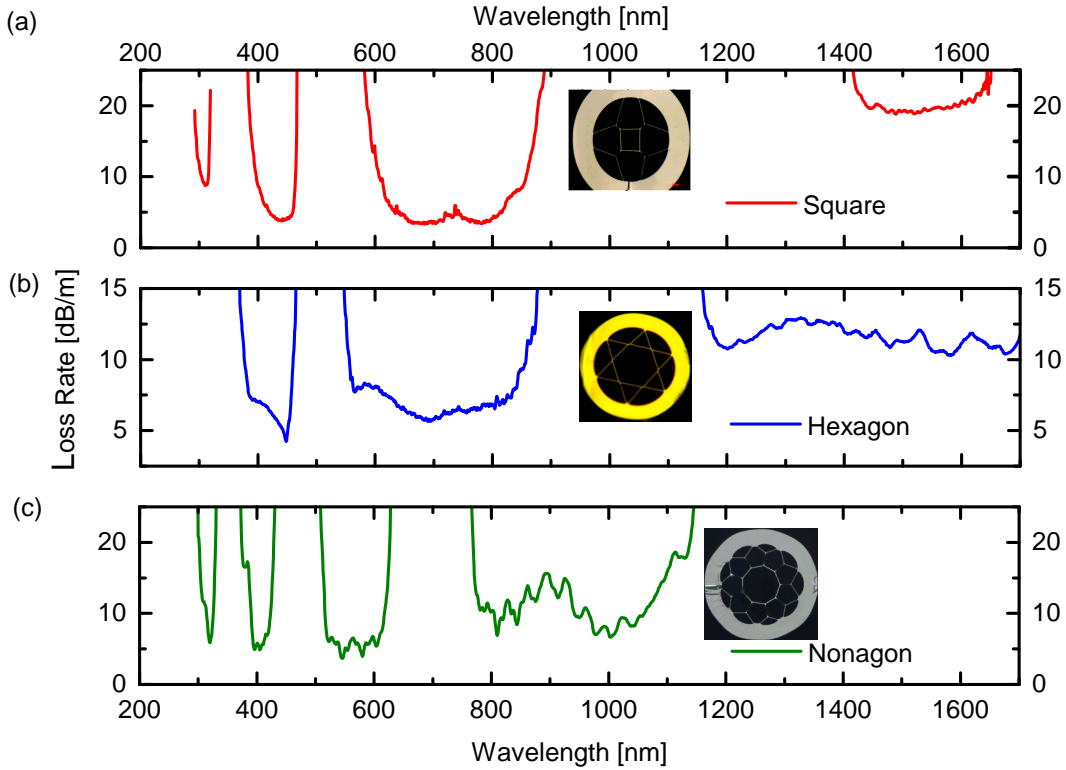


Figure 5.2: Measured spectral distribution of the modal loss of the three different ARHCFs (a) square, (b) hexagon and (c) nonagon core fibers. The transverse cross-section of the fibers is shown in the inset. Silica is shown in bright and air is represented by the darker areas.

Core geometry	Core diameter (μm)	Strand thickness (nm)
Square	~ 20 (length of a side)	~ 450
Hexagon	~ 50	~ 460
Nonagon	~ 45	~ 550

Table 5.1: Details of the fibers used in the polarization evolution experiment.

5.4 Experimental set up

The experimental set up is shown in Figure 5.3. About 11 to 12 cm long unbent ARHCF is placed on 3-axis fiber stage (*Thorlabs Nanomax*) and light from a suitable light source passes through an interference filter (IF) to select a narrow linewidth, followed by a Glan-Thompson (GTP) calcite polarizer to obtain linearly polarized output having

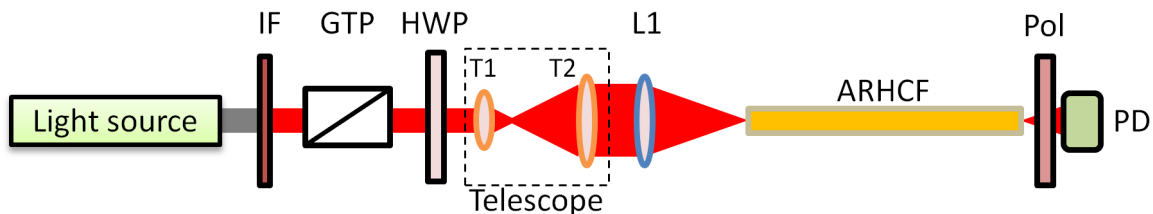


Figure 5.3: Sketch of the experimental setup used to characterize the ellipticity of the modes propagating through the fibers (details can be found in the main text)

high extinction ratio. The light passes through a half wave plate (HWP) to control the orientation of the input polarization and is coupled into the fiber using coupling optics. The lenses have low numerical aperture to avoid influencing the defined Jones matrices of the input. A polarizer is placed at the output end of the ARHCF and output light is collected on the photodiode (PD).

In the experiment, output ellipticity of the light is measured for different orientation of the HWP covering 360° . This maps the polarization evolution in the chosen ARHCF for a given wavelength. Next section discusses the impact of core geometry and impact of resonance on the output ellipticity.

5.5 Impact of core geometry on output ellipticity

For a symmetric core geometry, there is no birefringence that is imposed by the waveguide geometry [87]. The impact of deviations in core geometry from an ideal shape introduces birefringence [76, 83, 84]. For decreasing core diameter, the real and imaginary parts of effective refractive index decrease and increase, respectively [88]. Deviations from the ideal geometry influences the polarization evolution as a function of orientation of input polarization. All three fibers transmit light at wavelength of 800 nm and a commercial Ti:Sapphire system is used as input source as shown in Figure 5.4. There is no interference filter required as the input light has narrow spectral bandwidth of 15 nm.

The distance from the center of core to the core wall varies for different sides of the polygon due to technological limitations in maintaining the uniformity of the fiber drawing process. These minor deformations induce birefringence. The variation in ϵ_{out} with azimuthal periodicity for different cores geometries is shown in Figure 5.5. It can be observed that ϵ_{out} significantly varies from minimum–maximum–minimum (min–max

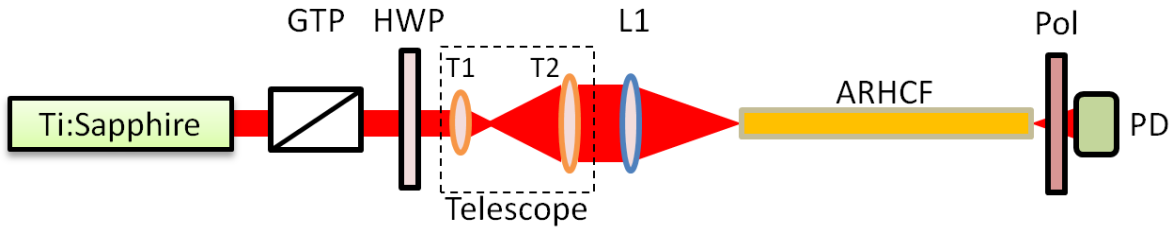


Figure 5.4: Experimental setup for absolute ellipticity measurement with orientation of input polarization at 800 nm (same set up as shown in Figure 5.3 with input being Ti:Sapphire laser system and no interference filter).

cycle) along with orientation of input polarization. The min–max cycle for square and hexagon fibers are measured to be 94° and 70° , respectively. The measurement closely correspond to inner angle of the regular polygon i.e. 90° for square fiber and 60° for hexagon fiber. Qualitatively, each min–max cycle resembles the core symmetry. Nonagon core fiber has very small variation in ε_{out} due to capillary-like behaviour of the core geometry. The effect of imperfections in the core geometry on ε_{out} decrease with increase in number of core sides.

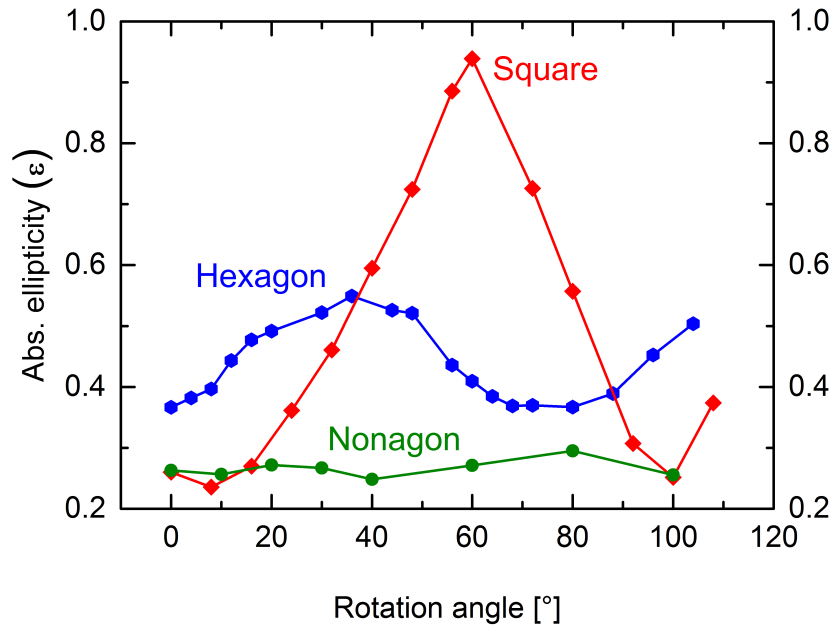


Figure 5.5: Absolute value of ellipticity as function the angle of the input polarization for different fiber core geometries (red: square; blue: hexagon; green: nonagon). Note, the orientation of the fiber has an arbitrary offset.

It is important to note that comparison of evolution of ε_{out} is qualitative in nature as all the fibers have different core diameter and also different imperfections. However, these measurements convey that it is important to consider orientation of input polarization with fiber cross section and corresponding ε_{out} to suit any given application, especially the square core fiber which shows large variation in ε_{out} between 0.2 and 0.95.

5.6 Impact of input wavelength on output ellipticity

The ARHCFs support broadband operation range extending from UV to IR wavelengths as shown in Figure 5.2 along with high attenuation resonance regions in between. At resonance wavelengths, transverse energy dissipates into the cladding which also influence polarization property of the propagating light at that wavelength. This section discusses the impact of propagating wavelength on ε_{out} . Figure 5.6 shows the experimental set up where a supercontinuum laser (*NKT* - SuperK Compact Supercontinuum laser) is used as source along with different narrowband IFs to select narrow linewidth laser as input. IFs at wavelengths 575 nm, 625 nm, 775 nm, 825 nm, 850 nm and 875 nm are used as they cover the spectral regions in VIS-NIR region between the two resonance orders ($m=1$ and 2) of the square and hexagon core fibers. Nonagon fiber is not included in this study due to presence of lossy resonance region in the VIS-NIR region of interest.

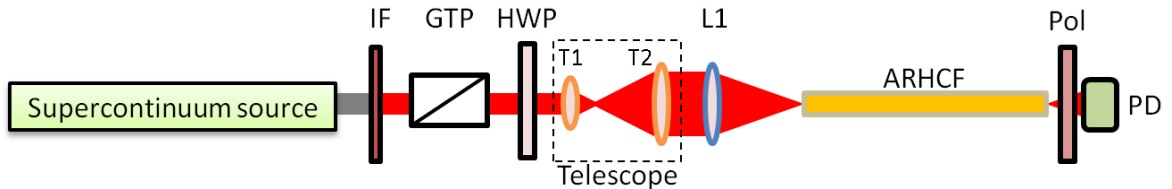


Figure 5.6: Experimental set up for absolute ellipticity measurement as a function of wavelength. Supercontinuum source is used as light source along with combination of different interference filters

Ellipticity evolution as a function of wavelength is shown in Figure 5.7 along with the excited fundamental mode. The measurement points are shown in square, circular and triangular patterns correspond to maximum, minimum and average ε_{out} , respectively. The ε_{out} is measured for every 8° of input polarization rotation and averaged to obtain average ε_{out} (shown in black).

Figure 5.7 shows a variation in ε_{out} as a function of input wavelength. Minimum ε_{out} is observed at wavelength of lowest losses i.e. at 625 nm in both the fibers. A

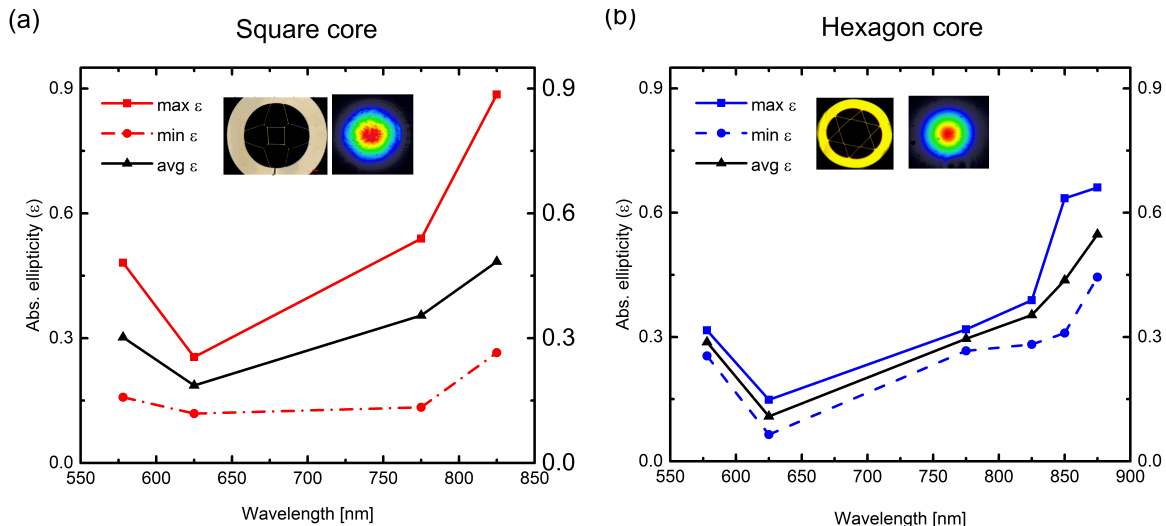


Figure 5.7: Variation of ε_{out} with input wavelength (a) for square core (in red); (b) and hexagon core fibers (in blue). For a chosen wavelength, ε_{out} is measured as explained in section 5.5. Maximum and minimum ε_{out} are shown in continuous and dotted lines, respectively. Average ε_{out} is averaged value for every 8° rotation of input polarization and is shown in black.

significant increase in ε_{out} is observed towards the resonance wavelengths in both square and hexagon fibers. This suggests a direct correlation between ε_{out} and the modal losses due to resonance. In square fiber ε_{out} varies from 0.12 at 625 nm to 0.9 at 825 nm and in hexagon fiber ε_{out} varies from 0.06 at 625 nm to 0.6 at 875 nm. The results show the importance of choosing right operating wavelength to obtain minimum ε_{out} at the fiber output for a given application.

5.7 Discussion

The impact of structural deviations during the fiber drawing introduces birefringence in the ARHCF. Different fiber designs like nested antiresonant nodeless fiber [83] and ARHCFs with different strand thickness surrounding the core [84] have been proposed for negative curvature ARHCFs, where it is challenging to introduce significant birefringence. However, single-ring (polygon-shaped core) ARHCFs, under discussion here, can introduce significant birefringence by deviating away from ideal polygon shaped core design. This can be understood by considering a leaky square waveguide that contains negligible fraction of power in the corners (see Figure 5.8a). This slab waveguide model qualitatively simulates the impact of structural deviations on modal

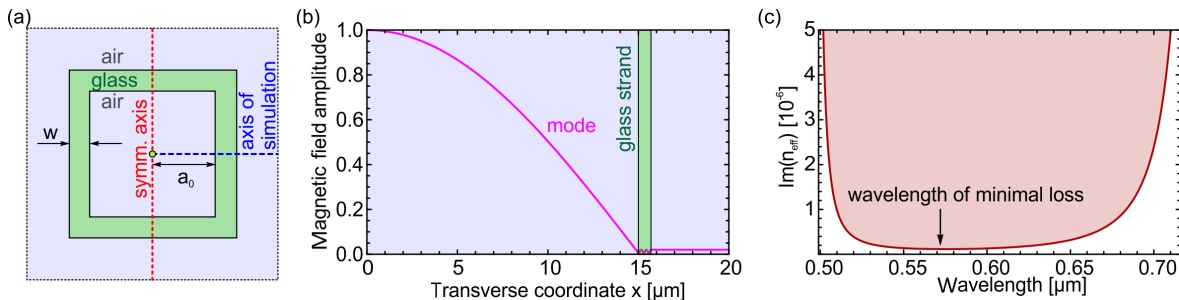


Figure 5.8: (a) Sketch of the slab waveguide model: light green shows the waveguide material silica glass (refractive index = 1.45) and light blue corresponds to air; w is the strand thickness and a_0 is the distance from the symmetry axis (red dashed line) to the glass strand; blue dashed line shows the axis of the simulation and refers to the spatial refractive index distribution used within in this toy model. (b) Real part of the magnetic field amplitude of the fundamental leaky mode as function of transverse coordinate (represented by the blue dashed line in (a)). (c) Imaginary part of the effective index of the fundamental leaky mode in the wavelength domain between the second ($m = 2$) and the third ($m = 3$) order resonances [88].

properties (light blue: air, light green: silica). The blue dashed line denotes the axis of simulation and the vertical red line show the symmetry axis of the square core waveguide geometry. An ideal square core provides zero birefringence regardless of relative orientation of incident polarization vector and the core symmetry axis. But, when the square core is deformed along one of its main axes (blue dashed line), the degenerated propagating constants of the fundamental modes split. This leads to modal birefringence [88]. Figure 5.8b shows the real part of the magnetic field amplitude along the axis of simulation (transverse coordinate) calculated by the slab waveguide toy model (TM-polarization) for the fundamental leaky mode [88–90]. Figure 5.8c shows the imaginary part of the effective refractive index between the second ($m = 2$) and the third ($m = 3$) order resonances. Effect of structural deviations on the refractive index and propagating wavelength are carried out at wavelength of minimal loss (black arrow in Figure 5.8c).

The impact of structural deviations from an ideal core shape on birefringence is simulated between two waveguides having core radii a_0 and a . These qualitative simulation results show an increase in the relative effective index (Δn), both in real and imaginary parts, with an increase in relative core radius ($a - a_0$). The results also suggest that birefringence in ARHCFs depends on the actual size of the core. This needs to be taken into consideration when comparing the polarization properties of different types (square, hexagon, and nonagon) of hollow core fibers studied in this work.

The structural deviations from an ideal core shape has an impact on spectral char-

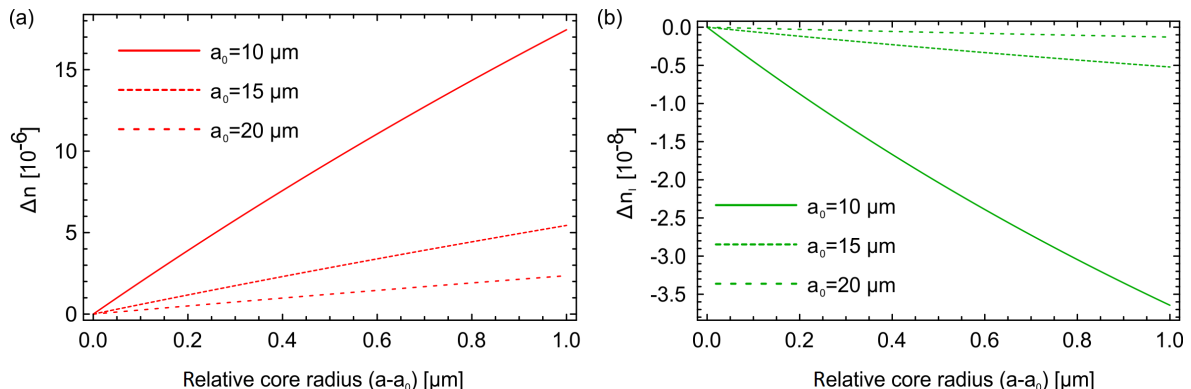


Figure 5.9: Effect of relative core radius on birefringence at wavelength of minimal loss ($\lambda = 572$ nm as indicated by the arrow in Figure 5.8c). (a) Real and (b) imaginary parts of the relative effective index ($n_{\text{eff}}(a_0) - n_{\text{eff}}(a)$) as function of the relative core radius ($a - a_0$), calculated using the slab waveguide toy model for strand thickness of $w = 0.7 \mu\text{m}$). The three different lines in each plot refer to three different base core radii varying from $10 \mu\text{m}$ to $20 \mu\text{m}$ (as indicated in the respective legend) [88].

acteristics of the leaky waveguide. This is studied by taking the difference between two simulations of the spectral distribution of n_{eff} for a base radius of a_0 and a slightly increased base radius $a_0 + \Delta a$, where $\Delta a = 100$ nm. The results shown in Figure 5.10 correspond to the spectral transmission window between the second ($m = 2$) and the third ($m = 3$) strand resonances. The spectral distribution of variation in effective refractive index (Δn) qualitatively follows the spectral dependence of $\text{Re}(n_{\text{eff}})$ where highest birefringence is observed close to the short wavelength side of the lower-order resonance, i.e. Δn is maximum at around 720 nm ($m=2$) when compared with 510 nm ($m=3$). The impact of the structural deviations reduce for an increasing core radius as suggested by the three curves in Figure 5.10a when compared with the scenario shown in Figure 5.9a. The corresponding imaginary part (Figure 5.10b) shows significant effect of structural deviations close to the edges of the transmission band. This can be attributed to the increase of electromagnetic field inside the glass strand in close proximity to the strand resonances. Hence, a strong polarization dependence is visible near edges of the transmission window.

This simulated toy-model gives only qualitative insights into the underlying principles of structural deviations in the ideal polygon core of an ARHCF. This model is a one dimensional hypothetical model. A direct quantitative comparison to the presented experimental results is unfeasible as the ARHCF structures experimentally investigated have two dimensional cross sections.

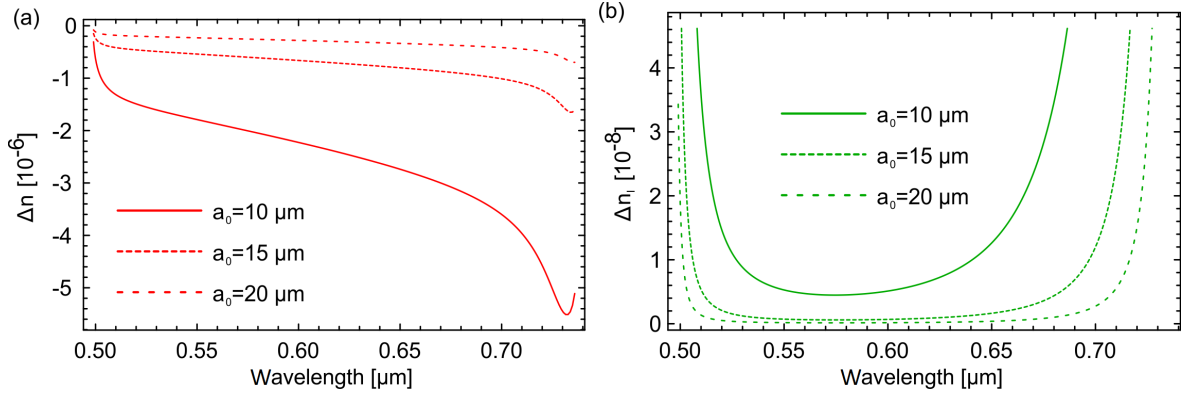


Figure 5.10: (a) Sketch of the slab waveguide model: light green shows the waveguide material silica glass and light blue corresponds to air; w is the strand thickness and a_0 is the distance from the symmetry axis (red dashed line) to the glass strand; blue dashed line shows the axis of the simulation and refers to the spatial refractive index distribution used within in this toy model. (b) Real part of the magnetic field amplitude of the fundamental leaky mode as function of transverse coordinate (represented by the blue dashed line in (a)). (c) Imaginary part of the effective index of the fundamental leaky mode in the wavelength domain between the second ($m=2$) and the third ($m=3$) order resonances [88].

Impact of fiber geometry and wavelength on ε_{out} from the experiments is summarized in Figure 5.11. The contour plot for square and hexagon fiber shows the variation of ε_{out} with respect to orientation of polarization at the input along horizontal axis and with respect to wavelength along vertical axis. Fundamental mode guidance is observed in both fibers at all the scan wavelengths. ε_{out} value are color coded as shown

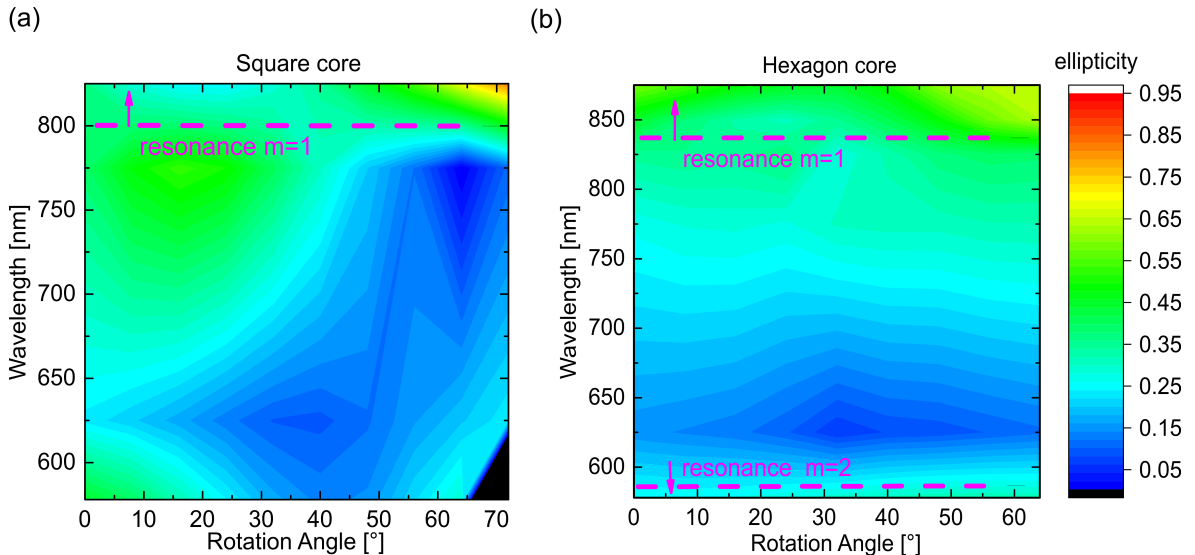


Figure 5.11: Contour plots for variation of ε_{out} with polarization of the incident beam and wavelength (a) square core and (b) hexagon core. Pink dashed horizontal lines represent the beginning of resonance region and the arrow points the direction of increasing resonance. The color bar on the right indicates the measured ε_{out} values. (The black portion shows no measurement).

by the vertical bar on the right side of the figure. The plots show a steep gradient in color along wavelength axis towards the resonance region. These maps illustrate the overall variation of ε_{out} in a non ideal polygon core of an ARHCF. The best operating wavelength to obtain output light with minimal output ellipticity is the point having the deep blue color.

5.8 Summary

This chapter explored the dependence of the geometry-induced polarization behaviour in polygon core ARHCF on various parameters from the experimental perspective. The structural deviations from an ideal polygonal core geometry provide a platform to induce birefringence in ARHCF which otherwise not possible in NC-ARHCF while maintaining the structural symmetry. Orientation of input polarization angle is critical as it has strong influence on the azimuthal deviations of the core geometry and can introduce large variation in ε_{out} . It is also observed that modal attenuation depends on the input polarization state and ε_{out} increases towards resonance region. Center of the transmission bands showed minimal variation in ε_{out} and maintain the minimum ε_{out} . One dimensional simulations support the observed experimental results qualitatively.

Part III: Non-linear properties of ARHCF

6 Supercontinuum Generation in ARHCF

Supercontinuum generation is a phenomena where a narrow band light undergoes extreme broadening in spectrum due to nonlinear interaction between the propagating light and the material [39]. It was shown that interplay between nonlinear effects and dispersion of the optical fibers can support soliton-like pulses [91] and were experimentally observed in 1980 leading to generation and control of ultrashort optical pulses [92, 93].

The first demonstration of supercontinuum generation in optical fiber was by *Lin and Stolen* in 1976 [94]. The field started to flourish after the advent of photonic crystal fibers (PCF) in the late 1990s because one can tune the dispersion properties in the core of the fiber not only by changing the core diameter, but also by varying holey cladding parameters such as pitch and diameter of cladding holes during the fiber design [8, 95–97]. The solid core fibers have limitations in terms of achievable peak power due to low damage threshold of silica and no flexibility in the control over the net dispersion characteristics for a given fiber design and length. Conventional hollow core capillary waveguide supports high peak power operation and also choice of nonlinear medium (e.g. capillary can be filled with inert gases, Raman-active gases, etc.), but losses increase inversely to the cube of capillary diameter, which is crucial to increase the nonlinearity, limiting its performance [16].

Invention of hollow core PCF and Kagome fibers have revolutionised the field of nonlinear fiber optics by combining the advantages of PCF technology and capillary waveguides [62, 98] such as tuneable fiber dispersion properties, high damage threshold operation, choice of nonlinear media that can be filled in the hollow core. Further, these new hollow core PCFs provide low loss transmission for a broader spectral bandwidth when compared with capillary waveguides. However, highly complex cladding structure of the Kagome introduces many challenges during the fiber drawing process.

The ARHCFs possess unique fiber properties such as broadband transmission window from ultraviolet to mid infrared, fundamental mode propagation throughout transmission window, high damage threshold. These fibers have found widespread applications in various fields of nonlinear optics [99], sensing [53, 100], telecommunication [78], and high-power delivery [51]. This chapter explores on efficient supercontinuum generation in ARHCF where an additional degree of freedom in dispersion management can be achieved due to resonance. Such a dispersion profile plays a crucial role in enabling new regime of soliton dynamics leading to spectral superbroadening.

A comparison of dispersion profile between ARHCF under study and Kagome-type or capillary type fiber is made in section 6.1. The experimental setup to generate supercontinuum in gas-filled ARHCF is described in section 6.2. Supercontinuum generation results in homogeneously gas-filled and differentially pumped ARHCF are shown in section 6.3. Section 6.4 introduces the simulation model and section 6.5 discusses different nonlinear effects that play a role in supercontinuum generation in the novel dispersion tuned ARHCF based on UPPE and GNLSE model. Supercontinuum generation in Raman active N₂ gas filled ARHCF is explained in section 6.6 and the results are compared in the final section 6.7.

6.1 Comparison of dispersion between ARHCF and Capillary

As we observed in chapter 4, the dispersion profile of the ARHCF varies abruptly near the resonance wavelength by few orders in magnitude. Figure 6.1 shows the comparison between calculated GVD profile of an hexagon core ARHCF and conventional hollow core fiber having same core diameter (when homogeneously filled with 6 bar of krypton gas). The GVD profile of the ARHCF is calculated by finite element method in the *COMSOL* software [82]. The resonance wavelength is considered the center of resonance spectrum (see Figure 3.5), i.e. at 1 μm . Along with abrupt variations in GVD profile near resonance region, ARHCF has four zero dispersion wavelengths (ZDW) in a bandwidth of 400 nm against one ZDW in HCF. These additional ZDWs further assist in accelerating nonlinear soliton dynamics which lead to supercontinuum generation.

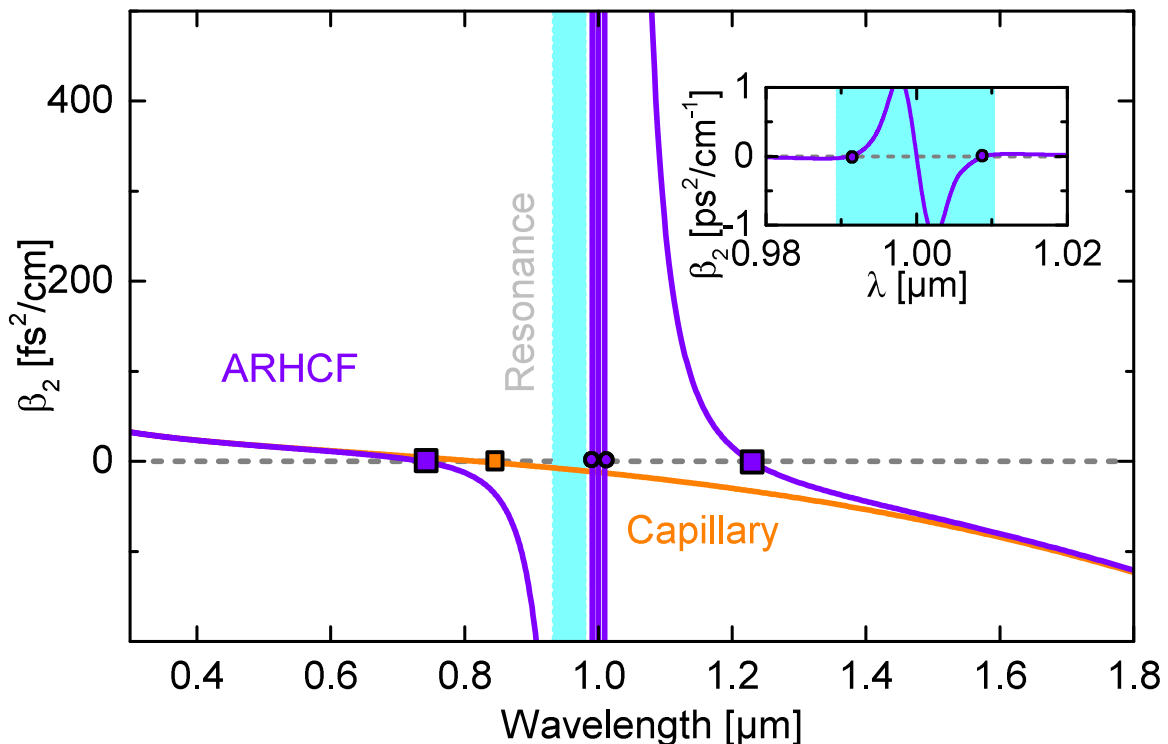


Figure 6.1: Comparison of group velocity dispersion between ARHCF and HCF: COMSOL simulation of the group velocity dispersion of the fundamental mode in the ARHCF filled with krypton at a pressure of 6 bar (purple curve, strand resonance located at 1 μm (in blue); orange line corresponds to gas-filled HCF dispersion having no strand resonance). The rectangle mark shows the zero group-velocity dispersion wavelengths. The inset shows close-up view of the GVD in the strand resonance. The circular mark shows the ZDW in the lossy resonance spectral region.

6.2 Experimental set-up

The experiment was carried out using a femtosecond Ti:Sapphire Chirped Pulse Amplifier (CPA) laser system. The CPA system delivered 80 fs pulses with energies up to 1 mJ at central wavelength of 800 nm with repetition rate of 1 kHz (*SpectraPhysics Spitfire*). The experimental setup is shown in Figure 6.2. Linearly polarized pulses emitted by the laser pass through a combination of a broadband (ultrafast) Thin-Film Polarizer (TFP: *Altechna 2-UFP-0800-2060-T2*) and a HWP (*Thorlabs Achromatic HWP: AHWP10M-980*) to control the input pulse energy from few nJ to 50 μJ . The collimated input beam having diameter of 12 mm was coupled into the core of the ARHCF (core diameter: 50 μm , length: 250 mm, shown in Figure 3.4) using a lens having focal length of 200 mm. The spot size at the focal point was measured to be 17 μm by knife edge technique. Unlike, HCF where the ratio between spot size and core diameter for best in coupling ~ 0.67 [16], the experiments with ARHCF show better coupling efficiency for

the ratio of $\lesssim 0.5$. A throughput efficiency of 65% was recorded for the evacuated fiber and remained constant for entire range of gas pressures and input energies used in the experiments. Both ends of the fiber were mounted on two independent gas cells with the possibility to maintain either a constant gas pressure along the fiber or a pressure gradient during experiments.

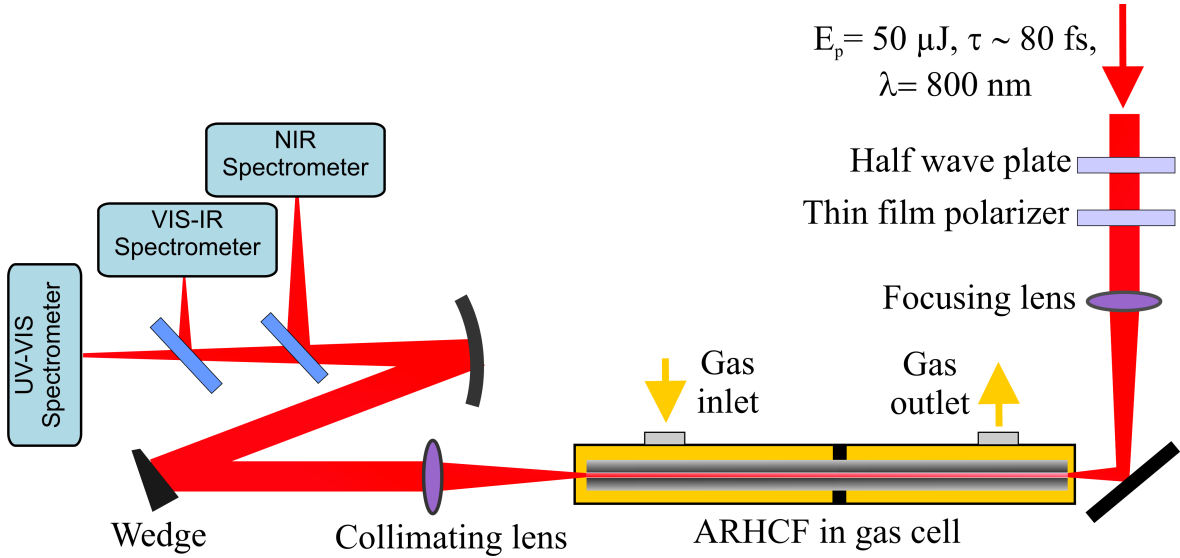


Figure 6.2: Schematic of the supercontinuum generation experimental setup. The yellow arrows refer to the situation of differential pumping to create a pressure gradient inside the fiber sample.

The output yield was attenuated by reflection on a wedge. This avoids saturation of spectrometer pixels at high output energies. The output beam is focused on the entrance slits of three different spectrometers via flip mounts. Two *Ocean Optics* silicon CCD spectrometers (USB4000-UV-VIS measures from 200 nm to 893 nm and USB2000+ measures from 504 nm to 1171 nm) are characterized to record the output from ultraviolet to near infrared (NIR) spectral range. An InGaAs CCD spectrometer (*Ocean Optics* NIRQuest512: measures from 899 nm to 1706 nm) for the NIR to short-wavelength infrared (SWIR) spectral range. Together with these combination allowed the characterization between 200 nm and 1.7 μm . In a control experiment with an entirely empty fiber i.e., fiber system including gas chambers are in vacuum, no signal is recorded in UV-VIS region for output energies up to 20 μJ and a clear signal at 800 nm suggests no stray light influence or nonlinearities in the waveguide material silica has to be taken into account for the experimental configuration discussed here. A clear UV signal appears above a particular threshold energy as shown in Figures 6.3 and 6.5. It is important to consider that the UV signal shows a dependence on gas

pressure (i.e., the *Ocean Optics* spectrometer showed a change of UV intensity which correlates with a change in gas pressure), clearly indicating that we can detect such short wavelength and that they originate from supercontinuum generation, which is additionally confirmed by the mode images (Figure 6.4).

It is important to consider that at resonance the strands resemble a Fabry-Perot type resonator operating in transmission mode, which imposes that the strands do not act as individual waveguides, i.e., do not support guided waveguide modes. The energy continuously leaks through the strands, but not propagate at these wavelengths. No intense light emerging from the strands is observed in the experiment. The contribution of the strand with regard to light generation is negligible in the experiments carried out here.

6.3 Supercontinuum generation

Homogeneously gas filled ARHCF

The evacuated ARHCF is homogeneously filled with krypton gas at 6 bar. The evolution of spectral broadening of the 80 fs laser pulses at an 800 nm wavelength as a function of increasing output pulse energy is shown in Figure 6.3(a-e). The Figure 6.3e shows the output spectrum at 60 nJ which is same as the input spectrum with no nonlinear interactions due to low pulse energy. Gradual increase of the input energy shows spectral broadening due to SPM. The broadening approaches towards spectral resonance region at output energy of 5 μJ as shown in Figure 6.3d.

A sudden onset of extreme spectral broadening at $\sim 6.5 \mu\text{J}$ of output energy is distinctly visible in Figure 6.3c. This broadening evolves into a multi-octave-spanning supercontinuum at an output energy of $\sim 8.1 \mu\text{J}$. This broadening towards longer wavelength region surpasses the lossy resonance spectral region (Figure 6.3b). Further, an increase in spectral content in the NIR region is observed where the output spectrum extends from 200 nm in ultraviolet to 1.4 μm in the NIR spectrum at $\sim 12.1 \mu\text{J}$ (see Figure 6.3a).

It is notable that a few-hundred nanometer spectral broadening is recorded with only a 25% increase in the output energy (Figure 6.3c-d). The broadening spans from UV (200 nm) region to the starting point of resonance at the output energy of

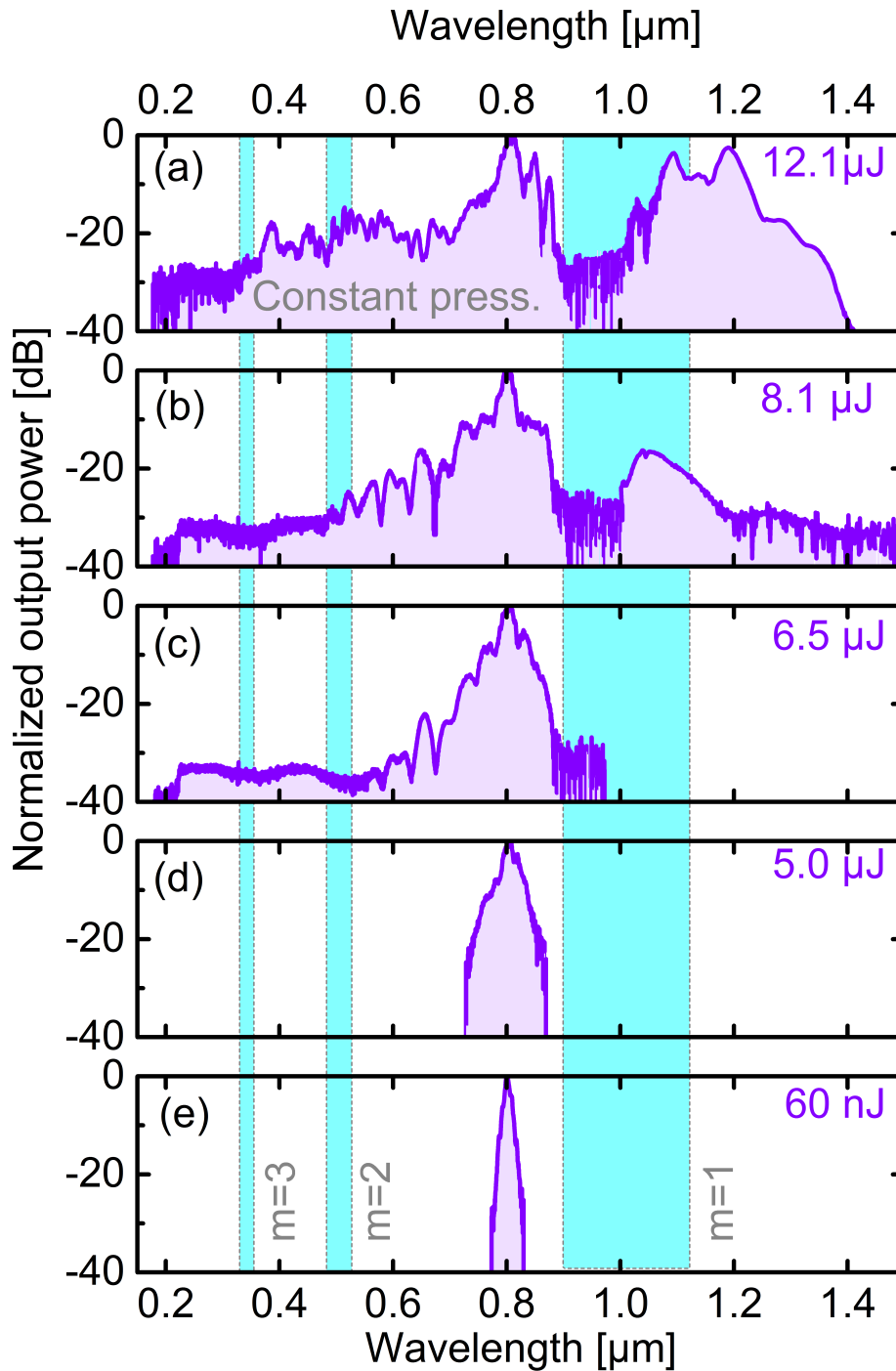


Figure 6.3: Measured spectral content at various output pulse energies in homogeneously krypton-filled ARHCF at 6 bar (given in the plots(a)-(e)). The corresponding output energy values are shown on the top right side of the plots. The blue bands show the resonance region for resonance orders $m=1,2$, and 3 . (e) has identical spectrum as the input laser spectrum, (d) shows the spectral broadening due to SPM, (c) shows the effect of resonance region on spectral broadening by onset of multiple dispersive waves and (b) shows extension of broadening on the longer wavelength of resonance. (a) shows increased spectral content in infrared spectral region at output energy of $12.1 \mu\text{J}$.

$\sim 6.5 \mu\text{J}$, where the signal in the NIR region is below the noise limit of the spectrometer. The spectral broadening further extends towards the IR spectral region with only 20% increase in the input energy. This is shown in Figure 6.3b-c with an increased supercontinuum power spectral density in IR region. At constant krypton gas pressure of 6 bar, the maximum achieved output energy in ARHCF for nearly three octaves broadband supercontinuum is $\sim 12.1 \mu\text{J}$ with $\sim 19 \mu\text{J}$ of input energy. Further increase in input energy resulted in significant ionization of the gas at the fiber input. This limits the fiber performance due to drilling of $\sim 495 \text{ nm}$ thick strands which support the antiresonant mode guidance through the fiber.

The near-field beam profile of the fiber output is measured in atmospheric conditions without gas cells shown in Figure 6.4a. It shows that majority of the propagating energy is confined in the core of the fiber.

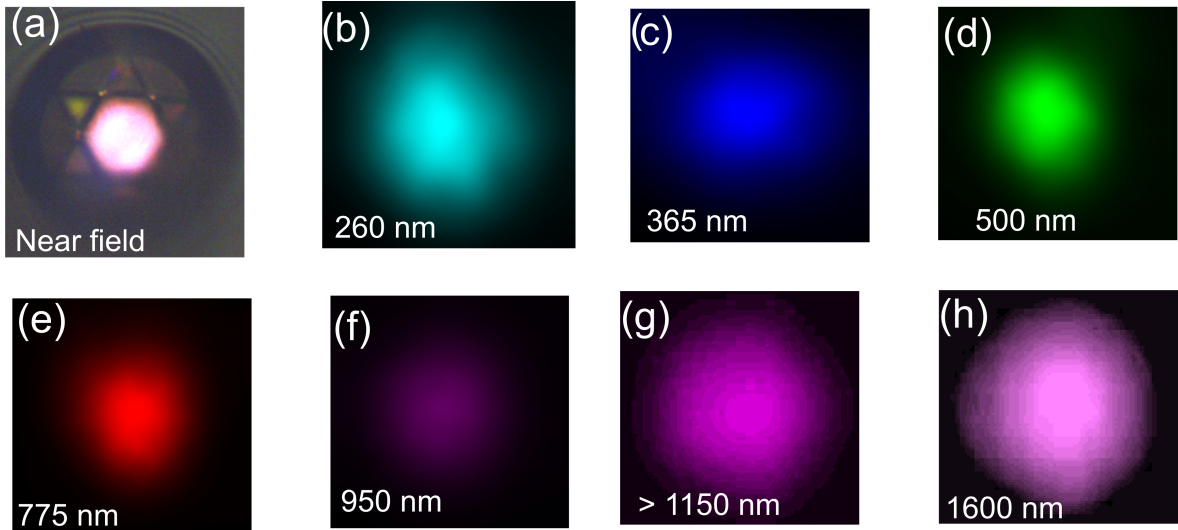


Figure 6.4: Recorded output mode profiles: (a) near field mode profile at the tip of the output end showing light confined in the core of ARHCF. (b-h) recorded at maximum output energy of $12.1 \mu\text{J}$ (see Figure 6.3a) behind narrowband filters with central wavelengths (b) 260 nm, (c) 365 nm, (d) 500 nm, (e) 775 nm, (f) 950 nm, (g) $>1150 \text{ nm}$, (h) 1600 nm. (a-f) are recorded using silica detector and (g-h) using InGaAs detector.

The far-field beam profiles of the supercontinuum output were selectively measured at different wavelengths by placing corresponding narrowband filters in front of the cameras (in UV-VIS spectral region: *Coherent GmbH* LaserCam-HR with BeamView software; in NIR spectral region: *ABS GmbH*, InGaAs IK-1513) placed at a distance of $\sim 12 \text{ cm}$ from the fiber end. Figure 6.4b-f shows far-field mode patterns for maximum output energy of $\sim 12.1 \mu\text{J}$ confirming fundamental mode propagation at all wavelengths

of the supercontinuum.

The experiment was conducted under the same energy conditions in an evacuated fiber system (down to 10s of mbar) to verify the contribution of spectral broadening from glass strands. The output spectral distribution was essentially identical to the input spectrum and confirm no contribution from waveguide material in spectral broadening.

Differentially-pumped ARHCF

The gas ionization effect at the fiber input is overcome by the differential gas pumping configuration. Here, the input of the fiber is maintained under vacuum conditions (10s of mbar) by a roughing pump and output gas cell is maintained at high krypton gas pressure of 6 bar. This gradient gas pressure not only avoids dense gas plasma formation at the fiber input, but also facilitates to couple higher input energies into the fiber. Tight focusing of the input beam avoids any direct damage of the fiber strands at the input and enables long term operation. This configuration observes no degradation in the output beam quality for hour long operations. The evolution of spectral broadening in this configuration is similar to homogeneously gas-filled system where onset of sudden broadening is first observed on the short wavelength side of the pump wavelength. The broadening extends towards longer wavelength region at higher input energies surpassing the lossy resonance valley as shown in Figure 6.5. SPM dominates spectral broadening up to 10 μJ of output energy (see Figure 6.5c) where broadening approaches resonance region. At $\sim 19 \mu\text{J}$ of output energy, spectral broadening largely extends towards shorter wavelength and also starts to overcome the resonance region with signal up to wavelength of 1.3 μm . Significant broadening is observed towards longer wavelengths extending the signal content up to 1.7 μm with only 20% increase in the output energy. Maximum broadening in differential pumping scheme is achieved at roughly double the coupled energy as seen in Figure 6.5a (in comparison with Figure 6.3a), and with an extended spectral broadening towards the NIR. In the IR region, the longest wavelength measured is 1.7 μm at output pulse energy of $\sim 23 \mu\text{J}$ (Figure 6.5a) and was limited by spectrometer range.

It is important to highlight that the high modal loss associated with the strand resonances (see Figure 3.4) is considerably suppressed at highest input energies as

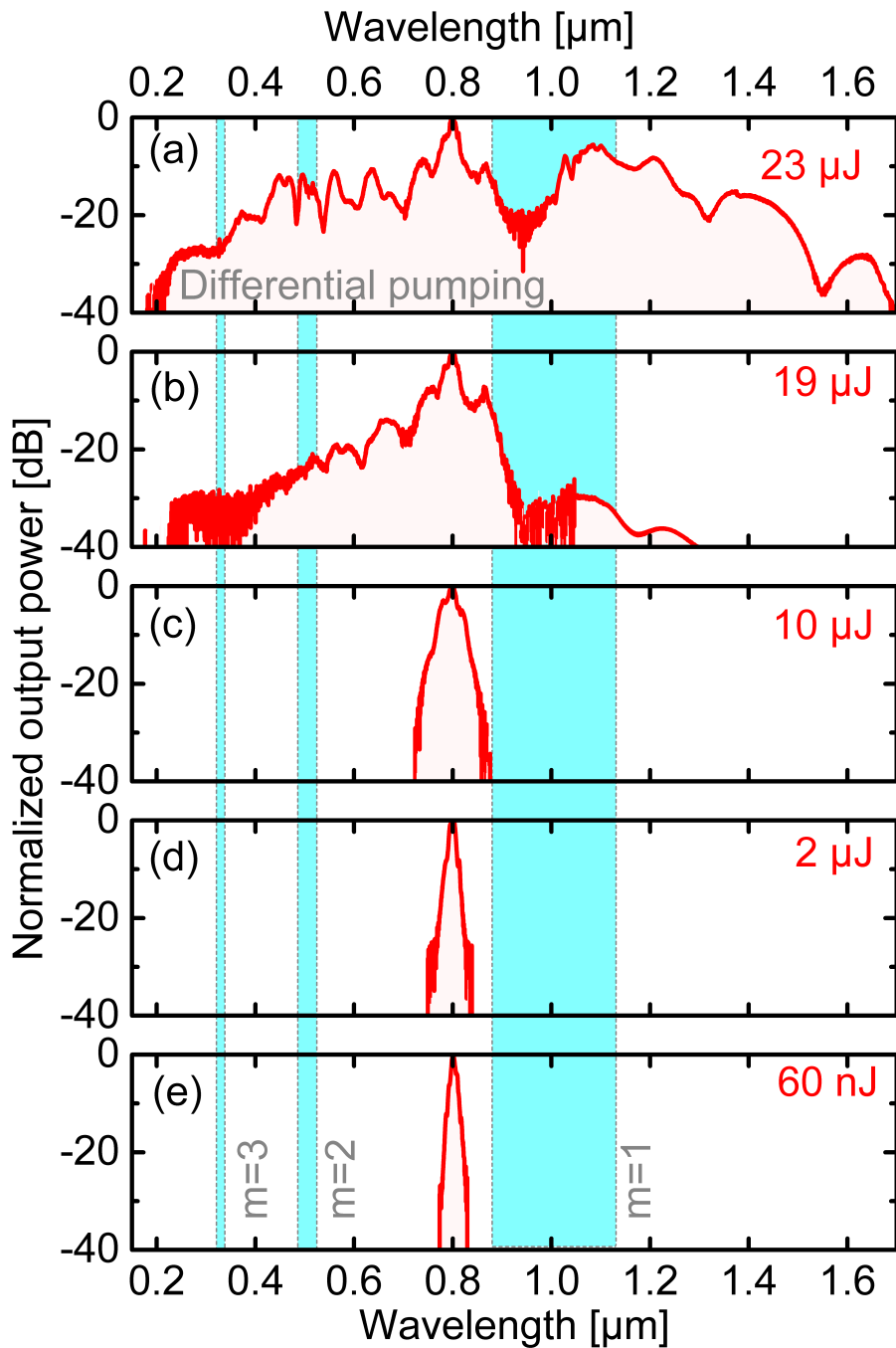


Figure 6.5: Measured spectral content at various output pulse energies in differentially pumped, krypton-filled ARHCF at 6 bar (given in the plots (a)-(e)). The corresponding output energy values are shown on the top right side of the plots. The blue bands show the resonance region for resonance orders $m=1$, 2, and 3. (e) is the input laser spectrum recorded at the exit of the fiber. (c, d) shows the spectral broadening due to SPM only for output energies of 2 μJ and 10 μJ . (b) shows the effect of resonance region on spectral broadening by onset of multiple Cherenkov radiation emission. (a) three octave spectral broadening at output energy of 23 μJ . The losses due to resonance is overcome by the nonlinear process to produce a continuous spectral output.

shown in blue bars in Figures 6.3 and 6.5. This shows that intrinsic propagation losses of the waveguide are fully compensated by nonlinear process of frequency conversion to achieve spectrally continuous output spanning over three octaves of bandwidth [101]. At maximum spectral broadening (i.e. in Figure 6.5a), nearly 75% the output energy is concentrated the infrared region (>700 nm), 24% in the visible spectral region (400-700 nm) and $\sim 1\%$ in the UV (< 400 nm). The Popov-Perelomov-Terentiev equation [102] is used to estimate the plasma density for the experimental conditions. It suggests that ionization plays an insignificant role for input energies of at least up to ~ 20 μJ . The relative plasma density increases to $\approx 2\%$ for the maximum input energy of ~ 35 μJ (corresponding to output energy of ~ 23 μJ energy in Figure 6.5a), and possibly play a role in the spectral broadening process due to nonlinear effects arising from to gas ionization (for e.g., spectral blueshift).

The final spectra shown in Figures 6.3 and 6.5 are recorded by different spectrometers and are stitched together by comparing the overlapping regions with similar spectral features to precisely record all the spectral features. Each individual spectrum was corrected for the spectral distribution of the respective spectrometer sensitivity.

6.4 Numerical Simulation and Analysis

As a consequence of the strong change of the GVD (discussed section 4.3), the ultrafast excitations located within the spectral domain adjacent to the strand resonance cannot be described anymore as classical Schrödinger solitons. The higher-order dispersion terms presumably play a significant role. The numerical simulations are carried out to model propagation of ultrafast pulses in such extreme dispersion domain with soliton-like behavior using Unidirectional Propagation Pulse Equation (UPPE) in the frequency domain (introduced in section 2.2.1 and reference [26]). These simulations happen in real electric field and hence are not limited by spectral bandwidth. The analytic representation of a real-valued electric field output can be easily calculated by considering the envelop of the high frequency carrier wave via Hilbert transform. Mathematically, UPPE is given by,

$$\frac{\partial \varepsilon}{\partial z} = i(k(\omega, p) - \frac{\omega}{\nu})\varepsilon + i\frac{\omega^2}{2c^2k(\omega, p)}\chi^{(3)}\mathcal{F}[E^3] \quad (6.1)$$

where, $\varepsilon(\omega, z) = \mathcal{F}[E(t, z)]$ is the spectral amplitude, \mathcal{F} is the Fourier transform operator, $E(t, z)$ is the real electric field in the laser pulse. The wave vector $k(\omega, p)$ is given by the dispersion relation describing the pressure dependence of refractive index of the gas as:

$$n_g(\omega, p) = \left(2 \frac{p}{p_0} \frac{n_0^2 - 1}{n_0^2 + 2} + 1\right)^{\frac{1}{2}} \left(1 - \frac{p}{p_0} \frac{n_0^2 - 1}{n_0^2 + 2}\right)^{-\frac{1}{2}} \quad (6.2)$$

where p_0 is the normal atmospheric pressure, n_0 is the refractive index of gas at atmospheric pressure calculated using the Sellmeier equation for Kr [103], ν is the velocity of a reference frame chosen for convenience of simulations, and $\chi^{(3)}$ is the instantaneous third order susceptibility and is frequency independent.

Numerical analysis assumes the pump is propagating in a single mode along the entire fiber length light at all generated wavelengths. The modes and modal effective index for the ARHCF structure used in the experiments are calculated by finite element simulations [18]. Away from the strand resonance, dispersion relation of a gas-filled HCF fits well to the modal dispersion of the fundamental mode (i.e., capillary) [16]. Nonlinear pulse propagation in Kagome fibers are simulated with similar approach where propagation vector is defined in Ref [15] and given by,

$$k(\omega) = \frac{\omega}{c} \left(n_g(\omega, p) - 2 \left(\frac{u_{11}c}{wd} \right)^2 \right) \quad (6.3)$$

where ω is the angular frequency, p is the gas pressure, n_g is the pressure-dependent refractive index of the gas (at a constant temperature), $u_{11} \approx 2.405$ is the first root of the zero-order Bessel function, d is the core diameter and c is the vacuum speed of light. Eq. 6.3 is modified to include the contributions from resonance as:

$$k(\omega) = \frac{\omega}{c} \left(n_g(\omega, p) - 2 \left(\frac{u_{11}c}{wd} \right)^2 - \frac{a(\omega - \omega_{res})}{(\omega - \omega_{res})^2 + b} \right) \quad (6.4)$$

where the coefficients a and b are obtained from fit to the effective mode index near resonance by a Lorentzian function $a = 2.05 \times 10^9 \text{ s}^{-1}$, $b = 9.4 \times 10^{25} \text{ s}^{-2}$.

The spectral distributions of the GVD for the ARHCF and a Kagome fiber (same effect as capillary) having similar core diameter shown in Figure 6.1. The UPPE simulations assume the following experimental parameters as input conditions: pulse width of 80 fs, laser pulses energy of 12 μJ having central wavelength of 800 nm propagating in the

20 cm long ARHCF having core diameter of 50 μm and filled with krypton gas at 6 bar of constant pressure. The simulation ignores propagation losses for simplicity. The fundamental strand resonance wavelength is chosen to be 1 μm , approximately corresponding to the center of the first order resonance band (see Figure 6.1).

6.5 Discussion

Figure 6.6 shows comparison of nonlinear pulse propagation simulations in the krypton filled ARHCF (Figure 6.6a) and in Kagome fiber (Figure 6.6b) of equal core diameter. The simulation results show significant influence of the strand resonance (at propagation length of 6 cm and 7 cm) on the supercontinuum process resulting in multi octave bandwidth extending from 200 nm to more than 2 μm with sudden dramatic increase in the broadening rate. For Kagome fibers, spectral broadening is mainly governed by SPM and self-steepening. This limits generated bandwidth to approximately 900 nm in 20 cm long fiber. SPM governs the spectral broadening process in both ARHCF and Kagome type fiber until the propagation length of 5 cm. However, when the broadening of the generated spectrum closes into the resonance region in ARHCF at about 6 cm of propagation, explosion-like dynamics is observed. The spectral broadening extends from 300 nm to 1.5 μm within a short propagation length of ~ 1 cm to generate over an octave of bandwidth.

The observed phenomena can be explained with the GVD profile of the ARHCF near resonance. As shown in measured GVD Figure 4.4 and simulations Figure 6.1, GVD increases by few orders of magnitude in the vicinity of the resonance. This abrupt change has three main effects will and shall be discussed further.

i. Soliton fission length

The rate of soliton fission and the total amount of solitons are proportional to

$$\sqrt{L_D} \sim \frac{1}{|\beta_2|} \quad (6.5)$$

where L_D is the dispersion length and GVD ($|\beta_2|$) is given by $\frac{\partial^2 k}{\partial \omega^2}$ [104]. Increment in GVD leads to increase in solitonic dynamics due to shortening of the propagation

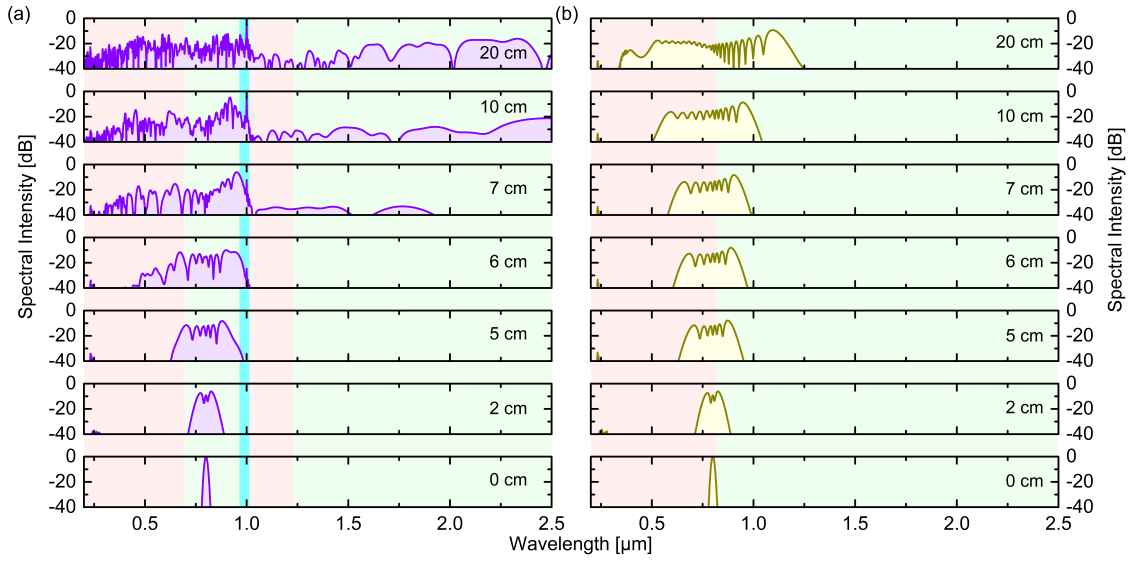


Figure 6.6: Spectral evolution in ARHCF (a) and Kagome-type (b) fibers due nonlinear pulse propagation simulations Spectral intensity distribution at different positions along the propagation length of ARHCF. Resonance region is marked in blue. Light blue shade show the anomalous dispersion region and light magenta marks the normal dispersion region.

distance. This enhances solitonic self-compression and subsequent break up into soliton-like temporally confined waves. GVD increases by orders of magnitude close to the resonance resulting in a short fission length.

ii. Cherenkov emission

Generating new frequencies using phase-matched dispersive wave generation is a well-know and particular efficient process. Typically, dispersive waves are clearly distinguishable in the spectral distribution of the generated light and allow to determine the wavelength of the associated soliton. It is challenging to identify individual dispersive waves in this experiment (and thus not associated with solitons) as the strongly changing dispersion allows phase-matching between a vast number of ultrafast excitations and dispersive waves.

Abrupt changes in magnitude of GVD implies large values of higher-order dispersion terms. These higher-order dispersion terms are responsible for formation of self-consistent large frequency shift of solitons and large number of Cherenkov emission. (The second Cherenkov radiation appears in the anomalous dispersive domain of the fiber, whereas the term "dispersive wave" normally refers to the waves generated

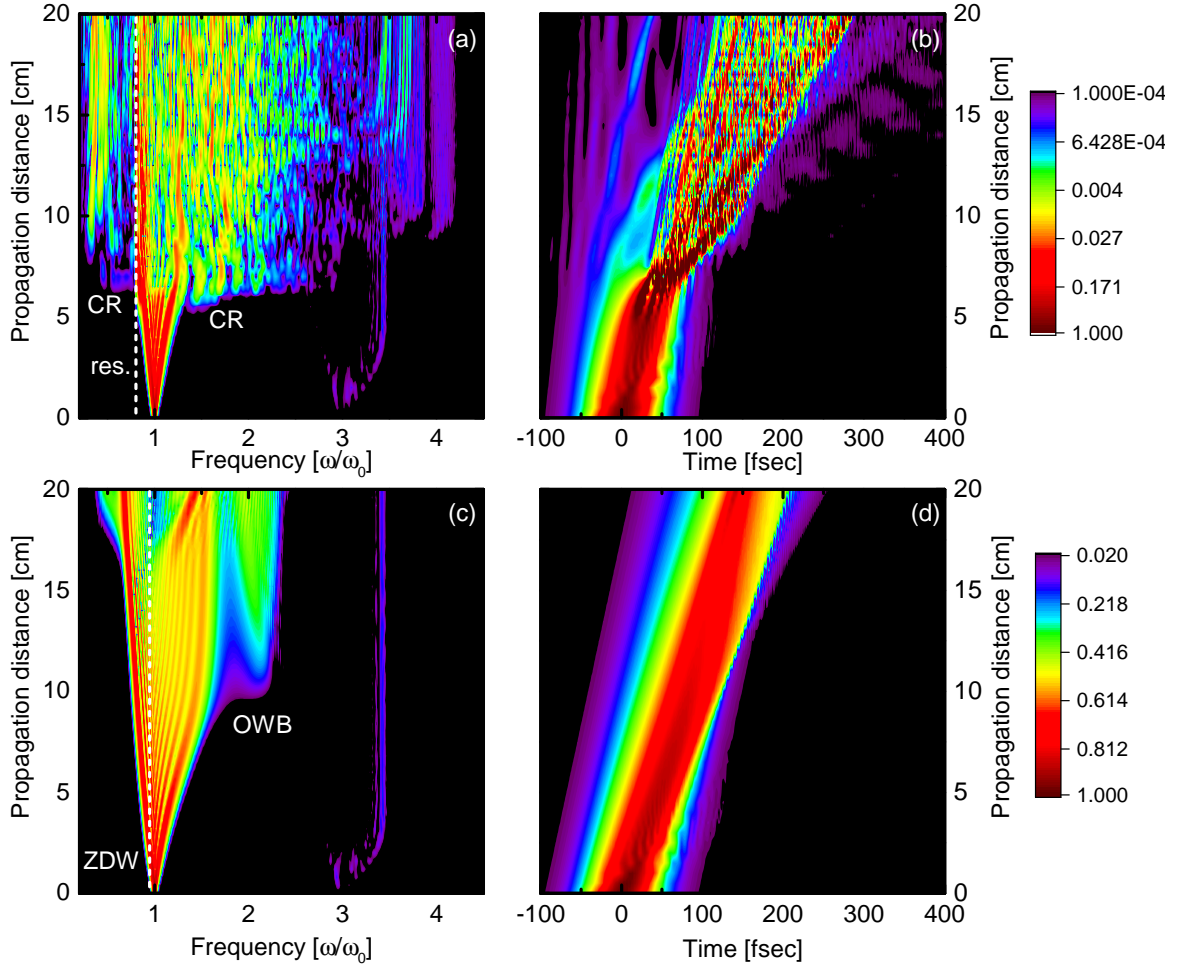


Figure 6.7: Nonlinear pulse propagation simulations in ARHCF and Kagome-type fibers. (a) Spectral intensity distribution at various positions inside the ARHCF (core diameter of 50 μm) with the dispersion profile shown in Figure 6.1. The vertical dashed line indicates the strand resonance, and the Cherenkov radiation bands are labelled by CR. The colors refer to the different intensity values defined by the top right color bar (logarithmic scale, normalized to unity). (b) Corresponding plot of the temporal evolution (bottom right color bar, linear color scale). Corresponding spectral and temporal distributions for a Kagome-type HCF with the same core diameter as the discussed ARHCF are shown in (c) and (d). The OWB label stands for optical wave breaking. The vertical dashed line in c indicates the ZDW. For all plots, ω_0 refers to the central frequency of the initial pulse ($2\pi c_0/\omega_0 = 800 \text{ nm}$) [23].

in the normal dispersion regime. Hence, more general term "Cherenkov radiation" is used throughout to avoid any confusion). The process is further fuelled by multiple ZDWs and spectral regions with opposite sign of GVD in the vicinity of the resonance (see Figure 6.1). This creates a platform for Cherenkov radiation emission at both short- and long-wavelength regions of spectrum [104].

The resonance influences the position of multiple ZDWs which in turn contributes

to the nonlinear light generation processes. Figure 6.1 compares the well-known dispersion of a capillary, corresponding to the model assumed for Kagome-type fibers, with the dispersion variations induced by a single strand resonance at $1 \mu\text{m}$ used in simulations to approximate our antiresonant fiber. It can be observed that the resonance induces four new ZDWs, out of which, two are in close proximity to the resonance. The presence of the ZDW in the near-IR on the red side of the resonance is the main reason for the energy transfer via phase-matched Cherenkov radiation generation to the longer wavelengths. Nevertheless, the first (initial) ZDW on the short wavelength side of the pump still exists and blue-shifts down to $0.75 \mu\text{m}$ due to the influence of the resonance. This ZDW is closest to the pump wavelength. Hence, energy is distributed to the short wavelength side first (i.e. the high-frequency side) and effectively leading to a drastic expansion of the spectrum to visible and ultraviolet wavelengths.

Comparison between spectral intensity distribution and temporal evolution of the simulated nonlinear pulse propagation in ARHCF and in Kagome are shown in Figure 6.7. As the main pulse undergoes the pulse break-up at the resonance, the broadening due to SPM no longer plays a role leading to soliton stabilization as seen in Figure 6.7a [105, 106]. This process releases sudden energy in the form of multiple phase-matched resonant Cherenkov radiation starting at a propagation distance of $\sim 7 \text{ cm}$ (see Figure 6.6). A subsequent Cherenkov radiation emission occurs at propagation distance of $\sim 10 \text{ cm}$, where the phase-matching is provided by the dispersion characteristic of the resonance. The efficient energy transfer across the resonance towards longer wavelength is observed. However, SPM continues to play significant role in spectral broadening in the case of Kagome fiber unlike in ARHCF. It takes longer propagation lengths to achieve efficient energy transfer towards UV due to lack of resonance (Figure 6.7c).

iii. **Four-wave mixing**

It is well known that complicated FWM processes play a dominant role in supercontinuum generation after the fission process [107]. The various combinations of the strong signal components emerging in the supercontinuum process can be

attributed to perfectly phase-matched signal and idler branches. It explains the further extent of the simulated spectrum to both sides beyond the extent of the initial Cherenkov radiation generation. This process corresponds to a parametric four-wave mixing pumped by both the initial solitary wave and one of the two generated Cherenkov radiation (either the one in the visible or the one in the near-IR), leading to the phase-matching condition

$$\beta(\omega_{1,n}) + \beta(\omega_{2,n}) - \beta(\omega_s) - \beta(\omega_{\text{CR},n}) - \gamma(\omega_s)P_0 = 0 \quad (6.6)$$

where, $\beta(\omega_s)$ is the frequencies of the solitary wave, $\beta(\omega_{\text{CR},n})$ is the n_{th} generated Cherenkov radiation ($n=1,2$), $\beta(\omega_{1,n})$ is the corresponding signal and $\beta(\omega_{2,n})$ is the idler. Since the peak power P_0 of the solitary wave (those close to the strand resonance) dominates the other mixing partners only the nonlinear phase of the solitary wave is considered. However, the bandwidth of phase-matching processes to Cherenkov radiation generation is overwhelming and FWM signals are indistinguishable from Cherenkov radiation.

Regarding the impact of the third-harmonic, in both cases Kagome and anti-resonant fiber, the third-harmonic light is generated and probably frequency shifted by cross-phase modulation. However, this part of the field has no further impact on the broadening process in case of the Kagome-type fiber. But also in case of the ARHCF, an independent evolution of both Cherenkov radiation generation and third-harmonic generation is observed. If the third-harmonic would act as a seed for the Cherenkov radiation, it should be observed earlier to the onset of the Cherenkov radiation at around $3\omega_0$ than e.g. around $2\omega_0$ in the Figure 6.7a.

The simulations presented here neglect ionization nonlinearity in the model based on an experimental observation and on numerical estimations. Very high intensity is present at the fiber entrance when incoupling the light into the hollow core. Consequently, ionization is expected to happen mainly at the fiber input which is well-known from nonlinear pulse compression in hollow-core fibers. An experimental verification of appearing ionization relies on a nonlinear relation between input and output energy, as coupling into the fiber is modified in case of ionization-induced defocusing. Such kind of nonlinear behavior was, however, not observed in the experiments presented here,

as the transmission efficiency through the fiber was approximately constant across the entire range of input pulse energies used in the experiments; thus from the experimental perspective ionization was not an issue at the energy levels considered.

In experiment, the fiber exhibits multiple resonances allowing a possibility for cascaded phase-matching processes pushing the output spectrum further towards UV region. But, the resonance regions are lossy and propagating mode experiences an increased effective mode field area that results in reduced nonlinearity [105]. The spectrally trapped associated solitary waves near resonance will lose peak power as they propagate, resulting in the reduced conversion efficiencies of the cascaded process. Hence, smaller spectral bandwidth is observed in the experiment.

The simulations (Figure 6.7) and the group velocity dispersion presented in Figure 6.1 only include the lowest-order resonant at around 1 μm , with all other resonances located at shorter wavelength being neglected. It is known that the magnitude of the strand resonance (i.e., the bandwidth and magnitude of loss for a finite sample length) reduces towards increasing resonance orders, as the spectral extend of the domain of the dispersion anti-crossing reduces, which is in accordance with coupled mode theory (see for instance the example of a band gap fiber in Figure 3a of reference [108]). Thus the fiber design placed the strongest strand resonance in proximity to the laser pump wavelength and forcing the input pulse to experience the strongly changing group velocity dispersion. As a first step, it is sufficient to consider only one resonance in simulations since the strongly varying dispersion provides a large number of phase-matching opportunities regardless of the dispersion profile away from the fundamental resonance. Though simulations include single strand resonance, it reproduces the numerical analysis qualitatively when compared with the experimental observations. This confirms the dramatic impact of the one strong resonance on nonlinear pulse propagation. The simulations also show spectral (temporal) evolution as a function of propagation distance whereas in the experiment, the spectral evolution is measured as a function of input energy for practical reasons. These two dependences are fairly equivalent.

Generalized nonlinear Schrödinger equation

To elaborate the dynamics more precisely, further simulations using the generalized nonlinear Schrödinger equation (GNLSE) are carried out to estimate phase-matching conditions for Cherenkov radiation and modulation instability (MI). The GNLSE assume quasi monochromatic electric field and spectrum is situated around zero. This helps in easier analysis of MI and phase matching conditions. High frequency part in neglected in these simulations and is easier to generate the spectrograms. The observed spectral broadening can be explained as follows:

- i. Initial SPM creates new frequency components symmetrically around the pump pulse, leading to a temporal contraction of the pulse and increases the peak power (i.e., solitonic compression). The soliton numbers calculated from the initial pulse parameters is around 16 for a pulse energy of 12 μJ at krypton gas pressure of 6 bars.
- ii. Once the pulse spectrum extends into the domain of the strand resonance, a number of ultrafast states with solitonic character are excited due to the strongly changing group velocity dispersion (i.e., strong perturbation). These states are phase-matched to large number of Cherenkov radiation emission at the short and long-wavelength sides of the resonance, distributing the energy across the UV, VIS and near IR domains. For qualitative verification of this argumentation, calculation of phase-matching wavelengths to dispersive waves shown in Figure 6.8 is carried out. This shows the dependence on frequency shift relative to the initial pump wavelength (800 nm) and compressed pulse peak power. It is important to note that dispersive wave generation does not require the presence of "classical" solitons. The nonlinear phase-matching condition is given by

$$\beta(\omega) - \beta(\omega_s) + [\omega_s - \omega]\beta_1(\omega_s) - \gamma(\omega_s)P_0 = 0 \quad (6.7)$$

where pump frequency is ω_0 , wave number is β , $\beta_1 = \partial_\omega\beta$, the nonlinear parameter is γ , and the peak power of the pump wave P_0 . Eq. 6.7 is of general character and, as a consequence, can be applied to any kind of pump excitation which possesses sufficiently high peak power. This was demonstrated in [109] where

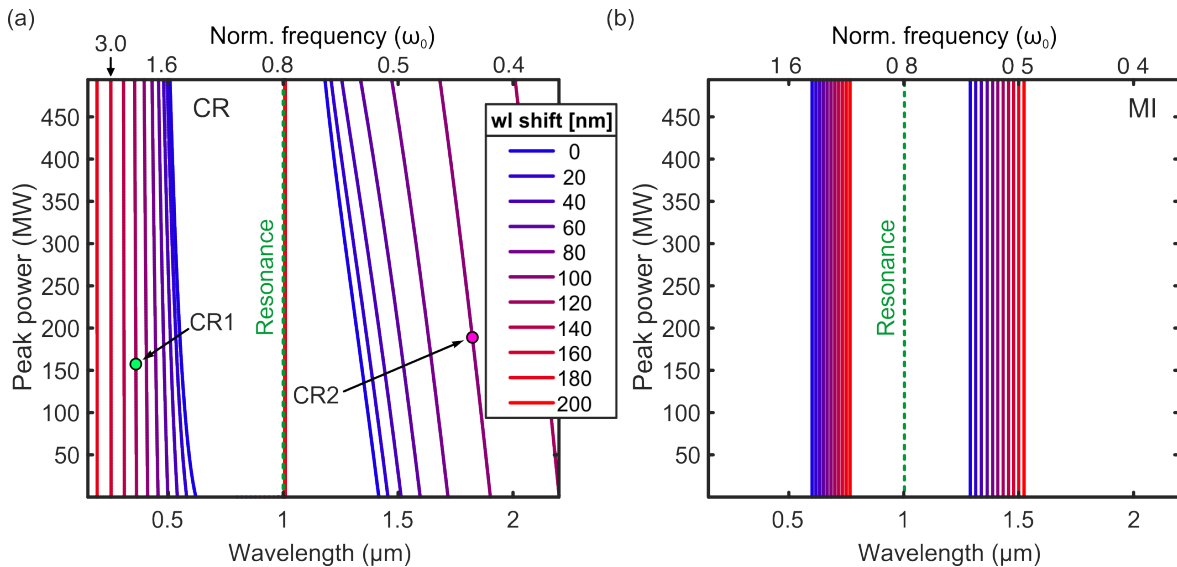


Figure 6.8: Perfect phase-matching condition for (a) resonant Cherenkov radiation (CR) and (b) modulation instabilities (MI) as functions of peak power along with wavelength detuning relative to central laser wavelength of 800, near the strand resonance (wavelength $1 \mu\text{m}$). The x-scale covers the normalized frequencies range from $5\omega_0$ to $0.4\omega_0$. The vertical dashed green lines show the resonance spectral positions in both plots. The phase-matching points of the two Cherenkov radiation bands indicated by CR1 (green dot) and R2 (magenta dot). The Cherenkov radiation bands are indicated in Figure 6.9 [23].

energy was transferred from a pulse propagating in the normal dispersion regime to its phase-matched counterpart in the anomalous dispersion regime. The bandwidth of possible phase-matching points in dependence of the center wavelength and peak power of the involved solitary wave is investigated here (see Figure 6.7a). Due to the large number of phase-matching points on both sides of the resonance within the extent of the measured spectral bandwidth (i.e., between $1.1 \mu\text{m}$ and $1.6 \mu\text{m}$ (0.5 and $0.7\omega_0$), and 0.25 and $0.55 \mu\text{m}$ (1.4 and $3.2\omega_0$)), it can be confirmed that multiple double-sided dispersive wave generation plays a key role in the underlying light generation process.

- iii. A further extent of the spectral bandwidth is anticipated as a result of phase matched four wave mixing processes between solitary waves and their generated dispersive waves. Additionally, the fiber used in the experiment features higher order resonance bands (i.e. at wavelengths $\sim 500 \text{ nm}$ and $\sim 250 \text{ nm}$). These resonances introduce additional modifications of the fiber dispersion and thus more potential phase-matching points for multiple cascaded effects down to UV wavelengths.
- iv. Modulation instabilities exhibit a characteristic symmetric spectral broadening

indicated by sideband modulations appearing simultaneously left and right of the SPM-modulated pump. Here, in contrast, the spectral evolution (Figures 6.7a and 6.9) shows a step-wise broadening with first a short-wavelength signal appearing around $1.4\omega_0$ at $z = 5$ cm, emerging before a second long-wavelength signal at $0.5\omega_0$ for a propagation distance of $z = 6$ cm. Such a step-wise, spectrally asymmetric process indicates multiple phase-matching processes rather than modulation instabilities.

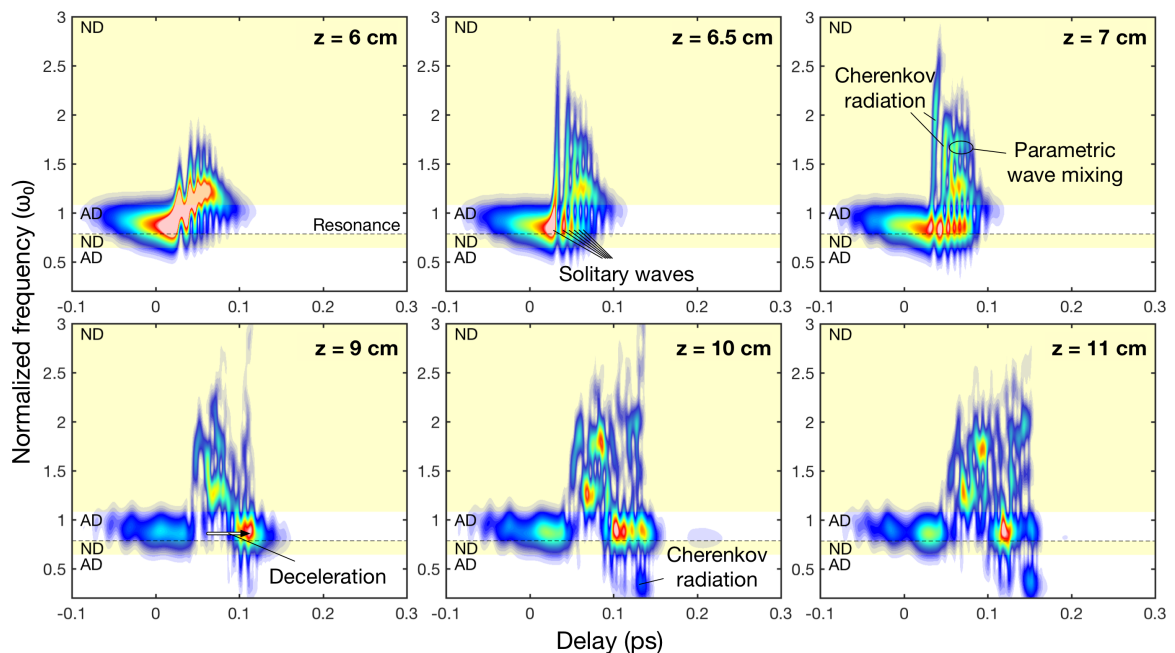


Figure 6.9: Spectro-temporal pulse evolution (i.e., spectrogram representation, linear scale) at selected positions inside the ARHCF (the corresponding position is indicated on the top of each plot). Normal dispersion (in yellow background) and anomalous dispersion (in white background) domains are labelled as ND and AD, respectively [23].

- v. The strong initial self-phase modulation pushes a large power fraction of the pulse into highly dispersive spectral domains. The non-adiabatic increase of the dispersion leads to a decreasing probability for MI to occur, which is well described in the review paper by *Dudley et. al.* [104].
- vi. The first order coherence of the generated spectra is shown in Figure 6.10. Simulations include uniformly distributed random phase noise into the UPPE solver and determine the first-order coherence by effectively averaging over 20 statistical realizations of spectra. One-photon-per-mode model with random phase $E_{\text{noise}}(\nu) = \sqrt{\frac{h\nu}{d\nu}} e^{i\varphi_{\text{rand}}}$ which is added on the pulse spectrum at the beginning of

each run (more details on the noise model can be found in [110]). For a given longitudinal position inside the gas-filled fiber, the spectral distribution of the first-order correlation function can be calculated by

$$|g_{mn}^{(1)}(\lambda)| = \left| \frac{\langle E_m^*(\lambda) E_n(\lambda) \rangle}{\sqrt{\langle E_m(\lambda)^2 \rangle \langle E_n(\lambda)^2 \rangle}} \right| \quad (6.8)$$

where E is the spectral amplitude of the electric field of the individual spectra at the respective wavelength, m and n run from 1 to 20 (over all permutations with $m \neq n$), and the triangular brackets denote an ensemble average (sum over all permuted products).

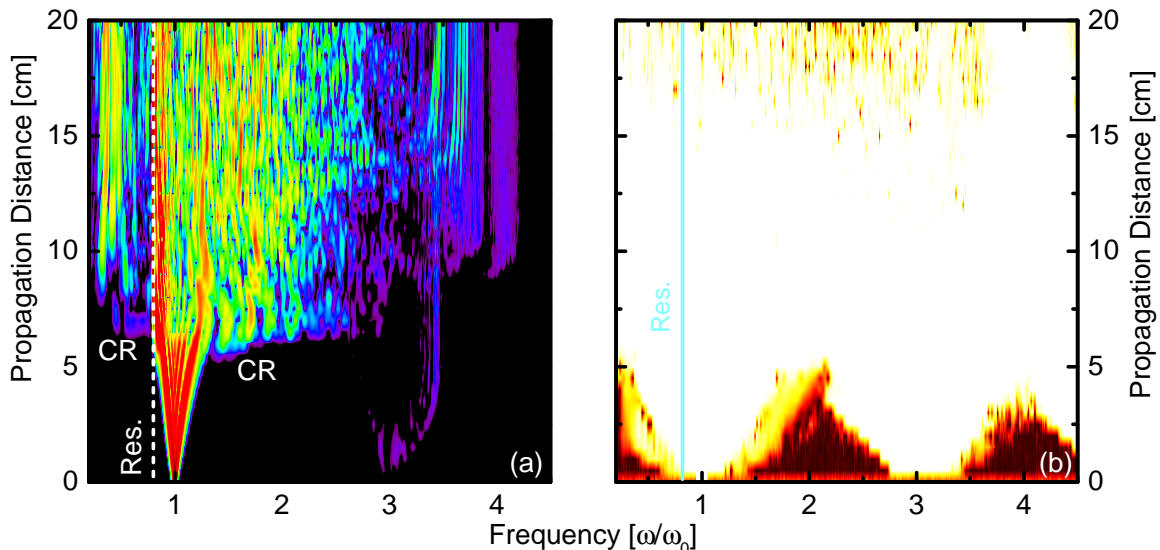


Figure 6.10: Coherence properties of the simulated spectral evolution in the gas filled ARHCF. (a) Spectral intensity evolution inside the ARHCF (core diameter 50 μm) as a function of propagating length with the group velocity dispersion profile shown in Figure 6.1. The colors refer to the different intensity values and defined at top left color bar (logarithmic scale, normalized to unity). (b) Corresponding plot of the first-order correlation function of the spectral distribution at different propagation lengths inside the fiber (white: unity (perfect coherence); dark red: no coherence). ω_0 refers to the central frequency of the input pulse ($\frac{2\pi c_0}{\omega_0} = 800 \text{ nm}$). The vertical blue line indicates the strand resonance and generated Cherenkov radiation bands are labelled as CR [23].

The simulations show unity coherence across the entire generated bandwidth even at large (initial) soliton numbers up to 57 (chosen limit of our test simulations), which is much larger than predicted by the coherence limit (MI is relevant for $N \gg 15$) given in literature. The results of the above calculations (presented

in Figures 6.9 and 6.10) clearly indicate that modulations instabilities do not dominate the spectral broadening.

The complexity of the spectrogram (Figure 6.9) data makes it challenging to identify all ultrafast nonlinear processes involved. However, three processes can be distinctly identified:

i. **Solitary waves**

The splitting of the pulse into a series of strong tempo-spectrally confined waveforms (e.g., at $z = 6.5$ cm), which are denoted as solitary waves.

ii. **Cherenkov radiation**

Two points of energy transfer (e.g., at $z = 7$ cm and $z = 10$ cm) to wave packets are observed where the phase matching wavelengths are satisfied for Cherenkov radiation in the UV and IR.

iii. **Parametric wave mixing**

Multiple domains of symmetric parametric wave mixing are observed. For e.g., at $z = 7$ cm solitary waves serve as seed signals and delayed SPM components as pump signals to generate strong idler waves around $1.7\omega_0$.

For propagation distances longer than 7 cm the spectrogram results reveal rather complex and sophisticated interactions between all the different processes. One effect that can be distinctly identified is the acceleration of the solitary wave(s) near the resonance (e.g., at $z = 9$ cm), as well as the subsequent generation of the second Cherenkov radiation wave in the infrared.

6.6 Supercontinuum generation in Raman-active gas

Spectral broadening in atomic gases due to SPM is induced by electronic Kerr effect which is instantaneous. However, diatomic molecules like nitrogen (N_2) are Raman-

active in nature. Raman response function is not instantaneous and has general form

$$R(\tau) = (1 - f_R)\delta(\tau) + f_R h_R(\tau) \quad (6.9)$$

where the first term corresponds to instantaneous electronic response and second term refers to the retarded molecular responses [27, 111, 112]. In presence of Raman-active medium, an intense light can undergo additional nonlinear process due to Raman effect providing a shift in input wavelength towards longer wavelengths. This assists in approaching the unique resonance GVD profile with lower input energies at a given gas pressure if nonlinear refractive index (n_2) of nitrogen is same as that of krypton. However, nitrogen molecule has n_2 approximately three time lower than of krypton. There will be an interplay of SPM and Raman effects in spectral broadening leading to supercontinuum generation. Due to experimental challenges like maintaining precise gradient gas pressure inside the fiber, having a fixed length of fiber for the two experiment and minor deviations (± 50 nm) in the central resonance wavelength for a give fiber piece, the comparison between krypton and nitrogen results are qualitative in nature.

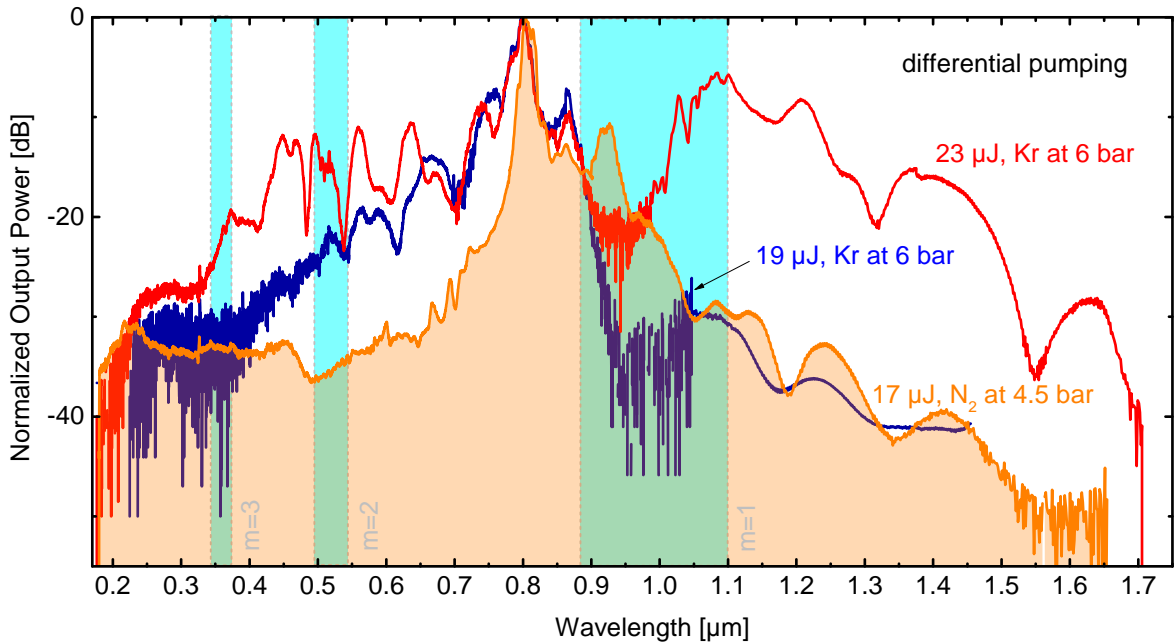


Figure 6.11: Supercontinuum Generation in Raman-active Gas - N_2 at 4.5 bar in differential pumping scheme (in orange). The experimental results from krypton filled ARHCF (Figures 6.5a and 6.5b) are shown in the background for comparison.

Figure 6.11 (in orange) shows the supercontinuum spectrum recorded at 17 μ J of output energy in N_2 filled ARHCF (supercontinuum spectrum from krypton filled,

differentially pumped experiments are shown from Figures 6.5a-b (in blue and red) are shown for comparison). At comparable energy levels of 17 μJ for N_2 at 4.5 bar and 19 μJ for Kr at 6 bar, output spectrum in the IR region are found to have similar spectral yield. One of the salient features in the case of N_2 is that the supercontinuum spectrum is continuous with significantly higher spectral content in the resonance region when compared with the Kr filled ARHCF. However, in the UV-VIS spectral region, Kr filled ARHCF has more spectral content due to larger SPM broadening because of higher n_2 , followed by Cherenkov radiation emission from phase matching in resonance GVD.

6.7 Summary

This chapter presented experimental results of supercontinuum generation in gas filled ARHCF. Results show that modal dispersion engineering via structural strand resonances in gas-filled ARHCFs offers a new degree of freedom in multioctave spectral broadening of output spectra from UV wavelengths towards the near infrared with high spectral density. The sophisticated dispersion landscapes of the ARHCF design plays a significant role in the spectral broadening and enables the generation of multiple octave supercontinua that span from deep UV to short-wave infrared wavelengths.

A 80 fs pulse having central wavelength of 800 nm is launched in Kr-filled ARHCF having ~ 495 nm thick silica strand which corresponds to resonance wavelength of ~ 1 μm . The resonance spectrum of the fiber is measured to be between 850 - 1200 nm due to variation in strand thickness along the fiber. The resulting abrupt GVD variation in the vicinity of 850 nm accelerates soliton dynamics as the SPM broadening of the pump light reaches the resonance region. At differential pumping of 6 bar of Kr-filled ARHCF, over three-octave-spectral broadening from 200 nm in UV to 1700 nm in IR is observed at output pulse energies of 23 μJ . Losses due to high-attenuation at strand resonance wavelength are considerably overcome by nonlinear interactions to generate a smooth spectra overall. The UPPE simulations show similar spectral broadening as observed in experiment providing qualitative confirmation and key understanding of the processes involved. Strongly varying GVD of the ARHCF at near resonance outperforms the dispersion contribution from the gas and the waveguide geometry, allowing access to new dispersion landscapes. Solitons propagating in such

non-adiabatically changing dispersion experience accelerated fission process. Further, the existence of multiple phase-matching possibilities emit resonant Cherenkov radiation on both sides of the resonance. Spectral broadening continues further by parametric wave mixing between solitary waves and emitted Cherenkov radiation. Subsequent cascade of similar processes and higher-order structural resonances influence extend the output spectrum. Experiments with Raman-active gas N_2 filled ARHCF show initiation of broadening due to resonance at lesser energies when compared with Kr which has three time higher nonlinear refractive index. This is attributed to Raman shift of the input spectrum, which further pushes the spectrum towards resonance region and delivers high output spectral content in the resonance region.

7 Few Cycle Pulse Generation in Negative Curvature ARHCF

7.1 Introduction

Few cycle pulses are of great interest across different fields of research due to its intense optical radiation that can interact with bound electronics of the exposed matter leading to extreme nonlinear interactions [113]. Few cycle pulses in the IR region ($\sim 1.8\mu\text{m} - 2\mu\text{m}$) have potential applications in fields like isolated attosecond pulse generation [114], high-harmonic generation [115], table-top particle acceleration [116], etc.

Conventional spectral broadening in gas-filled hollow-core capillary fibers by SPM needs an additional dispersion compensation module for dispersion compensation to obtain few-cycle pulses. The propagation losses in the capillary fiber scales inversely as the cube of the diameter. This demands large core diameter fibers to maintain a good coupling efficiency and need high input peak powers to generate sufficient spectral broadening that can be compressed down to few-cycle regime. However, in Kagome and ARHCFs propagation losses are independent of core diameter. It is possible to obtain increased nonlinearity by few orders for one tenth smaller bore diameter in comparison with capillary fibers. In the recent years, gas-filled Kagome fibers and ARHCFs have been successfully used to broaden the input spectrum and generate few-cycle pulses after a pulse compression system [12–14]. This chapter discusses generation of few cycle pulses directly from the gas filled NC-ARHCF with no additional pulse compression schemes.

The single-ring polygon core shaped ARHCFs discussed in earlier chapters do not transmit beyond silica cut-off wavelength. The NC-ARHCF silica fibers can have transmission spectrum well beyond silica transmission cut-off. NC-ARHCF can transmit light up to mid-IR wavelength unlike single ring ARHCF. The NC-ARHCFs are also

known to preserve the polarization state, as there is no large birefringence is introduced in the structural design of the fiber. These advantages make gas-filled NC-ARHCFs an ideal candidate to achieve pulse compression by SPM broadening at longer wavelengths.

When the pump wavelength is situated closer to resonance wavelength in any gas-filled ARHCF, it leads to accelerated soliton-fission like process (as discussed in chapter 6). This is detrimental to obtain smooth temporal profile at high energy. Hence, it is important to pump away from the resonance region to obtain a clean temporal profile of the output pulse. The experiment discussed in this chapter is carried out in the group of Prof. François Légaré at Advanced Laser Light Source situated at National Institute of Scientific Research - Energy, Materials and Telecommunications (*INRS-EMT*), Quebec, Canada.

The properties of NC-ARHCF used to generate few cycle pulses are introduced in section 7.2. Experimental set up including the temporal characterization unit is detailed in section 7.3. Experimental results are discussed in section 7.4 and summarized in the final section 7.5.

7.2 NC-ARHCF Properties

The revolver type of ARHCF considered in this experiment has 7 untouched thin tubes forming the nodeless negative-curvature hollow-core (inset of Figure 7.1 shows the SEM image of the fiber). This nodeless capillary structure is fabricated by the Beijing University of Technology (fabrication details are found elsewhere in [117]). The core diameter of the fiber is $\sim 55 \mu\text{m}$, cladding ring diameter is $\sim 22 \mu\text{m}$ and strand thickness is $\sim 585 \text{ nm}$. The fundamental resonance λ_1 is situated at $\sim 1.2 \mu\text{m}$. Further, this fiber guides light from $\sim 1.2 \mu\text{m}$ to mid-IR wavelengths $\sim 3 \mu\text{m}$. There is no transmission for the wavelengths $< 1.2 \mu\text{m}$. Figure 7.1 shows the calculated (by FEM simulations) variation of effective refractive index (left y-axis) and GVD (right y-axis) as a function of wavelength for the fundamental mode. The inset in the lower half of Figure 7.1 shows the close-up view of the strongly varying GVD in the resonance region.

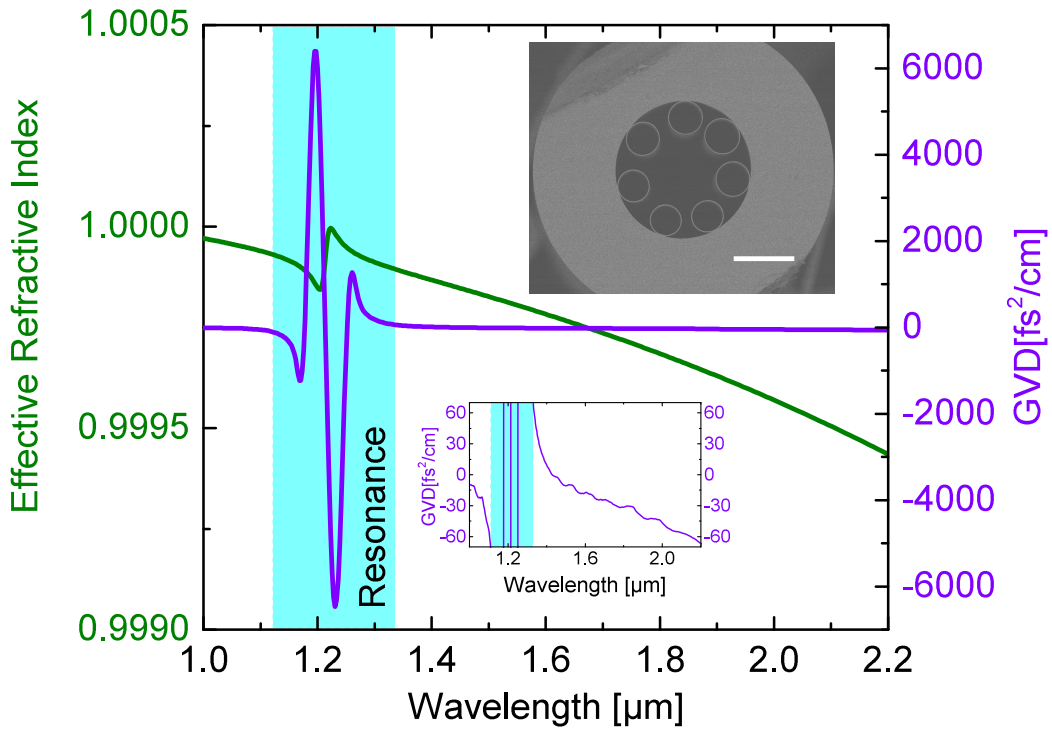


Figure 7.1: Properties of NC-ARHCF: Effective refractive index (left y-axis in green) and corresponding GVD (right y-axis in violet) for the fundamental mode of the NC-ARHCF. Resonance region is marked in blue. [inset (top): SEM image of 7 ringed NC-ARHCF, white scale bar corresponds to length of 50 μm ; inset (bottom) shows abrupt GVD variation in the resonance region].

7.3 Experimental set up

Conceptually, the experiment set up is similar to the one discussed in chapter 6 with additional temporal characterization unit. About 120 cm long NC-ARHCF is mounted on *few-cycle Inc.* fiber mounts, connected to gas cells as shown in Figure 7.2. CaF_2 windows having thickness of 2 mm form the window of the gas cells. Input end of the fiber is maintained under vacuum conditions (10s of mbar in G1). A constant Ar-gas pressure is maintained in output gas cell G2 maintaining a gradient of pressure inside the fiber.

Laser pulses for the experiment are generated by the Ti:Sapphire laser system. Ti:Sapphire oscillator (*KM labs*) output is amplified by two multi-pass chirped pulse amplifiers. The amplifier output delivers 35 fs pulses at energy of 1.6 mJ at repetition rate of 2.5 kHz. This output pumps the TOPAS which is white-light seeded optical parametric amplifier. The first difference frequency generation stage generates idler at

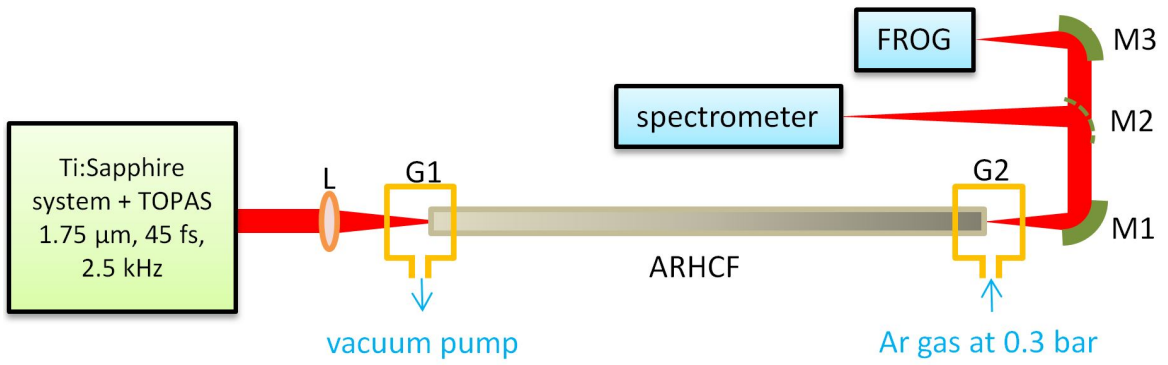


Figure 7.2: Experimental set up self pulse compression in NC-ARHCF (details can be found in the main text).

1.75 μm and the second stage amplification occurs in type-II BBO crystal delivering ~ 300 μJ of output energy.

The lens L1 couples the input light into NC-ARHCF with throughput efficiency of $\sim 50\%$. The concave mirror ($f = 20$ cm) collimates the output from the fiber. The flipper concave mirror M2 focuses the light into the spectrometer (*Ocean optics NIR256*) to record the spectrum, and mirror M3 guides the output into Frequency Resolved Optical Gating (FROG) for temporal characterization.

7.4 Results and Discussion

The experiment is carried out at fixed output energy of 18 μJ, the maximum energy that can be extracted from the fiber before ionisation like effects observed at the input of the fiber. At 18 μJ of output energy in completely evacuated fiber, argon gas pressure in the output cell G2 is gradually increased to record the shortest possible pulse duration that can be measured by the FROG technique.

Spectral characterization

The Figure 7.3 shows the measured input spectrum in the evacuated fiber (shown in dotted red line) and has pulse width of ~ 45 fs. The broadened output spectrum (in red and shaded) is recorded at 0.3 bar of argon pressure in the output cell. The broadening extends from 1.3 μm to 2.2 μm spanning over bandwidth of 900 nm. A dip of ~ 10 dB at the central wavelength can be observed in the output spectrum and this indicates the

spectral broadening caused by SPM. The pulse propagation in NC-ARHCF is modelled in UPPE (no loss included) and the simulated output spectrum (in blue) qualitatively matches with the experiment result (in red). The simulation peak at $\sim 1.25 \mu\text{m}$ resides in the lossy resonance region and is not observed in the experiment.

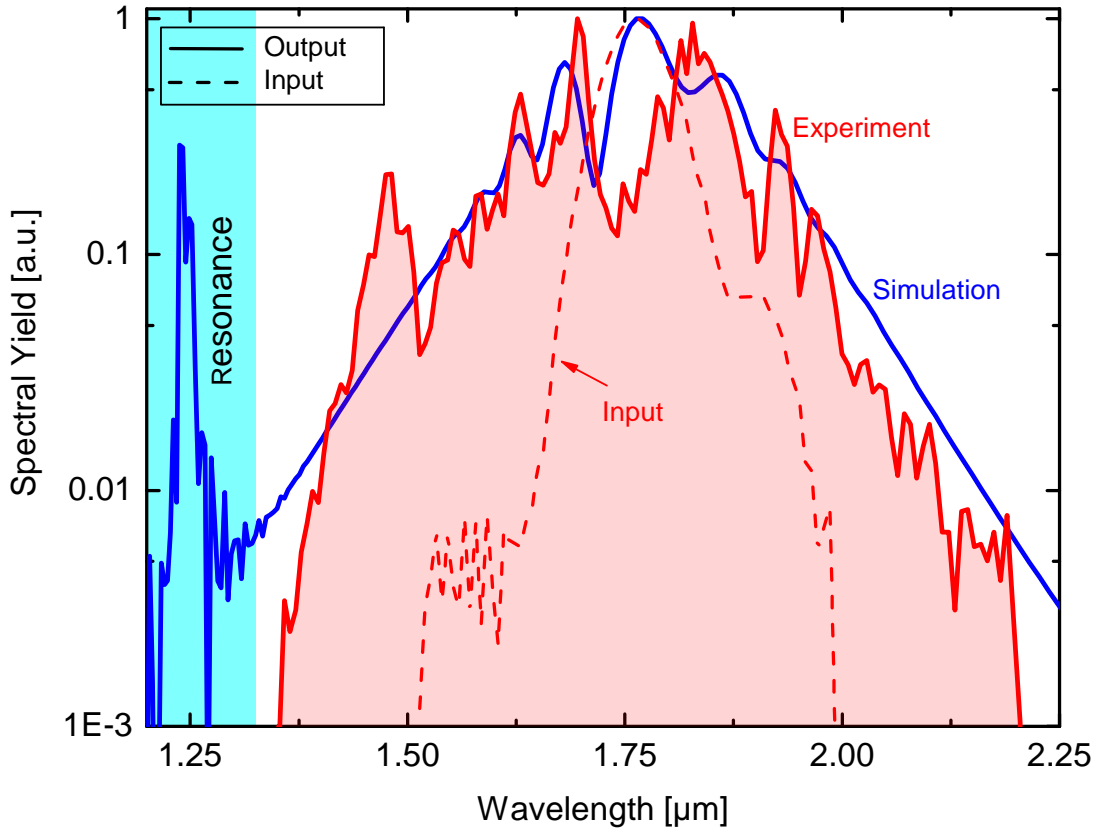


Figure 7.3: Spectral broadening in 1.2 m long differentially pumped (input end in vacuum and output maintained at 0.3 bar Argon gas) NC-ARHCF (in red); input spectrum (in red - dashed line) and output spectrum (in red and shaded); Spectral profile from UPPE simulations is shown in dark blue; resonance region is marked in light blue color

Temporal characterization

Temporal characterization is carried out using home built second harmonic frequency resolved optical gating (FROG) in 100 μm thick BBO crystal.

The Figure 7.4a-b show the measured and reconstructed FROG traces, respectively. The reconstruction has an error of 0.55%. The retrieved pulse duration measures 15 fs (shown in Figure 7.5 in red). This corresponds to ~ 2.5 cycle at wavelength of 1.75 μm (1 cycle ≈ 5.83 fs at 1.75 μm) and has peak power of >1 GW. The retrieved pulse has

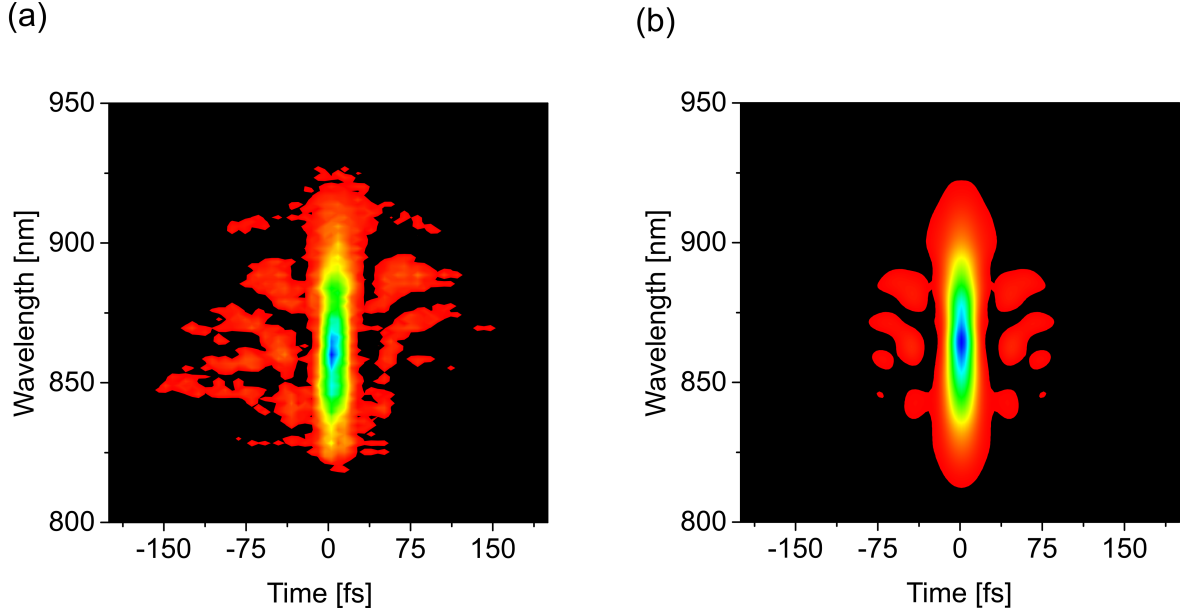


Figure 7.4: FROG trace of generated few-cycle pulse in NC-ARHCF (a) measured (b) retrieved

flat temporal phase and there is a possibility to compress the pulses down to transform limited pulse width of 14 fs.

The numerical simulations based on the UPPE [24] for the fundamental mode of the fiber and the Gaussian input pulse with the duration and energy corresponding to the experimental conditions are carried out. The dispersion profile for the fundamental mode for the selected NC-ARHCF is calculated by finite-difference element simulations in COMSOL [82]. Similar to hexagon core AHRCF simulation, the frequency dependence of the effective mode index is fitted with the functional form of the Lorentz derivative [23] (see Figure 7.1). The simulated output spectrum agrees well with the experimentally measured as shown in Figure 7.3 (in blue). The losses are neglected in these simulations. Hence, the dispersive wave emission peak situated in the resonance spectrum at $1.25 \mu\text{m}$ is not observed in the experiment though predicted by simulations. The temporal profile of the self-compressed pulse is shown in Figure 7.5 (in blue). It is in good agreement with the FROG trace reconstructed from the experimental measurement.

Analysis of the spectral and temporal dynamics in numerical simulations suggest that self-compression proceeds by conventional soliton self-compression mechanism [118]. In this experiment, the input laser pulse spectrum is far from the resonance region. Spectral broadening does not reach the resonance spectral region and numerical simulations confirm the self-compression along the fiber length.

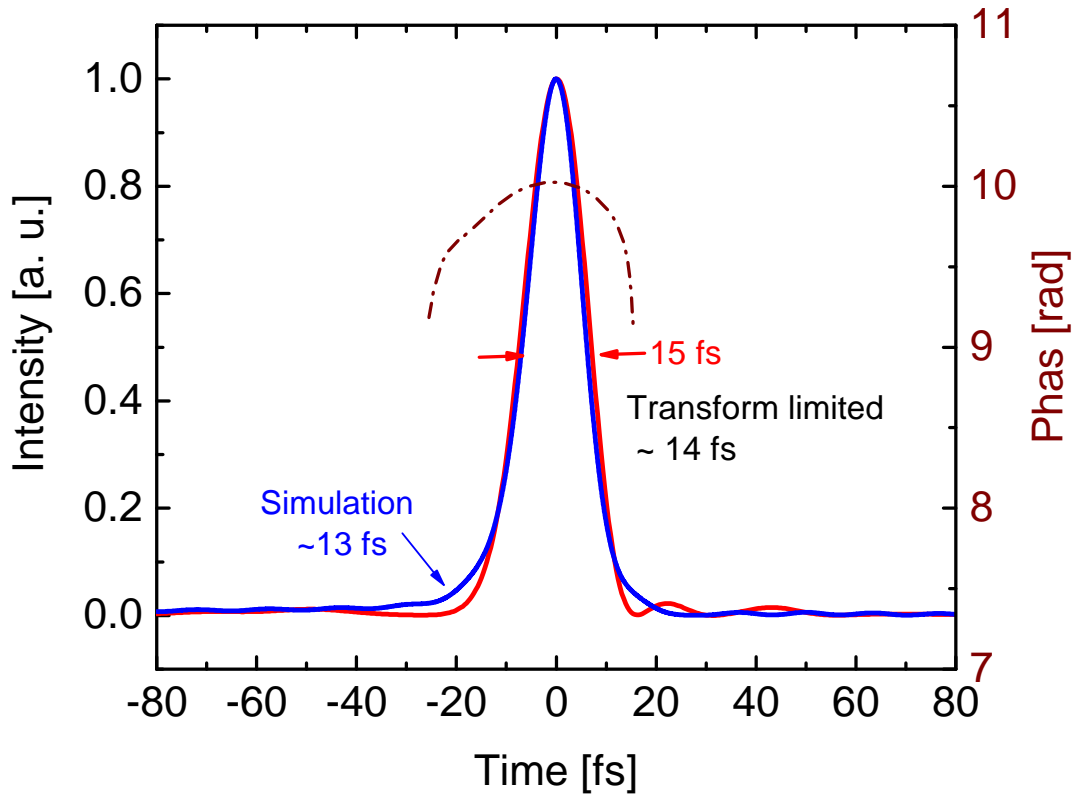


Figure 7.5: Retrieved temporal intensity profile (shown in red) and retrieved phase (in brown). Temporal intensity profile obtained from UPPE simulations (shown in blue).

7.5 Summary

This chapter demonstrates the few cycle pulse generation in 1.2 m long Ar-filled NC-ARHCF. The pump wavelength is away from the resonance to achieve gradual spectral broadening by SPM. The results show spectral broadening of >900 nm at output energy of $18 \mu\text{J}$ and at central wavelength of $1.75 \mu\text{m}$. Simulation shows self-compression of the output pulses to 2.5 cycle in ARHCF and 2 mm thick CaF_2 output window requiring no external compressor.

8 Summary and Outlook

The aim of this thesis is to study nonlinear light matter interactions in gas filled ARHCFs. The work involved characterization of optical propagation properties of novel ARHCF structures and study of spectral and temporal evolution in gas-filled ARHCF due to nonlinear optical effects.

The GVD profile of the hexagon core ARHCF near the structural resonance was investigated in a balanced Mach-Zehnder interferometer. GVD variations by few orders of magnitude near resonance were successfully measured in the vicinity of resonance as predicted by the analytical model developed in this work [20, 76]. The Fourier method involved for data analysis provided an advantage over other data analysis methods in terms of direct measurement of GVD with a single interferogram spreading over a bandwidth of hundreds of nanometers [80]. The result shows GVD variation of hundreds of fs^2/cm in proximity of the geometry-induced resonance wavelength. It is possible to precisely design the strand thickness and control the position of resonance wavelength. This paves way towards fibers having unique dispersion properties with niche applications in various different fields like telecommunication, supercontinuum generation and beam delivery.

Polarization evolution in different polygon shaped core ARHCFs allowed studying the structural influence on the polarization of the propagating light. The experimental results indicate that the dependence of a geometry-induced polarization behaviour exists in ARHCF. The structural deviations from an ideal polygonal core geometry induced birefringence and modal attenuation depending on the input polarization orientation with respect to fiber cross section. Further, it was also observed that ellipticity of the output light increased towards the resonance wavelength [88]. These results provide key knowledge on behaviour of cornered-core ARHCFs for linearly polarized input light and have practical relevance in fields such as high harmonic generation, interferometric

applications, nonlinear photonics or metrology.

Study of nonlinear spectral broadening in krypton-filled hexagon core shaped ARHCF yielded over three octaves wide spectral broadening at output energies of $\sim 23 \mu\text{J}$ due to strong non-adiabatic spectral dynamics of solitons near the resonance and emission of dispersive waves on both sides of the resonance spectrum [23]. The abrupt change in GVD profile plays a significant role in the observed soliton dynamics. Dispersion variation due to resonance becomes significant in the vicinity of the resonant wavelength such that dispersion due to geometrical shape of the waveguide and the filled gas play a negligible role in spectral broadening. The numerical simulations provide qualitative insight into the sophisticated nonlinear processes that are fuelled by strongly varying GVD near resonance wavelength, which provides a number of phase matching opportunities to generate Cherenkov radiation.

The nonlinear spectral broadening effect was able to fill up a significant fraction of the high-loss regions. It is important to note that the loss is significantly increased at resonance, but is still finite for the non-ideal waveguide used in the experiments. The actual broadening happened on a propagation distance which is so short that the actual finite loss becomes less significant, although the signatures of the loss distribution in the generated spectra were observed. This work shows how to efficiently exploit dispersion-engineered strand resonance for broadband white light generation which offers a new powerful tool for nonlinear system design in general. Particular interesting is the fact that the presented concept of strand resonance tuning allows to up-scale the hollow-core diameter without substantially changing the pulse dispersion - a situation which is hard to achieve in solid-core fibers. However, maintaining linear polarization of the propagating mode is challenging in cornered ARHCF as discussed in Chapter 5.

One of the disadvantages of pumping gas-filled ARHCFs closer to the resonance wavelength is the inability to extract a single output pulse at high input energies due to soliton fission. Pumping away from the resonance wavelength avoids the effects of abrupt change in GVD at resonance. Hence, nodeless negative curvature ARHCF was used generate few cycle pulses in gas-filled ARHCF at output energy of $\sim 18 \mu\text{J}$. The set up was differentially pumped with argon gas pressure of 0.3 bar at the output and the input end in vacuum conditions (10s of mbar). SPM-dominated spectral broadening yielded self-compressed 2.5 cycle pulse at wavelength of $1.75 \mu\text{m}$.

ARHCFs have large potential applications due to large number variable parameters in its design starting from the geometrical pattern of the fiber cross section, strand thickness, waveguide material etc.

Future research will focus on a deeper understanding of the soliton dynamics due strand resonance coupling, with an aim to reach towards either deep-UV or mid-IR wavelength in single ring ARHCF as predicted in our simulation [23]. Due to its unique spectral broadening and possibility of few cycle pulse generation at longer infrared wavelengths, this work is highly relevant in application-driven areas such as spectroscopy, microscopy, metrology and biophotonics.

References

- [1] COLLADON, D.: On the reflections of a ray of light inside a parabolic liquid stream. In: *Comptes Rendus* 15 (1842), S. 800–802
- [2] LEITER, S. B.: Microscope Illumination by Means of Quartz Rod. In: *J. Opt. Soc. Am.* 11 (1925), Aug, Nr. 2, 187–189. <http://www.osapublishing.org/abstract.cfm?URI=josa-11-2-187>
- [3] HOPKINS, H. H. ; KAPANY, N. S.: A flexible fiberscope using static scanning. In: *Nature* 173 (1954), 39-41. <http://dx.doi.org/10.1038/173039b0>
- [4] DUGUAY, M. A. ; KOKUBUN, Y. ; KOCH, T. L. ; PFEIFFER, Loren: Antiresonant reflecting optical waveguides in SiO₂-Si multilayer structures. In: *Applied Physics Letters* 49 (1986), Nr. 1, 13-15. <https://doi.org/10.1063/1.97085>
- [5] ARCHAMBAULT, J. L. ; BLACK, R. J. ; LACROIX, S. ; BURES, J.: Loss calculations for antiresonant waveguides. In: *Journal of Lightwave Technology* 11 (1993), March, Nr. 3, S. 416–423. – ISSN 0733–8724
- [6] MOLLENAUER, L. F. ; STOLEN, R. H.: The soliton laser. In: *Opt. Lett.* 9 (1984), Jan, Nr. 1, 13–15. <http://ol.osa.org/abstract.cfm?URI=ol-9-1-13>
- [7] STOLEN, R. H.: The Early Years of Fiber Nonlinear Optics. In: *J. Lightwave Technol.* 26 (2008), May, Nr. 9, 1021–1031. <http://jlt.osa.org/abstract.cfm?URI=jlt-26-9-1021>
- [8] RANKA, J. K. ; WINDELER, R. S. ; STENTZ, A. J.: Visible continuum generation in air-silica microstructure optical fibers with anomalous dispersion at 800 nm. In: *Opt. Lett.* 25 (2000), Jan, Nr. 1, 25–27. <http://ol.osa.org/abstract.cfm?URI=ol-25-1-25>
- [9] SHARPING, J. E. ; FIORENTINO, M. ; COKER, A. ; KUMAR, P. ; WINDELER, R. S.: Four-wave mixing in microstructure fiber. In: *Opt. Lett.* 26 (2001), Jul, Nr. 14, 1048–1050. <http://ol.osa.org/abstract.cfm?URI=ol-26-14-1048>
- [10] SHARPING, J. E. ; FIORENTINO, M. ; KUMAR, P. ; WINDELER, R. S.: All-optical switching based on cross-phase modulation in microstructure fiber. In: *IEEE Photonics Technology Letters* 14 (2002), Jan, Nr. 1, S. 77–79. – ISSN 1041–1135
- [11] FORK, R. L. ; CRUZ, C. H. B. ; BECKER, P. C. ; SHANK, C. V.: Compression of optical pulses to six femtoseconds by using cubic phase compensation. In: *Opt. Lett.* 12 (1987), Jul, Nr. 7, 483–485. <http://ol.osa.org/abstract.cfm?URI=ol-12-7-483>
- [12] MURARI, K. ; STEIN, G. J. ; CANKAYA, H. ; DEBORD, B. ; GÉRÔME, F. ; CIRMI, G. ; MÜCKE, O. D. ; LI, P. ; RUEHL, A. ; HARTL, I. ; HONG, K.-H. ; BENABID, F. ; KÄRTNER, F. X.: Kagome-fiber-based pulse compression of mid-infrared picosecond

- pulses from a Ho:YLF amplifier. In: *Optica* 3 (2016), Aug, Nr. 8, 816–822. <http://www.osapublishing.org/optica/abstract.cfm?URI=optica-3-8-816>
- [13] BALCIUNAS, T. ; FOURCADE-DUTIN, C. ; FAN, G. ; WITTING, T. ; VORONIN, A. A. ; ZHELTIKOV, A. M. ; GEROME, F. ; PAULUS, G. G. ; BALTUSKA, A. ; BENABID, F.: GeV electron beams from a centimetre-scale accelerator. In: *Nature Communications* 6 (2015), Jan, 1-7. <http://dx.doi.org/10.1038/ncomms7117>
- [14] GEBHARDT, M. ; GAIDA, C. ; HEUERMANN, T. ; STUTZKI, F. ; JAUREGUI, C. ; ANTONIO-LOPEZ, J. ; SCHULZGEN, A. ; AMEZCUA-CORREA, R. ; LIMPET, J. ; TÜNNERMANN, A.: Nonlinear pulse compression to 43;W GW-class few-cycle pulses at $2\mu\text{m}$ wavelength. In: *Opt. Lett.* 42 (2017), Oct, Nr. 20, 4179–4182. <http://ol.osa.org/abstract.cfm?URI=ol-42-20-4179>
- [15] RUSSELL, P. St. J. ; HÖLZER, P. ; CHANG, A. W. and A. W. and Abdolvand ; TRAVERS, J. C.: Hollow-core photonic crystal fibres for gas-based nonlinear optics. 8 (2014), 278–286. <http://dx.doi.org/10.1038/nphoton.2013.312>
- [16] MARCATILI, E. A. J. ; SCHMELTZER, R. A.: Hollow metallic and dielectric waveguides for long distance optical transmission and lasers. In: *The Bell System Technical Journal* 43 (1964), July, Nr. 4, S. 1783–1809. – ISSN 0005–8580
- [17] RENN, M. J. ; PASTEL, R. ; LEWANDOWSKI, H. J.: Laser Guidance and Trapping of Mesoscale Particles in Hollow-Core Optical Fibers. In: *Phys. Rev. Lett.* 82 (1999), Feb, 1574–1577. <https://link.aps.org/doi/10.1103/PhysRevLett.82.1574>
- [18] HARTUNG, A. ; KOBELKE, J. ; SCHWUCHOW, A. ; BIERLICH, J. ; POPP, J. ; SCHMIDT, M. A. ; FROSCHE, T.: Low-loss single-mode guidance in large-core antiresonant hollow-core fibers. In: *Opt. Lett.* 40 (2015), Jul, Nr. 14, 3432–3435. <http://ol.osa.org/abstract.cfm?URI=ol-40-14-3432>
- [19] BRADLEY, T. D. ; HAYES, J. R. ; CHEN, Y. ; JASION, G. T. ; SANDOGHCHI, S. R. ; SLAVIK, R. ; FOKOUA, E. N. ; BAWN, S. ; SAKR, H. ; DAVIDSON, I. A. ; TARANTA, A. ; THOMAS, J. P. ; PETROVICH, M. N. ; RICHARDSON, D. J. ; POLETTI, F.: Record Low-Loss 1.3dB/km Data Transmitting Antiresonant Hollow Core Fibre. In: *2018 European Conference on Optical Communication (ECOC)*, 2018, S. 1–3
- [20] GRIGOROVA, T. ; SOLLAPUR, R. ; HOFFMANN, A. ; HARTUNG, A. ; SCHWUCHOW, A. ; BIERLICH, J. ; KOBELKE, J. ; SCHMIDT, M. A. ; SPIELMANN, C.: Measurement of the Dispersion of an Antiresonant Hollow Core Fiber. In: *IEEE Photonics Journal* 10 (2018), Aug, Nr. 4, S. 1–6. – ISSN 1943–0655
- [21] YU, F. ; WADSWORTH, W. J. ; KNIGHT, J. C.: Low loss silica hollow core fibers for 3–4 μm spectral region. In: *Opt. Express* 20 (2012), May, Nr. 10, 11153–11158. <http://www.opticsexpress.org/abstract.cfm?URI=oe-20-10-11153>
- [22] ERMOLOV, A. ; MAK, K. F. ; FROSZ, M. H. ; TRAVERS, J. C. ; RUSSELL, P. St. J.: Supercontinuum generation in the vacuum ultraviolet through dispersive-wave and soliton-plasma interaction in a noble-gas-filled hollow-core photonic crystal fiber. In: *Phys. Rev. A* 92 (2015), Sep, 033821. <https://link.aps.org/doi/10.1103/PhysRevA.92.033821>

- [23] SOLLAPUR, R. ; KARTASHOV, D. ; ZUERCH, M. ; HOFFMANN, A. ; GRIGOROVA, T. ; SAUER, G. ; HARTUNG, A. ; SCHWUCHOW, A. ; BIERLICH, J. ; KOBELKE, J. ; CHEMNITZ, M. ; SCHMIDT, M. A. ; SPIELMANN, C.: Resonance-enhanced multi-octave supercontinuum generation in antiresonant hollow-core fibers. In: *Light: Science & Applications* 6 (2017), Dezember. <https://www.nature.com/articles/lisa2017124>
- [24] KOLESIK, M. ; MOLONEY, J. V. ; MLEJNEK, M.: Unidirectional Optical Pulse Propagation Equation. In: *Phys. Rev. Lett.* 89 (2002), Dec, 283902. <https://link.aps.org/doi/10.1103/PhysRevLett.89.283902>
- [25] KOLESIK, M. ; MOLONEY, J. V.: Nonlinear optical pulse propagation simulation: From Maxwell's to unidirectional equations. In: *Phys. Rev. E* 70 (2004), Sep, 036604. <https://link.aps.org/doi/10.1103/PhysRevE.70.036604>
- [26] COUAIRON, A. ; BRAMBILLA, E. ; CORTI, T. ; MAJUS, D. ; J. RAMÍREZ-GÓNGORA, O. de ; KOLESIK, M.: Practitioner's guide to laser pulse propagation models and simulation. In: *The European Physical Journal Special Topics* 199 (2011), Nov, Nr. 1, 5–76. <https://doi.org/10.1140/epjst/e2011-01503-3>. – ISSN 1951–6401
- [27] AGRAWAL, Govind.: *Nonlinear Fiber Optics 5th Edition*. Academic Press, 2013 <https://doi.org/10.1016/C2011-0-00045-5>
- [28] SHIMIZU, Fujio: Frequency Broadening in Liquids by a Short Light Pulse. In: *Phys. Rev. Lett.* 19 (1967), Nov, 1097–1100. <https://link.aps.org/doi/10.1103/PhysRevLett.19.1097>
- [29] STOLEN, R. H. ; LIN, Chinlon: Self-phase-modulation in silica optical fibers. In: *Phys. Rev. A* 17 (1978), Apr, 1448–1453. <https://link.aps.org/doi/10.1103/PhysRevA.17.1448>
- [30] DEMARTINI, F. ; TOWNES, C. H. ; GUSTAFSON, T. K. ; KELLEY, P. L.: Self-Steepening of Light Pulses. In: *Phys. Rev.* 164 (1967), Dec, 312–323. <https://link.aps.org/doi/10.1103/PhysRev.164.312>
- [31] YANG, Guozhen ; SHEN, Y. R.: Spectral broadening of ultrashort pulses in a nonlinear medium. In: *Opt. Lett.* 9 (1984), Nov, Nr. 11, 510–512. <http://ol.osa.org/abstract.cfm?URI=ol-9-11-510>
- [32] BOYD, R. W.: *Nonlinear Optics, Third Edition*. 3rd. Orlando, FL, USA : Academic Press, Inc., 2008. – ISBN 0123694701, 9780123694706
- [33] ZAKHAROV, V.E. ; OSTROVSKY, L.A.: Modulation instability: The beginning. In: *Physica D: Nonlinear Phenomena* 238 (2009), Nr. 5, 540 - 548. <http://www.sciencedirect.com/science/article/pii/S0167278908004223>. – ISSN 0167–2789
- [34] REEVES, W. H. ; SKRYABIN, D. V. ; BIANCALANA, F. ; KNIGHT, J. C. ; RUSSELL, P. St. J. ; OMENETTO, F. G. ; EFIMOV, A. ; TAYLOR, A. J.: Transformation and control of ultra-short pulses in dispersion-engineered photonic crystal fibres. In: *Nature* 424 (2003), Aug, 511-515. <http://dx.doi.org/10.1038/nature01798>
- [35] AKHMEDIEV, N. N. ; KORNEEV, V. I.: Modulation instability and periodic solutions of the nonlinear Schrödinger equation. In: *Theoretical and Mathematical Physics* 69 (1986), Nov, Nr. 2, 1089–1093. <https://doi.org/10.1007/BF01037866>. – ISSN 1573–9333

- [36] DUDLEY, J. M. ; GENTY, G. ; DIAS, F. ; KIBLER, B. ; AKHMEDIEV, N.: Modulation instability, Akhmediev Breathers and continuous wave supercontinuum generation. In: *Opt. Express* 17 (2009), Nov, Nr. 24, 21497–21508. <http://www.opticsexpress.org/abstract.cfm?URI=oe-17-24-21497>
- [37] CARMAN, R. L. ; CHIAO, R. Y. ; KELLEY, P. L.: Observation of Degenerate Stimulated Four-Photon Interaction and Four-Wave Parametric Amplification. In: *Phys. Rev. Lett.* 17 (1966), Dec, 1281–1283. <https://link.aps.org/doi/10.1103/PhysRevLett.17.1281>
- [38] STOLEN, R.: Phase-matched-stimulated four-photon mixing in silica-fiber waveguides. In: *IEEE Journal of Quantum Electronics* 11 (1975), March, Nr. 3, S. 100–103. – ISSN 0018–9197
- [39] ALFANO, R. R. ; SHAPIRO, S. L.: Observation of Self-Phase Modulation and Small-Scale Filaments in Crystals and Glasses. In: *Phys. Rev. Lett.* 24 (1970), Mar, 592–594. <https://link.aps.org/doi/10.1103/PhysRevLett.24.592>
- [40] RAEI, R. ; EBNALI-HEIDARI, M. ; SAGHAEI, H.: Supercontinuum generation in organic liquid-liquid core-cladding photonic crystal fiber in visible and near-infrared regions. In: *J. Opt. Soc. Am. B* 35 (2018), Feb, Nr. 2, 323–330. <http://josab.osa.org/abstract.cfm?URI=josab-35-2-323>
- [41] GU, F. ; YU, H. ; FANG, W. ; TONG, L.: Low-threshold supercontinuum generation in semiconductor nanoribbons by continuous-wave pumping. In: *Opt. Express* 20 (2012), Apr, Nr. 8, 8667–8674. <http://www.opticsexpress.org/abstract.cfm?URI=oe-20-8-8667>
- [42] CORKUM, P. B. ; ROLLAND, Claude ; SRINIVASAN-RAO, T.: Supercontinuum Generation in Gases. In: *Phys. Rev. Lett.* 57 (1986), Nov, 2268–2271. <https://link.aps.org/doi/10.1103/PhysRevLett.57.2268>
- [43] HODEL, W. ; WEBER, H. P.: Decay of femtosecond higher-order solitons in an optical fiber induced by Raman self-pumping. In: *Opt. Lett.* 12 (1987), Nov, Nr. 11, 924–926. <http://ol.osa.org/abstract.cfm?URI=ol-12-11-924>
- [44] YANOVSKY, V. P. ; WISE, F. W.: Nonlinear propagation of high-power, sub-100-fs pulses near the zero-dispersion wavelength of an optical fiber. In: *Opt. Lett.* 19 (1994), Oct, Nr. 19, 1547–1549. <http://ol.osa.org/abstract.cfm?URI=ol-19-19-1547>
- [45] BOYER, G.: High-power femtosecond-pulse reshaping near the zero-dispersion wavelength of an optical fiber. In: *Opt. Lett.* 24 (1999), Jul, Nr. 14, 945–947. <http://ol.osa.org/abstract.cfm?URI=ol-24-14-945>
- [46] PEARCE, G. J. ; WIEDERHECKER, G. S. ; POULTON, C. G. ; BURGER, S. ; RUSSELL, P. St. J.: Models for guidance in kagome-structured hollow-core photonic crystal fibres. In: *Opt. Express* 15 (2007), Oct, Nr. 20, 12680–12685. <http://www.opticsexpress.org/abstract.cfm?URI=oe-15-20-12680>
- [47] COUNY, F. ; BENABID, F. ; ROBERTS, P. J. ; LIGHT, P. S. ; RAYMER, M. G.: Generation and Photonic Guidance of Multi-Octave Optical-Frequency Combs. In: *Science* 318 (2007), Nr. 5853, 1118–1121. <http://science.sciencemag.org/content/318/5853/1118>. – ISSN 0036–8075

- [48] ARGYROS, A. ; LEON-SAVAL, S. G. ; PLA, J. ; DOCHERTY, A.: Antiresonant reflection and inhibited coupling in hollow-core square lattice optical fibres. In: *Opt. Express* 16 (2008), Apr, Nr. 8, 5642–5648. <http://www.opticsexpress.org/abstract.cfm?URI=oe-16-8-5642>
- [49] ROBERTS, P. J. ; WILLIAMS, D. P. ; MANGAN, B. J. ; SABERT, H. ; COUNY, F. ; WADSWORTH, W. J. ; BIRKS, T. A. ; KNIGHT, J. C. ; RUSSELL, P. S.: Realizing low loss air core photonic crystal fibers by exploiting an antiresonant core surround. In: *Opt. Express* 13 (2005), Oct, Nr. 20, 8277–8285. <http://www.opticsexpress.org/abstract.cfm?URI=oe-13-20-8277>
- [50] JAWORSKI, P. ; YU, F. ; MAIER, R. R. ; WADSWORTH, W. J. ; KNIGHT, J. C. ; SHEPHARD, J. D. ; HAND, D. P.: Picosecond and nanosecond pulse delivery through a hollow-core Negative Curvature Fiber for micro-machining applications. In: *Opt. Express* 21 (2013), Sep, Nr. 19, 22742–22753. <http://www.opticsexpress.org/abstract.cfm?URI=oe-21-19-22742>
- [51] MICHIELETTO, M. ; LYNGSØ, J. K. ; JAKOBSEN, Ch. ; LÆGSGAARD, J. ; BANG, O. ; ALKESKJOLD, T. T.: Hollow-core fibers for high power pulse delivery. In: *Opt. Express* 24 (2016), Apr, Nr. 7, 7103–7119. <http://www.opticsexpress.org/abstract.cfm?URI=oe-24-7-7103>
- [52] WANG, Z. ; BELARDI, W. ; YU, F. ; WADSWORTH, W. J. ; KNIGHT, J. C.: Efficient diode-pumped mid-infrared emission from acetylene-filled hollow-core fiber. In: *Opt. Express* 22 (2014), Sep, Nr. 18, 21872–21878. <http://www.opticsexpress.org/abstract.cfm?URI=oe-22-18-21872>
- [53] NISSEN, M. ; DOHERTY, B. ; HAMPERL, J. ; KOBELKE, J. ; WEBER, K. ; HENKEL, T. ; SCHMIDT, M. A.: UV Absorption Spectroscopy in Water-Filled Antiresonant Hollow Core Fibers for Pharmaceutical Detection. In: *Sensors* 18 (2018), Nr. 2. <http://www.mdpi.com/1424-8220/18/2/478>. – ISSN 1424–8220
- [54] URICH, A. ; MAIER, R.R.J. ; YU, Fei ; KNIGHT, J.C. ; HAND, D.P. ; SHEPHARD, J.D.: Silica hollow core microstructured fibres for mid-infrared surgical applications. In: *Journal of Non-Crystalline Solids* 377 (2013), 236 - 239. <http://www.sciencedirect.com/science/article/pii/S0022309313001166>. – ISSN 0022–3093. – ISNOG 2012 Proceedings of the 18th International Symposium on Non-Oxide and New Optical Glasses Rennes, France, July 1-5, 2012
- [55] SOLLAPUR, R. ; SCHMIDT, B. E. ; LASSONDE, P. ; GAO, S. ; WANG, Y. ; WANG, P. ; LÉGARÉ, F. ; SPIELMANN, C.: 2.5 Cycle Pulses Obtained With Self Compression At 1.8 μm In Antiresonant Waveguides. In: *Conference on Lasers and Electro-Optics*, Optical Society of America, 2018, SW3N.3
- [56] KNIGHT, J. C. ; BIRKS, T. A. ; RUSSELL, P. St. J. ; ATKIN, D. M.: All-silica single-mode optical fiber with photonic crystal cladding. In: *Opt. Lett.* 21 (1996), Oct, Nr. 19, 1547–1549. <http://ol.osa.org/abstract.cfm?URI=ol-21-19-1547>
- [57] BIRKS, T. A. ; KNIGHT, J. C. ; RUSSELL, P. St. J.: Endlessly single-mode photonic crystal fiber. In: *Opt. Lett.* 22 (1997), Jul, Nr. 13, 961–963. <http://ol.osa.org/abstract.cfm?URI=ol-22-13-961>

- [58] KNIGHT, J. C. ; BIRKS, T. A. ; CREGAN, R. F. ; RUSSELL, P. S. J. ; SANDRO, P. D.: Large mode area photonic crystal fibre. In: *Electronics Letters* 34 (1998), June, Nr. 13, S. 1347–1348. – ISSN 0013–5194
- [59] CREGAN, R. F. ; MANGAN, B. J. ; KNIGHT, J. C. ; BIRKS, T. A. ; RUSSELL, P. St. J. ; ROBERTS, P. J. ; ALLAN, D. C.: Single-Mode Photonic Band Gap Guidance of Light in Air. In: *Science* 285 (1999), Nr. 5433, 1537–1539. <http://science.sciencemag.org/content/285/5433/1537>. – ISSN 0036–8075
- [60] BENABID, F. ; KNIGHT, J. C. ; ANTONOPOULOS, G. ; RUSSELL, P. St. J.: Stimulated Raman Scattering in Hydrogen-Filled Hollow-Core Photonic Crystal Fiber. In: *Science* 298 (2002), Nr. 5592, 399–402. <http://science.sciencemag.org/content/298/5592/399>. – ISSN 0036–8075
- [61] CHEN, Y. ; MULVAD, H. C. H. ; SANDOGHCHI, S. R. ; NUMKAM, E. ; BRADLEY, T. D. ; HAYES, J. R. ; WHEELER, N. V. ; JASION, G. T. ; ALAM, S. U. ; POLETTI, F. ; PETROVICH, M. N. ; RICHARDSON, D. J.: First demonstration of low loss, bend insensitive 37-cell hollow-core photonic bandgap fiber at 1 μm for high power delivery applications. In: *2016 Conference on Lasers and Electro-Optics (CLEO)*, 2016, S. 1–2
- [62] WANG, Y. Y. ; WHEELER, N. V. ; COUNY, F. ; ROBERTS, P. J. ; BENABID, F.: Low loss broadband transmission in hypocycloid-core Kagome hollow-core photonic crystal fiber. In: *Opt. Lett.* 36 (2011), Mar, Nr. 5, 669–671. <http://ol.osa.org/abstract.cfm?URI=ol-36-5-669>
- [63] EDAVALATH, N. N. ; FROSZ, M. H. ; MÉNARD, . ; RUSSELL, P. S.: Fabrication and side-coupling characterization of hexagonal lattice single-ring hollow-core PCFs. In: *Frontiers in Optics 2015*, Optical Society of America, 2015, FM3G.3
- [64] TSIMINIS, G. ; ROWLAND, K.J. ; SCHATNER, E.P. ; SPOONER, N.A. ; MONRO, T.M. ; EBENDORFF-HEIDEPRIEM, H.: Single-ring hollow core optical fibers made by glass billet extrusion for Raman sensing. In: *Opt. Express* 24 (2016), Mar, Nr. 6, 5911–5917. <http://www.opticsexpress.org/abstract.cfm?URI=oe-24-6-5911>
- [65] CHENGLI, W. ; WEIBLEN, R. J. ; MENYUK, C. R. ; HU, J.: Negative curvature fibers. In: *Adv. Opt. Photon.* 9 (2017), Sep, Nr. 3, 504–561. <http://aop.osa.org/abstract.cfm?URI=aop-9-3-504>
- [66] GATTASS, R. R. ; RHONEHOUSE, D. ; GIBSON, D. ; MCCLAIN, C. C. ; THAPA, R. ; NGUYEN, V. Q. ; BAYYA, S. S. ; WEIBLEN, R. J. ; MENYUK, C. R. ; SHAW, L. B. ; SANGHERA, J. S.: Infrared glass-based negative-curvature anti-resonant fibers fabricated through extrusion. In: *Opt. Express* 24 (2016), Oct, Nr. 22, 25697–25703. <http://www.opticsexpress.org/abstract.cfm?URI=oe-24-22-25697>
- [67] NEWKIRK, A. V. ; ANTONIO-LOPEZ, J. E. ; ANDERSON, J. ; ALVAREZ-AGUIRRE, R. ; EZNAVEH, Z. S. ; LOPEZ-GALMICHE, G. ; AMEZCUA-CORREA, R. ; SCHÜLZGEN, A.: Modal analysis of antiresonant hollow core fibers using S2 imaging. In: *Opt. Lett.* 41 (2016), Jul, Nr. 14, 3277–3280. <http://ol.osa.org/abstract.cfm?URI=ol-41-14-3277>
- [68] LIU, X. ; DING, W. ; WANG, Y. ; GAO, S. ; CAO, L. ; FENG, X. ; WANG, P.: Characterization of a liquid-filled nodeless anti-resonant fiber for biochemical sensing.

- In: *Opt. Lett.* 42 (2017), Feb, Nr. 4, 863–866. <http://ol.osa.org/abstract.cfm?URI=ol-42-4-863>
- [69] POLETTI, F.: Nested antiresonant nodeless hollow core fiber. In: *Opt. Express* 22 (2014), Oct, Nr. 20, 23807–23828. <http://www.opticsexpress.org/abstract.cfm?URI=oe-22-20-23807>
- [70] BUFETOV, I.A. ; KOSOLAPOV, A.F. ; GLADYSHEV, A.V. ; KOLYADIN, A.N. ; YATSENKO, Y. P. ; PRYAMIKOV, A.D. ; BIRIUKOV, A.S. ; DIANOV, E.M.: Hollow Core Fibers with Single and Double Nested Capillaries Cladding and Fiber Based Raman Lasers. In: *Lasers Congress 2016 (ASSL, LSC, LAC)*, Optical Society of America, 2016, AW3A.5
- [71] HASAN, Md I. ; AKHMEDIEV, N. ; CHANG, W.: Positive and negative curvatures nested in an antiresonant hollow-core fiber. In: *Opt. Lett.* 42 (2017), Feb, Nr. 4, 703–706. <http://ol.osa.org/abstract.cfm?URI=ol-42-4-703>
- [72] PRYAMIKOV, A. D. ; BIRIUKOV, A. S. ; KOSOLAPOV, A. F. ; PLOTNICHENKO, V. G. ; SEMJONOV, S. L. ; DIANOV, E. M.: Demonstration of a waveguide regime for a silica hollow - core microstructured optical fiber with a negative curvature of the core boundary in the spectral region $\geq 3.5 \mu\text{m}$. In: *Opt. Express* 19 (2011), Jan, Nr. 2, 1441–1448. <http://www.opticsexpress.org/abstract.cfm?URI=oe-19-2-1441>
- [73] ANTONIO-LOPEZ, J. E. ; HABIB, S. ; NEWKIRK, A. V. ; LOPEZ-GALMICHE, G. ; EZNAVEH, Z. S. ; ALVARADO-ZACARIAS, J. C. ; BANG, O. ; BACHE, M. ; SCHÄJLZGEN, A. ; CORREA, R. A.: Antiresonant hollow core fiber with seven nested capillaries. In: *2016 IEEE Photonics Conference (IPC)*, 2016, S. 402–403
- [74] LIU, X. ; FAN, Z. ; SHI, Z. ; MA, Y. ; YU, J. ; ZHANG, J.: Dual-core antiresonant hollow core fibers. In: *Opt. Express* 24 (2016), Jul, Nr. 15, 17453–17458. <http://www.opticsexpress.org/abstract.cfm?URI=oe-24-15-17453>
- [75] LITCHINITSER, N. M. ; ABEELUCK, A. K. ; HEADLEY, C. ; EGGLETON, B. J.: Antiresonant reflecting photonic crystal optical waveguides. In: *Opt. Lett.* 27 (2002), Sep, Nr. 18, 1592–1594. <http://ol.osa.org/abstract.cfm?URI=ol-27-18-1592>
- [76] ZEISBERGER, M. ; SCHMIDT, M. A.: Analytic model for the complex effective index of the leaky modes of tube-type anti-resonant hollow core fibers. In: *Scientific Reports* 7 (2017), Sept, 11761. <https://doi.org/10.1038/s41598-017-12234-5>
- [77] MARKOS, C. ; TRAVERS, J. C. ; ABDOLVAND, A. ; EGGLETON, B. J. ; BANG, O.: Hybrid photonic-crystal fiber. In: *Rev. Mod. Phys.* 89 (2017), Nov, 045003. <https://link.aps.org/doi/10.1103/RevModPhys.89.045003>
- [78] HAYES, J. R. ; SANDOGHCHI, S. R. ; BRADLEY, T. D. ; LIU, Z. ; SLAVÍK, R. ; GOUVEIA, M. A. ; WHEELER, N. V. ; JASION, G. ; CHEN, Y. ; FOKOUA, E. N. ; PETROVICH, M. N. ; RICHARDSON, D. J. ; POLETTI, F.: Antiresonant Hollow Core Fiber With an Octave Spanning Bandwidth for Short Haul Data Communications. In: *J. Lightwave Technol.* 35 (2017), Feb, Nr. 3, 437–442. <http://jlt.osa.org/abstract.cfm?URI=jlt-35-3-437>
- [79] GAO, S. ; WANG, Y. ; DING, W. ; JIANG, D. ; GU, S. ; ZHANG, X. ; WANG, P. ; YULIN, A. V.: Hollow-core conjoined-tube negative-curvature fibre with ultralow loss. In: *Nature Communications* 9 (2018), Jul, 2828. <https://doi.org/10.1038/s41467-018-05225-1>

- [80] GRÓSZ, T. ; KOVÁCS, A. P. ; KISS, M. ; SZIPŐCS, R.: Measurement of higher order chromatic dispersion in a photonic bandgap fiber: comparative study of spectral interferometric methods. In: *Appl. Opt.* 53 (2014), Mar, Nr. 9, 1929–1937. <http://ao.osa.org/abstract.cfm?URI=ao-53-9-1929>
- [81] TANI, F. ; KÖTTIG, F. ; NOVOA, D. ; KEDING, R. ; RUSSELL, P. S.: Effect of anti-crossings with cladding resonances on ultrafast nonlinear dynamics in gas-filled photonic crystal fibers. In: *Photon. Res.* 6 (2018), Feb, Nr. 2, 84–88. <http://www.osapublishing.org/prj/abstract.cfm?URI=prj-6-2-84>
- [82] COMSOL: COMSOL Multiphysics. (2018). www.comsol.com
- [83] MOUSAVI, S. A. ; SANDOGHCHI, S. R. ; RICHARDSON, D. J. ; POLETTI, F.: Broadband high birefringence and polarizing hollow core antiresonant fibers. In: *Opt. Express* 24 (2016), Oct, Nr. 20, 22943–22958. <http://www.opticsexpress.org/abstract.cfm?URI=oe-24-20-22943>
- [84] DING, W. ; WANG, Y.: Hybrid transmission bands and large birefringence in hollow-core anti-resonant fibers. In: *Opt. Express* 23 (2015), Aug, Nr. 16, 21165–21174. <http://www.opticsexpress.org/abstract.cfm?URI=oe-23-16-21165>
- [85] COLLETT, E.: Polarized light: fundamentals and applications. (1993)
- [86] JONES, J. A. ; D’ADDARIO, A. J. ; ROJEC, B. L. ; MILIONE, G. ; GALVEZ, E. J.: The Poincaré-sphere approach to polarization: Formalism and new labs with Poincaré beams. In: *American Journal of Physics* 84 (2016), Nr. 11, 822–835. <https://doi.org/10.1119/1.4960468>
- [87] MCISAAC, P. R.: Symmetry-Induced Modal Characteristics of Uniform Waveguides - II: Theory. In: *IEEE Transactions on Microwave Theory and Techniques* 23 (1975), May, Nr. 5, S. 429–433. – ISSN 0018–9480
- [88] JAYAKUMAR, N. ; SOLLAPUR, R. ; HOFFMANN, A. ; GRIGOROVA, T. ; HARTUNG, A. ; SCHWUCHOW, A. ; BIERLICH, J. ; KOBELKE, J. ; SCHMIDT, M. A. ; SPIELMANN, C.: Polarization evolution in single-ring antiresonant hollow-core fibers. In: *Appl. Opt.* 57 (2018), Oct, Nr. 29, 8529–8535. <http://ao.osa.org/abstract.cfm?URI=ao-57-29-8529>
- [89] FLEMING, J. W.: Dispersion in GeO₂–SiO₂ glasses. In: *Appl. Opt.* 23 (1984), Dec, Nr. 24, 4486–4493. <http://ao.osa.org/abstract.cfm?URI=ao-23-24-4486>
- [90] WIEDUWILT, T. ; TUNIZ, A. ; LINZEN, S. ; GOERKE, J. S. D. S. Dellith ; HÜBNER, U. ; SCHMIDT, M. A.: Ultrathin niobium nanofilms on fiber optical tapers – a new route towards low-loss hybrid plasmonic modes. In: *Scientific Reports* 5 (2015), Nov, 17060. <https://doi.org/10.1038/srep17060>
- [91] HASEGAWA, A. ; TAPPRT, F.: Transmission of stationary nonlinear optical pulses in dispersive dielectric fibers. I. Anomalous dispersion. In: *Appl. Phys. Lett.* 23 (1973), Aug, 142–144. <https://aip.scitation.org/doi/10.1063/1.1654836>
- [92] MOLLENAUER, L. F. ; STOLEN, R. H. ; GORDON, J. P.: Experimental Observation of Picosecond Pulse Narrowing and Solitons in Optical Fibers. In: *Phys. Rev. Lett.* 45 (1980), Sep, 1095–1098. <https://link.aps.org/doi/10.1103/PhysRevLett.45.1095>

- [93] NISOLI, M. ; SILVESTRI, S. D. ; SVELTO, O. ; SZIPÖCS, R. ; FERENCZ, K. ; SPIELMANN, Ch. ; SARTANIA, S. ; KRAUSZ, F.: Compression of high-energy laser pulses below 5 fs. In: *Opt. Lett.* 22 (1997), Apr, Nr. 8, 522–524. <http://ol.osa.org/abstract.cfm?URI=ol-22-8-522>
- [94] LIN, C. ; STOLEN, R.H.: New nanosecond continuum for excited-state spectroscopy. In: *Appl. Phys. Lett.* 28 (1976), Feb, 216-218. <https://aip.scitation.org/doi/10.1063/1.88702>
- [95] WADSWORTH, W. J. ; KNIGHT, J. C. ; ORTIGOSA-BLANCH, A. ; ARRIAGA, J. ; SILVESTRE, E. ; RUSSELL, P. S. J.: Soliton effects in photonic crystal fibres at 850 nm. In: *Electronics Letters* 36 (2000), Jan, Nr. 1, S. 53–55. – ISSN 0013–5194
- [96] WADSWORTH, W. J. ; ORTIGOSA-BLANCH, A. ; KNIGHT, J. C. ; BIRKS, T. A. ; MAN, T.-P. M. ; RUSSELL, P. St. J.: Supercontinuum generation in photonic crystal fibers and optical fiber tapers: a novel light source. In: *J. Opt. Soc. Am. B* 19 (2002), Sep, Nr. 9, 2148–2155. <http://josab.osa.org/abstract.cfm?URI=josab-19-9-2148>
- [97] KNIGHT, J. C.: Photonic crystal fibres. In: *J. Opt. Soc. Am. B* 424 (2003), Aug, 874-851. <http://dx.doi.org/10.1038/nature01940>
- [98] COUNY, F. ; BENABID, F. ; LIGHT, P. S.: Large-pitch kagome-structured hollow-core photonic crystal fiber. In: *Opt. Lett.* 31 (2006), Dec, Nr. 24, 3574–3576. <http://ol.osa.org/abstract.cfm?URI=ol-31-24-3574>
- [99] CASSATARO, M. ; NOVOA, D. ; GÜNENDI, M. C. ; EDAVALATH, N. N. ; FROSZ, M. H. ; TRAVERS, J. C. ; RUSSELL, P. S.: Generation of broadband mid-IR and UV light in gas-filled single-ring hollow-core PCF. In: *Opt. Express* 25 (2017), Apr, Nr. 7, 7637–7644. <http://www.opticsexpress.org/abstract.cfm?URI=oe-25-7-7637>
- [100] GAO, R. ; JIANG, Y. ; ZHAO, Yang: Magnetic field sensor based on anti-resonant reflecting guidance in the magnetic gel-coated hollow core fiber. In: *Opt. Lett.* 39 (2014), Nov, Nr. 21, 6293–6296. <http://ol.osa.org/abstract.cfm?URI=ol-39-21-6293>
- [101] PRÄKELT, A. ; WOLLENHAUPT, M. ; SARPE-TUDORAN, C. ; ASSION, A. ; BAUMERT, T.: Filling a spectral hole via self-phase modulation. In: *Appl. Phys. Lett.* 87 (2005), Jul. <https://aip.scitation.org/doi/abs/10.1063/1.2056589>
- [102] PERELOMOV, A.M. ; POPOV, V.S. ; TERENCEV, M.V.: Ionization of Atoms in an Alternating Electric Field. In: *J Exptl Theoret Phys.* 23 (1966), Nov, 1393-1409
- [103] DALGARNO, A. ; KINGSTON, A. E.: The refractive indices and Verdet constants of the inert gases. In: *Proceedings of the Royal Society of London A: Mathematical, Physical and Engineering Sciences* 259 (1960), Nr. 1298, 424–431. <http://rspa.royalsocietypublishing.org/content/259/1298/424>. – ISSN 0080–4630
- [104] DUDLEY, J. M. ; GENTY, G. ; COEN, S.: Supercontinuum generation in photonic crystal fiber. In: *Rev. Mod. Phys.* 78 (2006), Oct, 1135–1184. <https://link.aps.org/doi/10.1103/RevModPhys.78.1135>
- [105] PUREUR, V. ; DUDLEY, J. M.: Nonlinear spectral broadening of femtosecond pulses in solid-core photonic bandgap fibers. In: *Opt. Lett.* 35 (2010), Aug, Nr. 16, 2813–2815. <http://ol.osa.org/abstract.cfm?URI=ol-35-16-2813>

- [106] VANVINCQ, O. ; KUDLINSKI, A. ; BÉTOURNÉ, A. ; QUIQUEMPOIS, Y. ; BOUWMANS, G.: Extreme deceleration of the soliton self-frequency shift by the third-order dispersion in solid-core photonic bandgap fibers. In: *J. Opt. Soc. Am. B* 27 (2010), Nov, Nr. 11, 2328–2335. <http://josab.osa.org/abstract.cfm?URI=josab-27-11-2328>
- [107] SKRYABIN, D. V. ; YULIN, A. V.: Theory of generation of new frequencies by mixing of solitons and dispersive waves in optical fibers. In: *Phys. Rev. E* 72 (2005), Jul, 016619. <https://link.aps.org/doi/10.1103/PhysRevE.72.016619>
- [108] GRANZOW, N. ; UEBEL, P. ; SCHMIDT, M. A. ; TVERJANOVICH, A. S. ; WONDRAKZEK, L. ; RUSSELL, P. St. J.: Bandgap guidance in hybrid chalcogenide–silica photonic crystal fibers. In: *Opt. Lett.* 36 (2011), Jul, Nr. 13, 2432–2434. <http://ol.osa.org/abstract.cfm?URI=ol-36-13-2432>
- [109] WEBB, K. E. ; XU, Y. Q. ; ERKINTALO, M. ; MURDOCH, S. G.: Generalized dispersive wave emission in nonlinear fiber optics. In: *Opt. Lett.* 38 (2013), Jan, Nr. 2, 151–153. <http://ol.osa.org/abstract.cfm?URI=ol-38-2-151>
- [110] DRUMMOND, P. D. ; CORNEY, J. F.: Quantum noise in optical fibers. I. Stochastic equations. In: *J. Opt. Soc. Am. B* 18 (2001), Feb, Nr. 2, 139–152. <http://josab.osa.org/abstract.cfm?URI=josab-18-2-139>
- [111] LIN, Q. ; AGRAWAL, G. P.: Raman response function for silica fibers. In: *Opt. Lett.* 31 (2006), Nov, Nr. 21, 3086–3088. <http://ol.osa.org/abstract.cfm?URI=ol-31-21-3086>
- [112] STOLEN, R. H. ; GORDON, J. P. ; TOMLINSON, W. J. ; HAUS, H. A.: Raman response function of silica-core fibers. In: *J. Opt. Soc. Am. B* 6 (1989), Jun, Nr. 6, 1159–1166. <http://josab.osa.org/abstract.cfm?URI=josab-6-6-1159>
- [113] BRABEC, T. ; KRAUSZ, F.: Intense few-cycle laser fields: Frontiers of nonlinear optics. In: *Rev. Mod. Phys.* 72 (2000), Apr, 545–591. <https://link.aps.org/doi/10.1103/RevModPhys.72.545>
- [114] PAUL, P. M. ; TOMA, E. S. ; BREGER, P. ; MULLOT, G. ; AUGÉ, F. ; BALCOU, Ph. ; MULLER, H. G. ; AGOSTINI, P.: Observation of a Train of Attosecond Pulses from High Harmonic Generation. In: *Science* 292 (2001), Nr. 5522, 1689–1692. <http://science.sciencemag.org/content/292/5522/1689>. – ISSN 0036–8075
- [115] LEWENSTEIN, M. ; BALCOU, Ph. ; IVANOV, M. Y. ; L’HUILIER, Anne ; CORKUM, P. B.: Theory of high-harmonic generation by low-frequency laser fields. In: *Phys. Rev. A* 49 (1994), Mar, 2117–2132. <https://link.aps.org/doi/10.1103/PhysRevA.49.2117>
- [116] LEEMANS, W. P. ; NAGLER, B. ; GONSALVES, A. J. ; TĀŠTH, Cs. ; NAKAMURA, K. ; GEDDES, C. G. R. ; ESAREY, E. ; SCHROEDER, C. B. ; HOOKER, S. M.: GeV electron beams from a centimetre-scale accelerator. In: *Nature Physics* 2 (2006), Sept, 696–699. <http://dx.doi.org/10.1038/nphys418>
- [117] CAO, L. ; GAO, S. ; PENG, Z. ; WANG, X. ; WANG, Y. ; WANG, P.: High peak power 2.8 μm Raman laser in a methane-filled negative-curvature fiber. In: *Opt. Express* 26 (2018), Mar, Nr. 5, 5609–5615. <http://www.opticsexpress.org/abstract.cfm?URI=oe-26-5-5609>

- [118] CHEN, C. ; KELLEY, P. L.: Nonlinear pulse compression in optical fibers: scaling laws and numerical analysis. In: *J. Opt. Soc. Am. B* 19 (2002), Sep, Nr. 9, 1961–1967. <http://josab.osa.org/abstract.cfm?URI=josab-19-9-1961>

List of Abbreviations and Symbols

The following table lists abbreviations, acronyms, and symbols used throughout the thesis.

λ	Wavelength of the light.
\mathcal{F}	<i>Fourier Transform.</i>
$\chi^{(2)}$	Second order susceptibility.
$\chi^{(3)}$	Third order susceptibility.
c	Velocity of light in vacuum.
f	Focal length of a lens or a focusing mirror.
n	Linear refractive index.
n_2	Nonlinear refractive index.
ARHCF	Antiresonant Hollow-Core Fiber.
ARROW	Anti-Resonant Reflecting Optical Waveguiding.
CPA	Chirped Pulse Amplification.
CW	Cherenkov radiation.
FEM	Finte Element Method.
FROG	Frequency Resolved Optical Gating.
FWM	Four-Wave Mixing.
GNLSE	Generalised Nonlinear Schrödinger Equation.
GTP	Glan-Thompson Polarizer.
GVD	Group Velocity Dispersion.
HCF	Hollow-Core Fiber.
HWP	Half-Wave Plate.
IR	Infrared.
MI	Modulation Instability.
NC-ARHCF	Negative Curvature Antiresonant Hollow-Core Fiber.

NIR	Near Infrared.
NLSE	Nonlinear Schrödinger Equation.
PBG	Photonic Bandgap.
PCF	Photonic Crystal Fiber.
PD	Photodiode.
SMF	Single-Mode Fiber.
SPM	Self-Phase Modulation.
SWIR	Short Wavelength Infrared.
Ti:Sa	Titanium-doped Sapphire laser.
UPPE	Unidirectional Pulse Propagation Equation.
UV	Ultraviolet.
VIS	Visible.
XPM	Cross-Phase Modulation.
ZDW	Zero Dispersion Wavelength.

List of Figures

2.1	Self phase modulation in silica fiber	15
2.2	Higher order soliton	16
2.3	Evolution of self steepening	17
2.4	Modulation instability	18
2.5	Four wave mixing	19
3.1	SEM images of different types of HCFs	23
3.2	SEM image of different types of ARHCFs	25
3.3	Resonance condition of ARHCF	27
3.4	SEM image of single ring ARHCF	28
3.5	Measured loss profile of the ARHCF	29
3.6	Effective refractive index of the ARHCF	30
3.7	SEM images of single ring ARHCFs used in this experiment	31
3.8	SEM image of nodeless ARHCF	31
4.1	Experimental setup for GVD measurement in ARHCF	36
4.2	Recorded spectral interference fringes to measure GVD of the ARHCF	37
4.3	Fit for the extracted phase	39
4.4	Measured GVD profile of the ARHCF	42
5.1	Concept figure to study polarization evolution in ARHCF	45
5.2	Measured spectral distribution of the modal loss profile of the three different ARHCFs	47
5.3	Experimental setup for polarization evolution measurement	48
5.4	Polarization evolution in different ARHCFs at Ti:Sapphire wavelength 800 nm	49
5.5	Ellipticity variation as a function of input polarization orientation	49

5.6	Experimental set up for absolute ellipticity measurement as function of wavelength	50
5.7	Ellipticity variation as a function of wavelength	51
5.8	Slab waveguide model	52
5.9	Effect of relative core radius on birefringence	53
5.10	Slab waveguide model	54
5.11	Contour plots for variation of ϵ_{out} with polarization of the incident beam and wavelength	54
6.1	Comparison of group velocity dispersion between ARHCF and HCF . .	59
6.2	Supercontinuum generation experimental setup	60
6.3	Supercontinuum output - homogeneously gas filled ARHCF	62
6.4	Mode profile of the supercontinuum output	63
6.5	Supercontinuum output - differentially pumped ARHCF	65
6.6	Comparison between spectral evolution in ARHCF and Kagome fibers .	69
6.7	Simulation of nonlinear pulse propagation in ARHCF and Kagome-type fibers	70
6.8	Phase-matching for Cherenkov radiation	75
6.9	Spectro-temporal pulse evolution	76
6.10	Coherence properties of the simulated spectral evolution	77
6.11	Supercontinuum generation in Raman-active gas	79
7.1	Properties of NC-ARHCF	84
7.2	Experimental set up for self-pulse compression in ARHCF	85
7.3	Spectral broadening in gas-filled NC-ARHCF	86
7.4	FROG trace of generated few-cycle pulse in NC-ARHCF	87
7.5	Retrieved temporal intensity profile of few-cycle pulse in NC-ARHCF	88

List of Tables

3.1	Comparison of different silica fibers	32
4.1	Fitting parameters for the extracted phase	41
5.1	Details of the fibers used in the polarization evolution experiment.	47

List of Publications

Publications in Peer-reviewed Journals and Proceedings

R. Sollapur, D. Kartashov, B. Schmidt, P. Lassonde, S. Gao, Y. Wang, P. Wang, F. L egar e, and C. Spielmann, *Few cycle pulse generation by self-compression at 1.75 μm in antiresonant waveguides*, in preparation.

V. Ramu, U. Reddy G, J. Liu, P. Hoffmann, **R. Sollapur**, R. Wyrwa, S. Kupfer, C. Spielmann, U. Neugebauer and A. Schiller, *Two-Photon Excitation leads to CO-Release from Targetable Manganese(I) Triscarbonyl Complexes in solution, polymers and cells*, accepted in Chemistry - A European Journal.

N. Jayakumar, **R. Sollapur**, A. Hoffmann, T. Grigorova, A. Hartung, A. Schwuchow, J. Bierlich, J. Kobelke, M. A. Schmidt, and C. Spielmann, *Polarization evolution in antiresonant hollow core fiber*, Applied Optics, Vol. 57, 8529-8535, 2018.

T. Grigorova, **R. Sollapur**, A. Hoffmann, A. Hartung, A. Schwuchow, J. Bierlich, J. Kobelke, M. A. Schmidt, and C. Spielmann, *Measurement of the Dispersion of an Antiresonant Hollow Core Fiber*, IEEE Photonics Journal, Vol. 10, 4, 1-6, 2018.

R. Sollapur, D. Kartashov, M. Z urch, A. Hoffmann, T. Grigorova, G. Sauer, A. Hartung, A. Schwuchow, J. Bierlich, J. Kobelke, M. Chemnitz, M. Schmidt and C.

Spielmann, *Resonance-enhanced multi-octave supercontinuum generation in antiresonant hollow-core fibers*, Light: Science and Applications, Vol. **6**, e17124, 2017.

Conference Talks

R. Sollapur, J. Gagnon-Audet, A. Schwuchow, J. Kobelke, M. Schmidt and, C. Spielmann, *Supercontinuum generation in Argon filled antiresonant fibers*, The International Conference on Fiber Optics and Photonics, New Delhi, India, 2018 (to be held).

D. Kartashov, **R. Sollapur**, M. Zürch, M. Chemnitz, M. Schmidt, C. Spielmann, *Non-linear wave dynamics in anti-resonant hollow-core fibers*, Symposium on Nanophotonics and Metamaterials, St. Petersburg, Russia, 2018, **invited presentation**.

D. Kartashov, **R. Sollapur**, M. Zürch, M. Chemnitz, M. Schmidt, C. Spielmann, *Non-linear wave dynamics in anti-resonant hollow-core fibers*, Symposium on Nanophotonics and Metamaterials, St. Petersburg, Russia, 2018, **invited presentation**.

R. Sollapur, B. Schmidt, P. Lassonde, S. Gao, Y. Wang, P. Wang, F. Légaré, C. Spielmann, *2.5 cycle pulses obtained with self compression at 1.8 μm in antiresonant waveguides*, Conference on Lasers and Electro-Optics, San Jose, California, USA.

N. Jayakumar, **R. Sollapur**, A. Hoffmann, T. Grigorova, A. Hartung, A. Schwuchow, J. Bierlich, J. Kobelke, M. A. Schmidt, C. Spielmann, *Polarization evolution in antiresonant hollow core fibers*, Conference on Lasers and Electro-Optics, San Jose, California, USA, 2018.

R. Sollapur, D. Kartashov, M. Zürich, A. Hoffmann, T. Grigorova, G. Sauer, A. Hartung, A. Schwuchow, J. Bierlich, J. Kobelke, M. A. Schmidt, C. Spielmann, *Antiresonant hollow core fibers: a new platform to study nonlinear laser matter interaction in gas filled fibers*, GRK-CREATE Autumn School, Université Laval, Quebec City, Quebec, Canada, 2017.

R. Sollapur, D. Kartashov, M. Zürich, A. Hoffmann, T. Grigorova, G. Sauer, A. Hartung, A. Schwuchow, J. Bierlich, J. Kobelke, M. Chemnitz, M. A. Schmidt C. Spielmann, *Multi-octave supercontinuum in dispersion tuned antiresonant hollow-core fibers*, DoKDoK - Doctoral Student Conference on Optics, Suhl, Thuringia, Germany, 2017.

T. Grigorova, **R. Sollapur**, A. Hoffmann, D. Kartashov, M. Zürich, A. Hartung, A. Schwuchow, J. Bierlich, J. Kobelke, M. A. Schmidt, C. Spielmann, *Dispersion Measurement of Engineered Antiresonant Hollow-Core Fibers with Spectral Interferometry*, Conference on Lasers and Electro-Optics/Europe and the European Quantum Electronics, Munich, Bavaria Germany, 2017.

M. Zürich, **R. Sollapur**, D. Kartashov, A. Hoffmann, T. Grigorova, G. Sauer, A. Hartung, A. Schwuchow, J. Bierlich, J. Kobelke, M. A. Schmidt C. Spielmann, *Multi-octave supercontinuum driven by soliton explosion in dispersion-designed antiresonant hollow-core fibers*, Conference on Lasers and Electro-Optics, Munich, Bavaria, Germany, 2017.

R. Sollapur, D. Kartashov, M. Zürich, A. Hoffmann, A. Hartung, M. Schmidt, C. Spielmann, *Supercontinuum generation in gas-filled anti-resonant hollow-core fibers*, ICONO-LAT, Minsk, Belarusia, 2016, **invited presentation**.

R. Sollapur, D. Kartashov, M. Zürich, A. Hoffmann, T. Grigorova, G. Sauer, A. Hartung, A. Schwuchow, J. Bierlich, J. Kobelke, M. A. Schmidt, C. Spielmann, *Multi-octave supercontinuum generation in anti-resonant hollow core fibers*, Summer School of the GRK 2101, Abbe Center of Photonics, Jena, Thuringia, Germany 2016.

M.Zürch, **R. Sollapur**, A. Hoffmann, G. Sauer, A. Hartung, D. Kartashov, M. Schmidt, C. Spielmann, *Octave Broadband Supercontinuum Generation in Gas-Filled Anti-Resonant Hollow-Core Fiber*, Conference on Lasers and Electro-Optics, San Jose, California, USA 2016, **invited presentation**.

Conference Posters

M. Mircovich, **R. Sollapur**, A. Hoffmann, C. Spielmann, A. Hartung, A. Schwuchow, J. Bierlich, J. Kobelke, M. A. Schmidt, *Pulse generation and characterization for supercontinuum experiments*, Annual Fall Meeting of the APS Ohio-Region Section, American Physical Society, Oxford, Ohio, USA, 2017.

Ni Jayakumar, **R. Sollapur**, A. Hoffmann, T. Grigorova, A. Hartung, A. Schwuchow, J. Bierlich, J. Kobelke, M. A. Schmidt, C. Spielmann, *Polarization Evolution in Antiresonant Hollow-Core Fibers*, DoKDoK ? Doctoral Student Conference on Optics, Suhl, Thuringia, Germany, 2017.

R. Sollapur, D. Kartashov, M. Zürich, A. Hoffmann, T. Grigorova, A. Hartung, A. Schwuchow, J. Bierlich, J. Kobelke, M. A. Schmidt, C. Spielmann, *Dispersion-Designed Antiresonant Hollow-Core Fibers for Supercontinuum Generation by Soliton Explosion*, Conference on Lasers and Electro-Optics/Europe and the European Quantum Electronics, Munich, Bavaria, Germany, 2017.

T. Grigorova, **R. Sollapur**, A. Hoffmann, M. Schmidt, A. Hartung, M. Schmidt, C. Spielmann, *Dispersion measurements of a novel anti-resonant hollow-core fiber*, DoK-DoK - Doctoral Student Conference on Optics, Oppurg, Thuringia, Germany, 2016.

A. Hoffmann, M. Zürich, **R. Sollapur**, D. Kartashov, T. Grigorova, G. Sauer, A. Hartung, M. Schmidt, C. Spielmann, *Scaling supercontinuum generation in gas-filled hollow-core fibers*, Europhoton, Vienna, Austria, 2016.

R. Sollapur, M.Zürch, A. Hoffmann, G. Sauer, D. Kartashov, A. Hartung, M. Schmidt, C. Spielmann, *Multi-octave supercontinuum generation in gas-filled anti-resonant hollow-core fiber*, Siegmán International School on Lasers, The Institute of Photonic Sciences, Barcelona, Spain, 2016.

R. Sollapur, M.Zürch, A. Hoffmann, G. Sauer, D. Kartashov, M. Schmidt, C. Spielmann, *Nonlinear optics in gas-filled hollow-core fibers in the near and mid-IR*, The international workshop on "New Frontiers in Fiber Optics" , Leibniz Institute of Photonic Technology, Jena, Thuringia, Germany, 2016.

R. Sollapur, M.Zürch, A. Hoffmann, G. Sauer, D. Kartashov, M. Schmidt, C. Spielmann, *Nonlinear optics in gas-filled hollow-core fibers in the near and mid-IR*, German Canadian workshop, University of Toronto, Toronto, Ontario, Canada, 2015.

R. Sollapur, M.Zürch, A. Hoffmann, G. Sauer, D. Kartashov, M. Schmidt, C. Spielmann, *Nonlinear optics in gas-filled hollow-core fibers in the near and mid-IR*, DoKDoK - Doctoral Student Conference on Optics, Eisenach, Thuringia, Germany 2015.

Ehrenwörtliche Erklärung

Ich erkläre hiermit ehrenwörtlich, dass ich die vorliegende Arbeit selbständig, ohne unzulässige Hilfe Dritter und ohne Benutzung anderer als der angegebenen Hilfsmittel und Literatur angefertigt habe. Die aus anderen Quellen direkt oder indirekt übernommenen Daten und Konzepte sind unter Angabe der Quelle gekennzeichnet. Bei der Auswahl und Auswertung folgenden Materials bzw. der Beisteuerung von Material/Daten haben mir die nachstehend aufgeführten Personen in der jeweils beschriebenen Weise unentgeltlich geholfen:

1. Die Herstellung der verwendeten Sechseck-Kern-ARHCF und Einzelring-ARHCFs erfolgte in der Arbeitsgruppe von Prof. Dr. Markus A. Schmidt vom Leibniz-Institut für Photonische Technologien (IPHT). Die in dieser Arbeit verwendeten effektiven Brechungsindizes von Sechseck-Kern-ARHCF und Verlustmessungen von Einzelring-ARHCFs wurden ebenfalls in der Gruppe von Prof. Dr. Markus A. Schmidt mittels der Finite-Element-Methode simuliert (Abb. 3.5, 6.1).
2. Die Herstellung und die Bestimmung der effektiven Brechzahl (Abb 7.1) von negative Krümmungs-HCF erfolgte in der Gruppe von Prof. Yingying Wang vom Beijing Institute of Technology.
3. Die numerischen Simulationen der nichtlinearen Pulsausbreitung in gasgefüllten ARHCF, welche in dieser Arbeit diskutiert werden wurden von Dr. Daniil Kartash vom Institut für Optik und Quantenelektronik, Friedrich-Schiller-Universität Jena durchgeführt.

Weitere Personen waren an der inhaltlich-materiellen Erstellung der vorliegenden Arbeit nicht beteiligt. Insbesondere habe ich hierfür nicht die entgeltliche Hilfe von Vermittlungs- bzw. Beratungsdiensten (Promotionsberater oder andere Personen) in Anspruch genommen. Niemand hat von mir unmittelbar oder mittelbar geldwerte Leistungen für Arbeiten erhalten, die im Zusammenhang mit dem Inhalt der vorgelegten Dissertation stehen. Die Arbeit wurde bisher weder im In- noch im Ausland in gleicher oder ähnlicher Form einer anderen

Prüfungsbehörde vorgelegt. Die geltende Promotionsordnung der Physikalisch-Astronomischen Fakultät ist mir bekannt.

Ich versichere ehrenwörtlich, dass ich nach bestem Wissen die reine Wahrheit gesagt und nichts verschwiegen habe.

Jena, 5. Dezember 2018

Rudrakant Sollapur

Acknowledgments

During the course of my PhD, there are many individuals who have played a significant role in making this work possible. I like to express my gratitude to them.

Every aspect of this work has been under continuous supervision and support of my PhD guru Prof. Dr. Christian Spielmann. I thank him for offering to undertake my doctoral research work in his group. Over the last three years, he has provided numerous opportunities for my academic growth. This work would not have been possible without his continuous support and guidance. I express my gratitude to Prof. Spielmann.

My regular interactions with Prof. Dr. Markus Schmidt have always been very inspiring and motivating. This work has been performed in very close collaboration with his group. Regular meetings and discussions have accelerated this work immensely. I express my gratitude to Prof. Schmidt.

Prof. François Légaré hosted me for over six months at institute INRS-EMT in Canada. Working under his guidance in a large scale laser facility has been a new learning experience. I thank him for hosting me in his lab.

Dr. Daniil Kartashov has been there for me from the beginning of this doctoral work. His regular guidance either in the lab or discussions have been very helpful. I thank him for all the help and support he provided over last years. Dr. Bruno Schmidt played significant role during my research stay abroad in Canada. He has been a great colleague and motivator in accomplishing the task in hand. I express my gratitude to Dr. Schmidt.

Dedicated support from our lab engineer Michael Damm has been very valuable in designing the experiments carried out in this work. I thank to M. Damm for his invaluable help. I also wish to express sincere appreciation to lab engineers Antoine Laramée and Philippe Lassonde at INRS-EMT facility in Canada, who made sure laser beam available to me all the time.

Furthermore, I wish to express my sincere thanks to all my colleagues of the Quantum Electronics group. I wish to express my gratitude to Dr. Michael Zürich and Dr. Andreas Hoffmann, who provided initial help needed in the lab to begin my research work and were helpful in various discussions over last years. My colleagues Zhanna Samsonova, Richard Hollinger, Frederik Tuitje, Tobias Helk and our secretary Sara Dürer have been very helpful whenever I was in need of. From regular group lunches to movie nights, they have provided a

great working atmosphere. I express my gratitude to all of them.

I express my sincere thanks to all the undergraduate and graduate students who have helped in this work. Significant contributions from our previous master students Teodora Grigorova and Nikhil Jayakumar are much appreciated.

Our doctoral coordinator Dr. Anna Späthe needs a special mention here for her continuous help in every administrative aspect of my doctoral program. Support from Dr. Dorit Schmidt and Ms. Anja Kluge is also much appreciated. I thank all of them for their help over last three years.

I also want to thank the funding agency German Science Foundation (DFG) for supporting my doctoral studies via IRTG 2101 program. Special thanks to Prof. Dr. Stefan Nolte and Prof. Dr. Andreas Tünnermann for their continuous support in this program.

There are few people whom we meet along the way and become very close to us. Special thanks to Rohith, Swathi, Arya, Santhosha and Pooja for creating a home away home in Jena. I express my deepest appreciations from the bottom of my heart to Dr. Pankaj Mishra, Dr. Krishna Murari, Swathi Sasikumar, Dr. Peng Li, Vinicius Oliveira and Dr. Chenchen Wan for all the things which you did for me over the last few years of stay in Germany.

The seeds of my doctoral studies were sworn in about 25 years ago when my father got his PhD. He then motivated my mother pursue her doctoral studies. So here, I am writing this thesis and continuing family traditions. This work is only possible with unconditional love, support and caring that my parents have bestowed upon me over last decades. They have also made many sacrifices to make this day happen.

I came across my spiritual master Sadhguru Jaggi Vasudev few months into my doctoral studies. The tools of self-transformation that he offered have been of immense help and significantly contributed in conducting my PhD with joy. I bow down to his lotus feet for everything he has offered me.

Curriculum Vitae

Sollapur, Rudrakant

Born on 15-02-1988 in Hukkeri, India.

Education

1993-1997: Primary school

1997-2003: Higher secondary school

2003-2005: Pre-University Course

2005-2009: Bachelor in Telecommunication Engineering

Visvesvaraya Technological University, Karnataka, India

2010-2012: Master of Technology in Laser and Electro-Optics

Defence Institute of Advanced Technology, Maharashtra, India

2012-2013: Master of Science in Optics and Photonics

Imperial College London, London, England

Employment

2009-2010: Systems Engineer

Infosys Technologies, Karnataka, India

2013-2015: Graduate research assistant

Deutsches Elektronen-Synchrotron, Hamburg, Germany

Jena, 05.12.2018

Signature